Towards Understanding Empty Nose Syndrome using Computational Fluid Dynamics

A thesis submitted in partial fulfilment of the requirements for the Degree of Master of Engineering in Mechanical Engineering

By **Tim Flint**

Senior Supervisor: Dr. Mathieu Sellier
Co-Supervisor: Dr. Sid Becker
Student Identification Number: 57910239

Department of Mechanical Engineering
University of Canterbury
New Zealand
August 16, 2017

Abstract

Empty nose syndrome (ENS) presents with sensations of nasal obstruction despite sufficiently patent nasal airways and little is known about its cause. The present work begins with a critical evaluation of the literature. From this we hypothesize that the sensation felt in ENS is likely a distinct sensation caused by abnormal airflow.

High resolution computational fluid dynamics (CFD) simulation, including heat and water transport, of one normal and two ENS nasal cavities before and after corrective surgery were performed. The results are presented with reference to patient symptoms as recorded by the SNOT22 and ENS6Q standard questionnaires. The results supported previous findings of a deficit in inferior wall shear stress in ENS nasal cavities.

It was hypothesised that the state of the nasal mucus layer could provide a universal explanation for the majority of ENS symptoms. More realistic boundary conditions for CFD need to be explored so that this hypothesis can be tested. Constant temperature, variable temperature, and a novel drying model boundary treatments for heat and water transport were compared in Poiseuille flow. It was found that the constant temperature condition produced significantly different results from the other conditions. Also the introduction of a drying model may have implications for the location of maximum heat flux in the nasal geometry.

Acknowledgements

Firstly I would like to thank my Supervisor, Prof. Mathieu Sellier, for supporting and guiding me through this process and putting up with interruptions caused by my travels and topic changes. Prof. Sellier has been very understanding of my decision to pull out of the PhD program to submit this Master's thesis and I greatly appreciate his support.

Many thanks to Dr. Mahdi Esmaily-Moghadam for the time he spent giving me advice, teaching me important skills and concepts, and providing me access to the MUPFES simulation package.

Thanks to all of my office-mates, most notably, Jeff O'Brien, for bouncing ideas and teaching me the basics.

Thank you to Stanford University, in particular, Prof. Parviz Moin and the Center for Turbulence Research for hosting me for a year, offering me guidance, and for the use of the Certainty computer cluster.

Thanks to Stanford's School of Medicine, specifically Dr. Andrew Thamboo, Dr. Nathalia Velasquez, and Prof. Jayakar Nayak for providing the inspiration for this project, clinical data, and a medical perspective.

Thank you to Prof. Sid Becker, for his support and advice.

Thank you to the computer support and administrative teams, both at the University of Canterbury and at the Center for Turbulence Research, for making things run as smoothly as possible.

I would like to acknowledge financial support from the Canterbury Community Trust, Fulbright New Zealand, and the University of Canterbury Alumni Association.

Finally I would like to thank my family and friends for supporting me through this experience.

List of figures

1.1 The nasal anatomy. 2

3.1 The nasal cavity CFD domain and mesh. 21
3.2 Mesh-independence study for the nasal cavity simulation. . . . 28
3.3 Nose simulation scalar profile comparison with literature. . . . 32
3.4 Accumulated SNOT-22 and ENS6Q scores. 35
3.5 Individual symptom scores for SNOT-22. 37
3.6 Individual symptom scores for ENS6Q. 38
3.7 Stream tracers in the nasal cavities. 39
3.8 Nasal cavity surface pressures. 41
3.9 Total heat flux through the mucosal surface in the nasal cavities. 44
3.10 Water flux through the mucosal surface in the nasal cavities. . 46
3.11 Wall shear stress in the nasal cavities. 47
3.12 Slices through the velocity field in the nasal cavities. 49
3.13 Slices through the RMS velocity field in the nasal cavities. . . 52
3.14 Slices through the temperature field in the nasal cavities. . . . 54
3.15 Slices through the water concentration field in the nasal cavities. 55
3.16 Nasal cavity surface areas. 57
3.17 Nasal cavity surface metrics. 57
3.18 Temperature and water concentration at the exit of the nasal cavities. 59
3.19 Total heat loss with axial position in the nasal cavities. 61
3.20 Peak smoothed heat flux in the nasal cavities. 66
3.21 Mean wall shear stress with height in the nasal cavities. 68
3.22 Mean total heat flux with height in the nasal cavities. 70

4.1 Schematic of the channel geometry. 80
4.2 Channel mesh. 81
4.3 Energy balance across the wall-air interface. 86
4.4 Transport equation coupling solution method. 87
4.5 Drying model implementation. 90
4.6 Wall conduction layer constants with layer thickness. 92
4.7 Channel mesh-independence study. 95
4.8 Channel mean temperature profile at two mesh resolutions. . . 96
4.9 Verification of channel simulation methods. 97
4.10 Temperature and water concentration in the channel. 98
4.11 Heat flux components and wall temperature in the channel using the full drying model at 25°C. 99
4.12 Heat flux components and wall temperature in the channel using the full drying model at 26°C. 100
4.13 Relative humidity on the channel wall using the full drying model. 101
4.14 Channel boundary condition comparison for fluxes and wall temperature. 102
4.15 Channel boundary condition comparison for air-conditioning. . 103
4.16 Axial heat flux in the channel wall conduction layer. 104

List of tables

3.1 Properties of air at 25°C 26
3.2 Nose simulation metric comparison with literature. 30

4.1 Channel dimensions. 81
4.2 Channel simulation material properties. 90
4.3 Physiological properties used for the solution to the Pennes equation. 92

Glossary

Alloderm — Donated tissue with all cells removed leaving a tissue matrix.

Anosmia — Loss of the sense of smell.

Anterior — Closer to the front in position.

Atrophic rhinitis — Nasal condition in which atrophy of the nasal mucosa causes the formation of thick dry crusts in the nasal cavity.

Auditory tube — Connects the nasopharynx to the middle ear.

Aural — Relating to the ears or hearing.

Chronic — Persisting for a long time.

Cilia — Slender projections from a cell body.

Coronal plane — Vertical plane through the body with normal in the forwards facing direction.

Dermis — The inner of two layers that make up the skin.

Dyspnoea — Shortness of breath.

Emollient — Preparation for soothing the skin.

Endoscope — Fibre-optic instrument for looking deep into the body.

Eustachian tube — See auditory tube.

Fractional inspiratory time — The fraction of time spend on inspiration during the breathing cycle.

Functional MRI — Imaging procedure in which brain activity is measured by detecting changes in blood flow in the brain.

Hypoxaemia — Low blood oxygen concentration.

Inferior — Lower in position.

in silico — Taking place within computer simulation.

in vivo — Taking place in a living organism.

Lateral — Situated towards the sides.

Meatus — Passageway leading to the interior of the body (see page 2).

Mechanoreceptor — Nervous sensor that responds to mechanical pressure or distortion.

Medial — Situated near the body's midline.

Medical treatment — A treatment regime not involving surgery.

Mucociliary transport — The transport of mucus by ciliary action.

Mucus layer — Thin layer of mucus that lines the nasal cavity.

Nares — Commonly called nostrils, external openings of the nasal cavity.

Nasal mucosa — Mucous membrane lining the interior surfaces of the nasal cavity.

Nasal resistance — The nasal passages' aerodynamic resistance measured in $\frac{Pa\ s}{ml}$.

Nasal valve area — Location of minimum cross-sectional area in the nose, posterior of the vestibule, anterior of the turbinates (see page 2).

Nasopharynx — Space at the rear of the nasal cavity connecting it to the throat (see page 2).

Nasopulmonary bronchomotor reflex — Reflex which regulates breathing through deepening inhalation.

Neuropsychological — Relating to the function of the brain and its role in psychological processes.

Neurosensory — Relating to the sensory function of the nervous system.

Olfactory — Relating to the sense of smell.

Ostium — An opening into a cavity.

Pathophysiology — The mechanisms within an organism (physiology) associated with symptoms of a disease state (pathology).

Perfusion — Typically refers to the delivery of blood to tissue through the circulatory system.

Pharynx — The cavity behind the nose and mouth.

Physiological — Relating to the way in which parts of an organism functions.

Posterior — Further back in position.

Post-nasal drip — The feeling of mucus accumulating or dripping from the back of the nose into the throat.

Primary ciliary dyskinesia — Genetic disorder resulting in defects in the motion of the cilia in the respiratory tract and poor mucus clearance.

Psychological — Relating to a persons mental and emotional state.

Pulmonary — Relating to the lungs.

Resection — The surgical removal of an organ or body part.

Rhinology — The branch of medicine associated with the nose.

Sagittal plane — Vertical plane through the body with normal facing left or right.

Segmentation — The process by which digital image data is split into multiple parts.

Septal — Relating to the septum.

Septoplasty — Surgical modification of the septum.

Septum — Structure that separates the left and right nasal airways (see page 2).

Sinus — Cavity in a bone or tissue (see page 2).

Sinusitis — Inflammation of the tissue lining the sinuses.

Somatic symtom disorder — Mental disorder resulting in the presentation of physical symptoms that cannot be explained by medical examination.

Superior — Higher in position.

Thermoreceptor — Nervous sensor that responds to changes in temperature.

Trachea — Commonly called the wind pipe, connects the upper airway to the lungs.

Transverse plane — Horizontal plane through the body.

Trigeminal nerve — The nerve that is responsible for sensation in the face.

Turbinate — Long, curled bony structure protruding into the nasal cavity (see page 2).

Vestibule — Skin lined region of the nasal cavity near the entrance to the nose (see page 2).

Vibrissae — Stiff hairs in the vestibule.

Abbreviations

AR — atrophic rhinitis

CFD — computational fluid dynamics

CI — confidence interval

CT — computerized tomography

ENS — empty nose syndrome

ENS6Q — empty nose syndrome 6-item questionnaire

ITR — inferior turbinate resection

MRI — magnetic resonance imaging

MUPFES — multi-physics finite element solver

RH — relative humidity

RMS — root mean square

SD — standard deviation

SIS — small intestinal submucosa, typically porcine (pig)

SNOT-22 — sino-nasal outcome test 22

STL — steriolithography

TRPM8 — transient receptor potential cation channel subfamily M member 8

List of symbols

A - first conduction layer constant [m^2K/W]

α_T - thermal diffusivity [m^2/s]

α_w - molecular diffusivity of water in air [m^2/s]

B - second conduction layer constant [$°C$]

β - $= \sqrt{\frac{\omega_b \rho_b c_b}{k}}$ [1/m]

C - water vapour concentration [kg/m^3]

C_M - molar concentration [mol/m^3]

c - speed of sound in air [m/s]

c_b - specific heat capacity of blood [$J/kg\,K$]

c_t - specific heat capacity of tissue [$J/kg\,K$]

D_h - hydraulic diameter [m]

E_w - saturation vapour pressure of water [hPa]

f - frequency [Hz]

g - acceleration due to gravity [9.81 m/s^2]

$\Delta\mathcal{H}$ - latent heat of evaporation for water [J/kg]

h - channel half height [m]

h_c - convective heat transfer coefficient [W/m^2 K]

k - thermal conductivity [W/m K]

L - length [m]

l - length scale [m]

M - Mach number

M - molar mass [g/mol]

μ - dynamic viscosity [kg/m s]

Nu - Nusselt number

n - number of data points

n - number of moles [mol]

ν - kinematic viscosity [m^2/s]

Pe - Péclet number

Pr - Prandtl number

$\dot{q}$ - heat flux [W/m^2]

$\dot{q}_{water}$ - water flux [kg/m^2 s]

ρ - density [kg/m^3]

R - universal gas constant [8.314 J/mol K]

Re - Reynolds number

Ri - Richardson number

S - heat source term [W/m^3]

Sc - Schmidt number

St - Strouhal number

T - temperature [K]

t - time [s]

θ - generic transported quantity

τ_w - shear stress at the wall [Pa]

U - velocity scale [m/s]

u_τ - friction velocity [m/s]

u_x - x-component of velocity [m/s]

V - volume [m^3]

Wo - Womersley number

w - layer thickness [m]

ω_b - blood perfusion rate [$m^3_{blood}/m^3_{tissue}\,s$]

Δx - mesh size in the x-direction [m]

y - distance to the wall or the vertical ordinate [m]

y^+ - dimensionless distance to the wall

Contents

Abstract i

Acknowledgements ii

List of figures iii

List of tables v

Glossary vi

Abbreviations x

List of symbols xi

1 Introduction 1

1.1 Empty nose syndrome 1

1.2 Motivations and objectives 3

1.3 Thesis overview 4

2 Literature review 5

2.1 Symptoms 5

2.2 Diagnosis 6

2.3 Treatment 6

2.3.1 Medical treatment 6

2.3.2 Surgical treatment 7

2.4 Pathophysiology 7

2.4.1 Psychological factors 10

2.4.2 The baseline of normal nasal airflow 10
2.4.3 Neurosensory damage 11
2.4.4 The role of nasal airflow 12
2.5 Previous work 14
2.6 CFD to inform nasal surgery 16
2.7 Discussion and conclusions 17

3 Nasal cavity simulation **20**
3.1 Objectives 20
3.2 Methodology 20
3.2.1 Anatomical model 20
3.2.2 Mesh 22
3.2.3 Flow solver 23
3.2.4 Assumptions 23
3.2.5 Boundary conditions 25
3.2.6 Mesh-independence analysis 27
3.2.7 Validation 29
3.3 Results 32
3.3.1 Patient information 32
3.3.2 Quantification of symptoms 34
3.3.3 Nasal cavity visualization 38
3.3.4 Flow field visualisation 48
3.3.5 Global comparison 56
3.3.6 Surface heat loss distribution 60
3.4 Discussion 62
3.4.1 The paradox 62
3.4.2 Patient specific outcomes 62
3.4.3 The air conditioning capacity of the ENS nose 64
3.4.4 Response to common hypotheses 64
3.4.5 New hypotheses 67
3.4.6 Final thoughts 71
3.4.7 Limitations 73
3.5 Conclusions 75

4 Exploration of new boundary conditions **77**
4.1 Background . . . 77
4.2 Objectives . . . 79
4.3 Methodology . . . 80
4.3.1 Geometry and mesh . . . 80
4.3.2 Numerical methods . . . 82
4.3.3 Boundary conditions and material properties . . . 89
4.3.4 Mesh-independence analysis . . . 94
4.3.5 Verification . . . 96
4.4 Results . . . 97
4.4.1 Full drying model . . . 97
4.4.2 Boundary condition comparison . . . 101
4.4.3 Effect of streamwise wall conduction . . . 103
4.5 Discussion . . . 105
4.5.1 Implications for nasal CFD . . . 105
4.5.2 Limitations . . . 106
4.6 Conclusions . . . 107

5 Conclusions **109**
5.1 List of contributions . . . 111

6 Future work **113**
6.1 Testing proposed hypotheses . . . 113
6.2 Clinical research . . . 114
6.3 Development of computational fluid dynamics for empty nose syndrome . . . 115
6.4 Translation of computational results for clinical use . . . 116

Bibliography **117**

A Analytic solutions in the wall conduction layer **125**
A.1 Solution to the Pennes equation . . . 125
A.2 Solution to the heat conduction equation . . . 128

Chapter 1

Introduction

1.1 Empty nose syndrome

As originally used in 1944 by Kern and Stenkvist (Scheithauer (2010)), the term 'empty nose syndrome' described patients with a literal empty nose. The lack of turbinate tissue and the resulting cavernous nasal cavities seen on computerized tomography (CT) scans of such patients prompted the description of an empty nose. Empty nose syndrome was first used in the literature by Moore and Kern (Moore & Kern (2001)) in their review of 242 cases of atrophic rhinitis (AR). Moore and Kern identified several patients who complained of a sense of nasal obstruction despite objectively presenting with widely patent nasal cavities. They subsequently defined empty nose syndrome (ENS) as 'the symptoms of atrophic rhinitis coupled with a cavernous nasal airway lacking identifiable turbinate tissue'. The incidence of ENS is unknown, and estimates seem to vary greatly with some as high as 20% following inferior turbinate surgery (Chhabra & Houser (2009)). A schematic of nasal anatomy, including the turbinates, is shown in Figure 1.1 for the reader's convenience

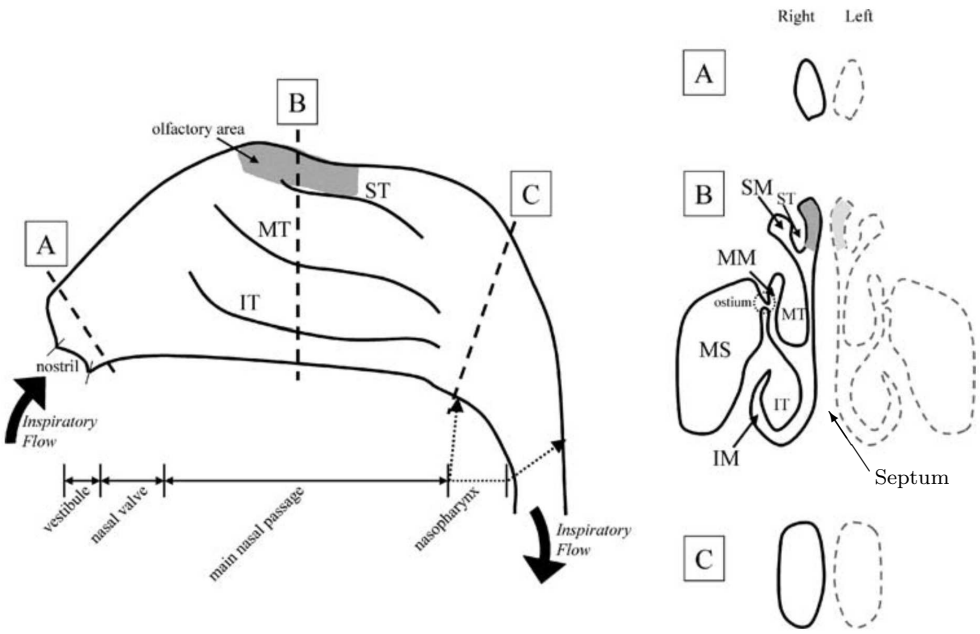

Figure 1.1: Nasal anatomy adapted from Croce *et al.* (2006). A, B, and C represent cross-sections through the nose. IT, MT, and ST refer to inferior turbinate, middle turbinate, and superior turbinate. IM, MM, and SM refer to inferior meatus, middle meatus, and superior meatus. MS refers to the maxillary sinus. In a patient with ENS, one or several of the turbinates are absent.

1.2 Motivations and objectives

Patients with empty nose syndrome (ENS) suffer from a sense of nasal obstruction despite their airways often being overly patent. Little is known about the physical and biological mechanisms responsible for this. Overly patent airways typical in ENS patients are normally caused by excessive removal of turbinate tissue for the treatment of conditions such as nasal obstruction (Chhabra & Houser (2009)). Currently, no objective tests that are normally used for characterizing the health of patients' upper airways can quantify or diagnose ENS. Doctors are forced to base their judgements on purely subjective metrics (Houser (2007)). This deficiency makes identification and treatment difficult, prompting some doctors, in the past, to choose not to acknowledge ENS as a real clinical condition (Payne (2009)). Payne noted that perhaps one reason for this lack of acceptance was that we could not explain ENS with the current knowledge of the human nose. More recent work suggests that changes in airflow, mucosal cooling, or neurosensory receptors could cause the symptoms present in ENS (Kuan *et al.* (2015)); however, a direct link has not yet been made. Initially, ENS is treated medically via multiple vectors with the goal of moisturising the nasal mucosa. In severe cases, however, surgical treatment may be the only option. Surgical treatment typically involves implanting some material under the nasal mucosa to replace the missing turbinate tissue and restore normal nasal function through manipulation of nasal fluid dynamics.

This work focuses on the use of computational fluid dynamics (CFD) to study ENS. Simulation of airflow in ENS and surgically corrected nasal geometries has been performed, and boundary conditions for CFD relevant to ENS have been explored. Computational fluid dynamics allows detailed access to surface metrics such as heat flux and wall shear stress which may elucidate a link to the observed symptomatic improvement following corrective surgery. The few studies that have used CFD to simulate airflow in ENS patients have revealed reduced air conditioning capacity and changes in the distribution of airflow in the nose (Garcia *et al.* (2007); Scheithauer (2010); Li *et al.* (2017)). These conclusions are informative but do not relate the

airflow directly to its interaction with the nasal mucosa and the sensation felt by the patient. An in-depth analysis of surface metrics such as heat flux and wall shear stress is required to understand how airflow contributes to the subjective symptom profile of ENS.

1.3 Thesis overview

- Chapter 2 Provides a detailed literature review of ENS research to date. It provides context to the research presented here, cements the motivation, and facilitates exploration of the pathophysiology of ENS. An attempt has been made to critically address claims made by other researchers using evidence from the literature.
- Chapter 3 presents CFD simulations of patient specific diseased and normal nasal airways. It includes a description of the CFD methodology (Section 3.2) and discussion of the results obtained with their meaning in the context of the wider literature (Section 3.3).
- Chapter 4 presents a brief investigation of a more realistic mucosal boundary condition to determine how it would affect simulations of the human nasal cavity and to provide a first step towards accurate modelling of the air-mucosa interaction.
- Chapter 5 compiles all the major conclusions presented in the thesis and outlines the original contributions made by this work.
- Chapter 6 makes some suggestions for future work.

Chapter 2

Literature review

2.1 Symptoms

The characteristic symptom of empty nose syndrome is a paradoxical sense of nasal obstruction despite objectively patent nasal airways. Patients' sensation of nasal obstruction is often difficult to describe and may manifest in descriptions of stuffiness, an inability to breathe well, a nose that feels too open while being unable to fill the lungs, or a sensation of suffocation (Houser (2007)). These sensations can result in obsession with ones breathing and give rise to secondary symptoms such as an poor sleep, inability to concentrate, chronic fatigue, frustration, irritability, anger, anxiety, and even depression; thus, ENS can significantly affect patients' quality of life (Kuan *et al.* (2015)). Other symptoms that may be present include dyspnoea, mucosal dryness, decreased ability to smell, crusting, pain, or headache (Houser (2007); Chhabra & Houser (2009); Shah *et al.* (2016); Saafan *et al.* (2016); Coste *et al.* (2012)). All ENS patients have had turbinate procedures in the past and symptoms can manifest soon after turbinate surgery (Houser (2007)) or can take months to years to appear (Chhabra & Houser (2009)).

2.2 Diagnosis

Diagnosis of ENS is difficult due to the lack of any objective tests that can corroborate the patient's subjective sensations. The diagnosis of ENS is therefore a diagnosis of exclusion (Sozansky & Houser (2015)) and is hallmarked by lack of turbinate tissue and complaints of nasal obstruction. The difficult identification of ENS, based largely on subjective metrics, prompted some to choose not to acknowledge ENS as a real clinical condition (Payne (2009)). Payne notes that perhaps one reason for this lack of acceptance is that we cannot explain ENS with our current knowledge of the human nose. Careful investigation of published results on inferior turbinate resection (ITR) does, in fact, reveal postoperative anomalies such as continued complaints of unexplained breathing difficulty that are indicative of ENS (Chhabra & Houser (2009)).

2.3 Treatment

ENS is initially treated medically, with surgery reserved for only the most severe cases.

2.3.1 Medical treatment

Medical treatment is similar to that of atrophic rhinitis (AR) (Leong (2015)) and is centred around mucosal hygiene and moisturising. Medical treatment for ENS patients is not as effective as for those with AR (Jang *et al.* (2011)). Treatment typically includes (Houser (2007); Coste *et al.* (2012)):

- Use of a humidifier
- Nasal sprays such as isotonic sodium chloride
- Nasal lavage
- Emollients
- Local corticosteroids

2.3.2 Surgical treatment

Surgical treatment involves implanting material beneath the mucosa in the nasal cavity as a substitute for missing turbinate tissue. Corrective surgical technique has been motivated by the idea of re-establishing nasal resistance, increasing surface area available for air conditioning, and restoring nasal aerodynamics to a nominal state (Jang *et al.* (2011)). Surgical treatment of ENS tends to result in an improvement of symptoms, though up to 21% may report only marginal benefits (Leong (2015)). Surgical treatment can effectively relieve abnormal breathing sensation and mucosal crusting (Moore & Kern (2001)), however patients who's main complaint is pain do not seem to benefit as much (Houser (2007)). Implants are typically placed on the septum, floor, or lateral wall of the nasal cavity (Chhabra & Houser (2009); Jang *et al.* (2011); Rice (2000)). Houser (Houser (2007)) proposed the cotton test to help inform the placement and size of an implant. The cotton test involves placing a lump of cotton wool that has been moistened with saline solution into the nose where an implant would be feasible; the cotton acts as a temporary implant. The patient is asked to breathe normally for 30 minutes with the cotton in place and report any changes in their symptoms. Only those who notice a significant improvement in their breathing are offered surgery. It was later suggested that the cotton test be used to aid diagnosis of ENS (Chhabra & Houser (2009)).

2.4 Pathophysiology

The pathophysiology of ENS is unclear though there has been much speculation.

- Moore and Kern (Moore & Kern (2001)) suggested:
  - Patients lack a baseline of normal airflow to compare too.
  - Nerve damage in the nasal mucosa.
  - Lack of nasal resistance.

- Chhabra and Houser (Chhabra & Houser (2009)) suggested a few factors:
  - Sensory nerves regenerate poorly following turbinate surgery resulting in reduced sensation of airflow.
  - Airflow in the nose is disrupted resulting in lower airflow sensation.
  - A lack of nasal resistance leads to poor pulmonary function.
  - Poor humidification of incoming air dries the mucosa leading to crusts which impair the sensation of airflow.
- Scheithauer (Scheithauer (2010)) discussed:
  - Dehydration of the mucosa due to high speed air impacting the walls of the nasal cavity and insufficient air humidification results in a lack of area of functional mucosa.
  - Reduced air-mucosa contact decreases the sensation of airflow.
  - Reduced nasal resistance causes malfunction of the nasopulmonary bronchomotor reflex causing poor pulmonary function.
- Kuan *et al.* (Kuan *et al.* (2015)) suggested three factors are responsible:
  - Changes to the local environment caused by structural changes.
  - Disruption to mucosal cooling.
  - Damage to neurosensory mechanisms.
- Sozansky and Houser(Sozansky & Houser (2015)) discussed possible mechanisms at length and mentioned many possible causes including:
  - Receptors in the nasal mucosa are not stimulated enough due to lack of mucosal cooling. This results in decreased sensation of airflow. The lack of mucosal cooling is caused by a reduction in mucosal surface area and modified airflow.

  - Airflow is not sensed properly by the nasal mucosa but still activates stretch receptors in the lungs producing contradictory signals. This gives rise to the distress associated with breathing seen in ENS patients.
  - Modified airflow dynamics result in poor air conditioning of inspired air. The warmer, dryer air in the nasal cavity results in mucosal dryness and crusting, decreasing mucosal cooling and hence reducing airflow sensation.
  - Nerve damage after turbinate surgery may result in increased neurosensory detection thresholds which would lead to a diminished sense of nasal airflow.

- Saafan *et al.* (Saafan *et al.* (2016)) cited:
  - Lack of activation of cool thermoreceptors in the nose.
  - Damage to neurosensory mechanisms in the nose.
  - Destruction of the meatal structure resulting in less sensate airflow.

Though there has been much discussion, many settle with broad statements of little certainty. Explanations of the cause of paradoxical nasal obstruction can typically be reduced to some combination of the following:

- **Nerve damage** resulting in loss of airflow sensation.
- **Less sensate airflow** decreasing airflow sensation.
- **Lack of nasal resistance** producing poor pulmonary function and abnormal breathing sensation.

The following provides a discussion of the evidence behind possible explanations for ENS and justifies the need to perform CFD simulations of ENS nasal cavities.

2.4.1 Psychological factors

Without a useful objective metric, the patient's subjective sense of nasal obstruction is often passed off as being purely psychological in nature (Sozansky & Houser (2015)). Payne (Payne (2009)) notes that the high number of psychiatric findings in ENS patients may be cause for concern, and that pre-existing neuropsychological issues may be exacerbated by turbinate surgery. Coste *et al.* (Coste *et al.* (2012)) also suggest the possibility that psychiatric disorder could play a role in ENS. Though a psychological role is an easy explanation for the paradoxical symptoms, there is no hard evidence in support of this hypothesis. On the other hand, paradoxical nasal obstruction typically presents with other, observable, symptoms (Houser (2007)) which also reduce following treatment. This would imply that there may be some underlying physiological problem causing the sensation of nasal obstruction. Additionally it has been shown, through functional magnetic resonance imaging (MRI), that the brain activity of patients with ENS are consistent with that of someone under real respiratory distress (Freund *et al.* (2011)). More recently, one patient was treated as though ENS was a somatic symptom disorder (a psychological disorder) (Lemogne *et al.* (2015)). The patient showed significant functional improvement in social and leisure activities, though did not report much improvement in ENS symptoms. Finally Thamboo *et al.* (Thamboo *et al.* (2017)) tested ENS patients for placebo effect while administering the cotton test and found no patients test positive.

While psychological factors could exacerbate symptoms in some patients, the evidence presented here would suggest that the cause of ENS is not psychological and has some physical grounds.

2.4.2 The baseline of normal nasal airflow

All patients who suffer from ENS have had some kind of turbinate procedure, often surgical reduction of the turbinates to treat an obstructed nasal cavity (Houser (2007)). Some have suggested that because these patients have never previously experienced normal nasal airflow, their incorrect interpreta-

tion of what should feel normal explains their paradoxical sensation of nasal obstruction (Ophir (1990)). However, the fact that patients report improvement in their symptoms following surgical implants implies the existence of a state that feels normal. If this is the case then the lack of a normal baseline to compare to becomes irrelevant.

2.4.3 Neurosensory damage

Neurosensory damage following turbinate surgery is often speculated as being responsible for a lack of sensation of airflow and the paradoxical sensation of nasal obstruction in ENS. There is no explicit evidence of neurosensory damage in ENS patients, however there is evidence that even uncomplicated surgery (Aasvang & Kehlet (2010)), or surgery that carefully preserves nerves (Witt (2005)) can result in post operative nerve dysfunction. Nerve dysfunction can present as numbness (Aasvang & Kehlet (2010)) or pain (Kehlet *et al.* (2006)). Numbness could result in increased detection thresholds for cold, warmth, and mechanical stimulation. Sozansky (Sozansky & Houser (2015)) suggested that if the nasal mucosa was affected in this way, patients would experience a decreased sensation of nasal airflow. They also suggest that the reason only some patients develop ENS could be due to differences in nerve recovery. Finally, the existence of ENS-type patients (Houser (2007)), whose turbinates look normal in size yet they present with symptoms of ENS, could be explained by neurosensory damage of the mucosa following turbinate surgery.

After some contradiction in the literature, it was shown by Clarke *et al.* (Clarke *et al.* (1992)) that mucosal neurosensory receptors are unimportant to the sensation of nasal airflow. After anaesthetic of the nasal mucosa, patients reported no significant change in their sensation of airflow throughout their nose. This would suggest that numbness resulting from neurosensory damage following turbinate surgery could not cause a sensation of nasal obstruction in ENS patients. Also, corrective surgery for ENS patients improves symptoms despite surgically damaging the nasal mucosa further. However, for ENS patients that report pain as a predominant symptom, neurosensory damage

might be a factor; Houser (Houser (2007)) noted that these patients do not benefit much from corrective surgery.

Neurosensory damage may contribute to ENS in some patients but is unlikely to be responsible for the paradoxical sensation of nasal obstruction that is often observed.

2.4.4 The role of nasal airflow

Airflow patterns in the nasal cavity are essential to the nose's physiological function of humidification and conditioning inspired air. Geometrical changes to the nasal cavity following turbinate surgery may have a detrimental effect on nasal airflow and nasal function. Many have speculated that airflow patterns play a role in ENS, though the complexity of fluid dynamic analysis makes its role difficult to test and understand. Airflow patterns can be modified almost instantaneously through variation in the nasal geometry. The fact that the cotton test (a purely geometrical variation to the nasal cavity) results in near-instant improvement in ENS patient symptoms (Houser (2007); Velasquez *et al.* (2016)) lends support to the idea that nasal airflow may play a role in the pathophysiology of ENS. The only evidence conflicting with this idea is the fact that it sometimes takes a while, months to years, for ENS symptoms to occur following turbinate surgery (Chhabra & Houser (2009)). This delay in symptom development could, perhaps, be caused by geometrical changes to the nasal cavity as swelling reduces and the nose heals during the post-surgical recovery period, or a slowly deteriorating condition resulting from an extended period of abnormal airflow.

With the absence of solid supporting evidence for the influence that other factors such as psychological and neurosensory factors play in the pathophysiology of ENS, it is probable that nasal airflow is important. Performing CFD to help understand ENS is likely to be of benefit to our understanding of this condition.

Nasal resistance: The removal of turbinate tissue typically results in a reduction of nasal resistance, and hence ENS patients often present with reduced nasal resistance (Houser (2007)). Moore and Kern (Moore & Kern (2001)) postulated that sufficient nasal resistance was important for a satisfying breathing sensation and a lack of resistance may be perceived as a sense of congestion. It has also been shown that nasal resistance helps maintain pulmonary volume and may indirectly determine arterial oxygenation (Swift *et al.* (1988)). Subsequently, reduced nasal resistance may lead to hypoxaemia, resulting in a sense of breathlessness and respiratory distress.

Some evidence shows that nasal resistance correlates with objective nasal patency following surgery for nasal obstruction (Broms *et al.* (1982)). However, there is also evidence that nasal resistance and airflow sensation are not linked at all. It has been shown that inhalation of menthol has no effect on nasal resistance but results in an increased sensation of airflow, conversely, nasal resistance decreases following exercise but this is not accompanied by any change in airflow sensation (Burrow *et al.* (1983)). Others have clearly shown a lack of correlation between nasal resistance and patient reported nasal patency in large samples of people (Hardcastle *et al.* (1988); Jones *et al.* (1989*b*)). Finally, Jones *et al.* (Jones *et al.* (1988)) showed that in patients undergoing inferior turbinate reduction procedures for nasal obstruction, similar reductions in nasal resistance does not correlate to similar patient outcomes. Anterior trimming of the turbinates and complete resection of the turbinates produced the same decrease in nasal resistance but only the complete resection resulted in a statistically significant increased sensation of nasal patency.

Lack of nasal resistance may be related to dyspnoea that is often seen in ENS patients, though it is unlikely to be responsible for sensations associated with paradoxical nasal obstruction.

Airflow sensation: It has often been implied that paradoxical nasal obstruction may be the result of reduced airflow sensation caused by a disruption to the normal sensory stimulus during breathing. The sensation of

airflow and nasal patency is thought to be determined through nasal cooling as air flows through the nose (Zhao *et al.* (2011)). This sensation may be felt through activation of TRPM8 thermoreceptors (Baraniuk (2011)). It has been shown that ENS patients respond with partial relief from nasal congestion upon inhalation of menthol (which directly activates the TRPM8 thermoreceptors) (Freund *et al.* (2011)) proving that thermoreceptors are still present and functioning in these patients.

Thermoreceptors are concentrated in the nasal vestibule (Jones *et al.* (1989*a*)) and it has been shown that anaesthesia of the vestibule causes a sensation of nasal obstruction (Jones *et al.* (1987)). Conversely, after conflicting results in the literature, the nasal mucosa is not thought to play any significant role in the sensation of airflow (Clarke *et al.* (1992)). The turbinate surgery that results in ENS modifies only the nasal cavum leaving the nasal vestibule untouched. The natural conclusion from this would be that turbinate surgery should not have any affect on a patient's sensation of airflow. Regardless, there have been no reports in the literature of people reporting significant ENS-like symptoms following anaesthesia of the nasal vestibule, or nasal mucosa.

2.5 Previous work

Numerous studies have attempted to visualize the airflow within overly patent airways in order to understand how they differ from a nominal case. Grützenmacher and others (Grützenmacher *et al.* (2003)) performed experiments on acrylic casts of a healthy nasal cavity and compared results to that of the same geometry after removal of the inferior turbinate. They found that airflow through the normal nose was quite evenly distributed throughout the entire nasal cavity; however, removal of the inferior turbinate resulted in the majority of air flowing through the lower half of the cavity where the turbinate used to be. Additionally, flow through this region was disorganized, displaying what was described as a strong increase in turbulence. Others corroborated these results with CFD simulations of virtual turbinate removal of

healthy nasal geometries derived from CT scans (Di *et al.* (2013), Na *et al.* (2012)) showing also that the majority of the air flowed through the inferior half of the cavity. It is interesting to note discrepancy between these results and that of CT models of patients actually suffering from ENS, which found instead that the majority of the airflow travels through the superior half of the nasal cavity (Garcia *et al.* (2007), Scheithauer (2010), Li *et al.* (2017)). This indicates that there may be flow features that are unique to ENS and can aid the prediction of this condition through CFD simulation.

Studies involving virtual surgery have also investigated how metrics such as nasal resistance and wall shear stress change following inferior turbinate resection, showing wide variation in results. The work of Wexler and others (Wexler *et al.* (2005)) showed a decrease in nasal resistance following removal of the inferior turbinate, Di and others (Di *et al.* (2013)) along with Chen and colleagues (Chen *et al.* (2010)) found a decrease in nasal resistance as well as wall shear stress. In contrast, Na and others (Na *et al.* (2012)) observed increases in both nasal resistance and wall shear stress. These studies demonstrate that airflow patterns following inferior turbinate resection can vary greatly between individuals. All studies of overly patent airways including that of real ENS patients do, however, agree that the airflow in the space formerly occupied by the inferior turbinate is largely disorganized displaying vortical-type structures.

It is apparent that experience alone cannot guarantee a successful surgical plan, with Houser stating that on occasion he has been surprised by the location of a wad of cotton that gives symptomatic improvement (Houser (2007)). It is obvious that more focused CFD analyses are needed if we are to fully understand this condition. Of most relevance to the present study is the work by Garcia and others (Garcia *et al.* (2007)) which appears to be the only example of CFD analysis on a patient suffering from ENS before and after surgery to correct the condition. The patient tested also expressed symptoms of atrophic rhinitis which commonly accompany ENS, and while Garcia and colleagues hypothesized that most symptoms, including crusting and anosmia, could be explained by abnormal water flux distribution causing

damage to the mucosa, they were unable to fully explain the cause of the paradoxical nasal obstruction. Their surgery did not relieve the patient of nasal obstruction, but they did speculate that the loss of temperature and pain receptors resulting from the damage to the mucosa may be responsible. More recently Li *et al.* (Li *et al.* (2017)) simulated patients pre- and post-inferior turbinate resection that resulted in ENS. They revealed that the removal of the turbinate resulted in a narrow jet of air directed towards the middle meatus, and decreased airflow and wall shear stress around the inferior turbinate in the ENS nose.

Konstantinidis *et al.* (Konstantinidis *et al.* (2017)) performed intranasal trigeminal testing in patients with ENS and compared them to normal subjects and ITR patients who did not develop ENS. This tested subjects' sensitivity to menthol and olfactory stimulus inhaled through the nose. It was found that patients with ENS showed significantly lower menthol sensitivity than both normal and ITR subjects. These results were corroborated by Li *et al.* (Li *et al.* (2017)) and would suggest that their sensitivity to heat flux may be impaired. Whether this is due to nerve damage or unique airflow patterns is unknown, nor is the relevance of this result to the pathophysiology of ENS.

2.6 CFD to inform nasal surgery

The potential benefits of using CFD to inform nasal surgery has been identified by Rhee and co-workers (Rhee *et al.* (2011)), noting that the subjective nature of assessment for nasal reconstruction surgery to treat nasal obstruction leads to a reported 25-50% failure rate. The objective of Rhee's work was to evaluate the ability of CFD to predict surgical outcomes to prove the utility of CFD modelling as part of a surgical planning procedure. It was found that virtual surgical procedures and CFD analysis for a patient undergoing inferior turbinate resection and septoplasty provided good predictions of overall reduction in nasal resistance and flow distribution between the two sides of the nose. Kimbell and colleagues (Kimbell *et al.* (2013)) furthered

Rhee's work by simulating pre- and post-operative nasal geometries of ten patients who underwent various surgery to relieve nasal obstruction. They recorded moderate linear correlation with patient-reported outcomes for unilateral heat flux, unilateral airflow, and unilateral nasal resistance as a fraction of bilateral nasal resistance all calculated on the most obstructed side. These results suggest that the proposed metrics may be useful when planning surgical procedures of this kind. Finally, work by Hariri and colleagues (Hariri *et al.* (2015)) employed CFD to predict if patients would benefit from turbinate reduction surgery and what surgical procedure would give the best results. They assessed nasal resistance, heat flux, and humidity transport and found that predicted outcomes from various procedures was specific to each patient's nasal geometry, emphasizing the need for customized surgical planning. It was also found that the location of inferior turbinate resection, medial vs bottom resection, had little influence on nasal resistance, although nasal air conditioning was better preserved by bottom resection, emphasizing the importance of using multiple metrics to gauge surgical outcome.

To guide surgical intervention for ENS, one must identify objective measures that can be made using CFD or otherwise which correlate with the patients' symptoms. In the case of the subjective sense of nasal obstruction, this has so far proven to be a difficult task.

2.7 Discussion and conclusions

The pathophysiology of ENS is still not well understood despite many attempts to review the literature. A psychological fault is easy to blame given the paradoxical presentation of both an open airway and a sense of nasal obstruction, though there is little to no evidence in support of this explanation. The literature would suggest that it is unlikely that the symptoms could be caused by psychological factors alone.

It is natural to draw a connection between airflow sensation and neurosensory mechanisms. Many have subsequently connected a lack of normal

sensation to a lack of neurosensory function. This conclusion, however, appears not to be supported by evidence. There is no direct evidence that ENS patients suffer from nerve damage, though this may be to due to lack of appropriate tools to measure such an effect. Conversely, there is strong evidence that suggests that a lack of neurosensory function would not result in a sensation of nasal obstruction at all.

By elimination and due to the complex nature of fluid flow, it can be concluded that a disruption of airflow through the nose is likely responsible paradoxical nasal obstruction in ENS, justifying further fluid dynamic analysis.

Nasal resistance is unlikely to be important, evidence against this hypothesis currently outweighs any support. We understand the physiological mechanisms behind a sensation of nasal patency, however a lack of this sensation may not necessarily result in a feeling of nasal obstruction as might be a natural conclusion. There is evidence to suggest that: the thermoreceptors responsible for this sensation are present and functioning in the ENS nose; and the nasal mucosa does not participate meaningfully in this sensation. Instead, it is much more likely that paradoxical nasal obstruction is caused by a distinct sensation that is not felt in the normal subject. Houser (Houser (2007)) noted that ENS patients often have no clear way to describe how they feel, being consistent with the idea of novel sensation being responsible. This idea has not yet been explored in the literature to the authors knowledge. This hypothesis could easily be tested by anaesthetising the mucosa of ENS patients and seeing how they respond.

Shotgun speculation about the pathophysiology of ENS are common in the literature. We now have a large enough literature base to reliably discard some common misconceptions and start asking more targeted questions about the origin of ENS. Computational simulation has the potential to help improve our, currently poor, understanding of ENS. There still remains a paucity of computational investigation into ENS and it is clear that further investigation of patients suffering from the condition would benefit the med-

ical community. It appears that fluid dynamics may be important to the development of ENS, though its role is still unknown. This work will address the role of fluid dynamics in ENS by providing CFD analysis of multiple patients suffering from ENS. The intention is to focus on understanding paradoxical nasal obstruction specifically, by investigating correlation between fluid dynamic metrics obtained using CFD and subjective reports of nasal obstruction. Airflow patterns have not yet been investigated in patients that have suffered from ENS and have seen improvement in nasal obstruction following re-constructive surgery. Using CFD to aid nasal surgical procedures has been gaining traction in the literature and has the potential to shift the current paradigm toward a predictive treatment. It is hoped that the results from this work can be used to inform better surgical procedures with regard to turbinate resection and treatment of ENS.

Chapter 3

Nasal cavity simulation

3.1 Objectives

In this part of the thesis, simulation of patient specific nasal cavities with and without empty nose syndrome are presented. Here we hope to use high resolution simulation to advance our understanding of the fluid mechanics associated with empty nose syndrome. One normal subject and two ENS patients before and after corrective surgery have been simulated and will be presented.

3.2 Methodology

3.2.1 Anatomical model

Patient data were available for one normal subject and two patients diagnosed with ENS. Both patients underwent corrective surgery after which they reported significant improvement in symptoms. Coronal CT scan image data was used to create three-dimensional representations of each patient's nasal cavity before and after surgery. An example of the resulting nasal surface geometry for the pre-surgery case of patient 1 is shown in Figure 3.1(a).

The computer program, 3D Slicer (Fedorov *et al.* (2012)), was used to perform three-dimensional segmentation of the image data and produce a

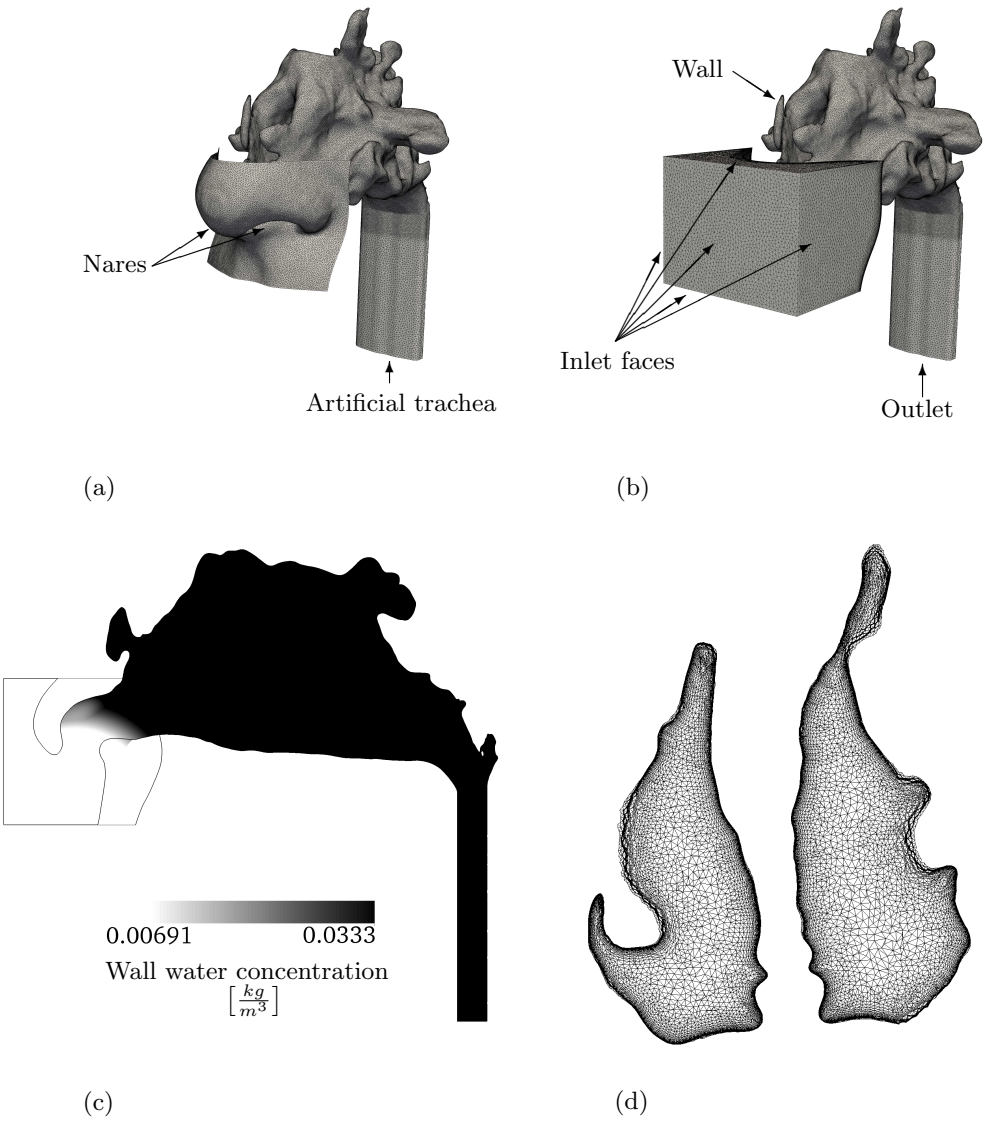

Figure 3.1: The CFD domain and mesh: (a) surface geometry, (b) volume mesh with boundaries labelled, (c) water concentration boundary condition for the mucosal surface, (d) coronal slice through the mesh.

high-quality surface triangulation of the nasal cavity and a portion of the patient's face. Segmentation involves identifying an intensity threshold at which to clip the three dimensional image data to denote the interface between tissue (high intensity) and air (low intensity). An intensity threshold for the image segmentation process was selected for each geometry that best represented the anatomical features of the nose. To remain consistent between cases a systematic procedure was developed by which the user selected a threshold mid-way between minimal and maximal plausible thresholds. Though the selection of this threshold is partly subjective, well-chosen threshold values are not expected to introduce significant error to the fluid dynamic simulations (Quadrio *et al.* (2016)).

The surface triangulation was then smoothed and modified in Meshmixer (Schmidt & Singh (2010)). Any artefacts resulting from the digitization process or CT resolution were smoothed out. Effort was made to ensure that the smoothing removed artefacts while preserving the geometrical form of the nasal cavity. An equal amount of smoothing was applied to all geometries for consistency. An artificial trachea was extended inferiorly from the nasopharynx so that the outflow boundary condition did not significantly affect the fluid dynamics in the nasal cavity. A small region of the patient's face was kept to provide a realistic inflow into the nasal cavity (Figure 3.1(a)).

3.2.2 Mesh

A cross-section of the volume mesh is shown in Figure 3.1(d). A triangular surface mesh with tetrahedral volume elements was generated using the meshing software Pointwise (Pointwise Inc. (2016)). Anisotropic layers were generated on the walls of the nasal cavity in order to resolve the near-wall flow. Multiple mesh resolutions were tested, and the final mesh included approximately 14 million elements. The surface mesh was adapted to the curvature of the surface through a constraint on the maximum deviation from the geometry; the resulting surface mesh was made up of triangles with a maximum edge length of 0.5 mm and a mean of about 0.4 mm. The volume mesh smoothly increased in size from the walls to a specified maximum

edge length of 1 mm. There were 15 anisotropic layers near the wall with a growth rate of 1.25 and an approximate maximum y^+ calculated locally of about 0.8. y^+ was defined as

$$y^+ = \frac{y\ u_\tau}{\nu}, \tag{3.1}$$

where

$$u_\tau = \sqrt{\frac{\tau_w}{\rho}}, \tag{3.2}$$

and y is the distance to the wall, u_τ is the friction velocity, ν is the kinematic viscosity, τ_w is the wall shear stress, and ρ is the density.

3.2.3 Flow solver

A validated (Arbia *et al.* (2014); Steinman & Others (2013)) finite element solver, MUPFES (Esmaily-Moghadam (2014)), was used to solve the incompressible Navier-Stokes equations for the fluid motion and scalar advection-diffusion equations for temperature and water transport in the nasal geometry. Turbulence was treated with the variational multi-scale method (Bazilevs *et al.* (2007)) which is similar to the large eddy simulation approach used a in finite volume discretisation. A novel back-flow stabilization algorithm (Esmaily-Moghadam *et al.* (2011)) allowed the prescription of a Neumann boundary condition at the inlet (see Boundary conditions, Section 3.2.5). All simulations were run in parallel on the Certainty cluster at the Center for Turbulence Research, Stanford University, using 240 processors.

3.2.4 Assumptions

We consider the case of steady inhalation at a constant flow rate. Modelling the full respiratory cycle would have added significant complexity to both the simulation and interpretation of the data. It seems intuitive that patients would feel the most discomfort during inhalation given that some have described the sensation that 'their nose feels too open, yet they cannot seem to properly inflate the lungs' (Houser (2007)). The average residence time of

air in this nasal cavity at the proposed condition (see Boundary conditions, Section 3.2.5) is approximately 0.26 s compared to typical inhalation time of 1.5 s (Tobin *et al.* (1983)). The average residence time is approximately 6 times smaller than typical inhalation time, making the steady approximation appropriate. Keyhani *et al.* estimated a Strouhal number of 0.2 for nasal breathing and used this to justify a quasi-steady assumption (Keyhani *et al.* (1995)). Additionally, Doorly *et al.* estimated Strouhal and Womersley numbers to be less than 0.25 and 3 respectively, suggesting that a quasi-steady approximation is valid (Doorly *et al.* (2008)). The Srouhal and Womersley numbers are defined as

$$\mathrm{St} = \frac{2\pi f l}{U}, \tag{3.3}$$

$$\mathrm{Wo} = \frac{D_h}{2}\left(\frac{2\pi f}{\nu}\right)^{1/2}, \tag{3.4}$$

where f is resting breathing frequency, l is a length scale (the length of the nasal cavity in this case), D_h is the average hydraulic diameter of the nasal cavity, and U is a velocity scale (the average fluid bulk velocity in this case). The average hydraulic diameter was defined as

$$D_h = \sqrt{\frac{4V}{\pi L}}, \tag{3.5}$$

where V is the volume of the nasal cavity and L is the length of the nasal cavity. Hörschler *et al.* (Hörschler *et al.* (2010)) and Lee *et al.* (Lee *et al.* (2010)) tested the validity of the quasi-steady assumption by comparing unsteady simulations with steady ones at various instantaneous flow rates. Both found that while there were differences between the unsteady and steady simulations, these differences were most pronounced during the transition between inspiration and expiration. During the inspiration phase, the steady and unsteady results appeared comparable.

The effects of buoyancy on the flow physics in the nose were ignored for the purposes of this study. The Richardson number was calculated to

be a maximum of approximately 0.025 for the present simulations. Hence, buoyancy effects are about 40 times less important than inertial effects and can safely be ignored. The Richardson number was defined as

$$\mathrm{Ri} = \frac{gl\,(\rho_2 - \rho_1)}{\rho_1 U^2}, \tag{3.6}$$

where g is acceleration due to gravity, l is the relevant length scale (average hydraulic diameter, D_h in this case), ρ_1 and ρ_2 are the maximum and minimum densities seen in the flow respectively, and U is a relevant velocity scale (again the average fluid bulk velocity in this case).

The Prandtl number (Equation 3.7) compares momentum diffusivity and heat diffusivity in a fluid. For the air used in the present simulation (properties of air were taken at 25°C, see Table 3.1) the Prandtl number was approximately 0.7. The Schmidt number (Equation 3.8) similarly compares momentum diffusivity with mass diffusivity of water in air in this case. For the present simulation the Schmidt number was approximately 0.6. Both were less than one meaning that viscous effects were important at smaller scales than heat and mass diffusivity. This has the implication that if the fluid motion is sufficiently resolved then heat and water transport will also be sufficiently resolved. The Prandtl and Schmidt numbers are defined as

$$\mathrm{Pr} = \frac{\mu}{\rho\alpha_T}, \tag{3.7}$$

$$\mathrm{Sc} = \frac{\mu}{\rho\alpha_w}, \tag{3.8}$$

where μ is the dynamic viscosity, α_T is the thermal diffusivity, and α_w is the molecular diffusivity of water in air.

3.2.5 Boundary conditions

Walls

The walls of the nasal cavity were specified as Dirichlet boundary conditions for the Navier-Stokes and the scalar advection-diffusion equations. Fluid ve-

Property	Value
Density, ρ	1.18 kg/m^3
Dynamic viscosity, μ	1.84×10^{-5} kg/m s
Thermal diffusivity, α_T	2.22×10^{-5} m^2/s
Molecular diffusivity of water in air, α_w	2.56×10^{-5} m^2/s

Table 3.1: Properties of air at 25°C (Çengel *et al.* (2012); Hall & Pruppacher (1976)).

locity was set to zero to satisfy the no-slip condition. The temperature was set to 31.7°C based off the mean temperature of the nasal mucosa measured during inspiration (Lindemann *et al.* (2002)). Water concentration was set to 3.33×10^{-2} kg/m^3 on the walls inside the nose, transitioning smoothly to 6.91×10^{-3} kg/m^3 at the nasal vestibule, shown in Figure 3.1(c). These concentrations correspond to 100% relative humidity at 31.7°C (Jones (1994)) inside the nose to represent damp mucosa and an equivalent water concentration to the incoming air outside the nose (see Inflow).

Inflow

A rectangular prism-like section in front of the nose was used to provide a realistic inflow condition to the nostrils (Figure 3.1(b)). The outer surfaces of this box were specified as Neumann boundary conditions for the Navier-Stokes equations, corresponding physically to a zero pressure inlet. This inlet condition allowed air to be driven by the outflow condition and be sucked through the geometry. Such a boundary condition mitigates inaccuracies that would be caused by specifying a velocity profile at the inlet, and more closely matches the physics of real inhalation. Boundary conditions for temperature and water transport were treated as Dirichlet boundary conditions with a temperature of 25°C and water concentration of 6.91×10^{-3} kg/m^3 (30% relative humidity (Jones (1994))), corresponding to the ambient air used in the experiments of Lindemann (Lindemann *et al.* (2002)) from which the mucosa temperature was chosen. The material properties for air were taken at 25°C and are presented in Table 3.1.

Outflow

The section attached to the outflow boundary was artificially extended from the back of the nasal geometry to reduce any impact the outflow may have on the fluid flow in the region of interest. The outflow condition was set as a Dirichlet condition for the Navier-Stokes equations with a flow rate of 250 ml/s, which corresponds to the mean inspiratory flow rate associated with nasal breathing at resting conditions (Tobin *et al.* (1983)). The imposed flow rate was constant, modelling a steady inspiration. Despite the fact that the imposed boundary conditions are time-independent, the solution is unsteady. Unsteadiness of the solution is accounted for in our computations by solving time-dependent Navier-Stokes and advection-diffusion equations. The source of unsteadiness, as discussed in the Results section (Section 3.3), is the instabilities caused by shear layers inside the nasal cavity. Temperature and water transport were treated as Neumann boundaries of zero gradient at the outlet.

3.2.6 Mesh-independence analysis

Multiple mesh resolutions of the pre-surgery geometry of patient 1 were generated and compared to assess the sensitivity of the flow solution to variations in mesh size. The two mesh length scales that were found to have the most impact on the solution were the height of the first anisotropic layer and the size of the triangles in the surface mesh. These were varied independently and shown in Figure 3.2 as y^+ refinement and surface refinement, respectively.

At the highest surface resolution, the outlet pressure, mean wall shear stress, and total wall heat loss show little sensitivity to refinement. However, as the first anisotropic layer height is refined, the mean wall shear stress converged very slowly (Figure 3.2(b)). Computational effort became a limiting factor at the highest resolution shown here, and the independence study was stopped. But it does appear that the mean wall shear stress was almost mesh independent at this resolution. The highest resolution case presented in Figure 3.2 was used for the remainder of this study.

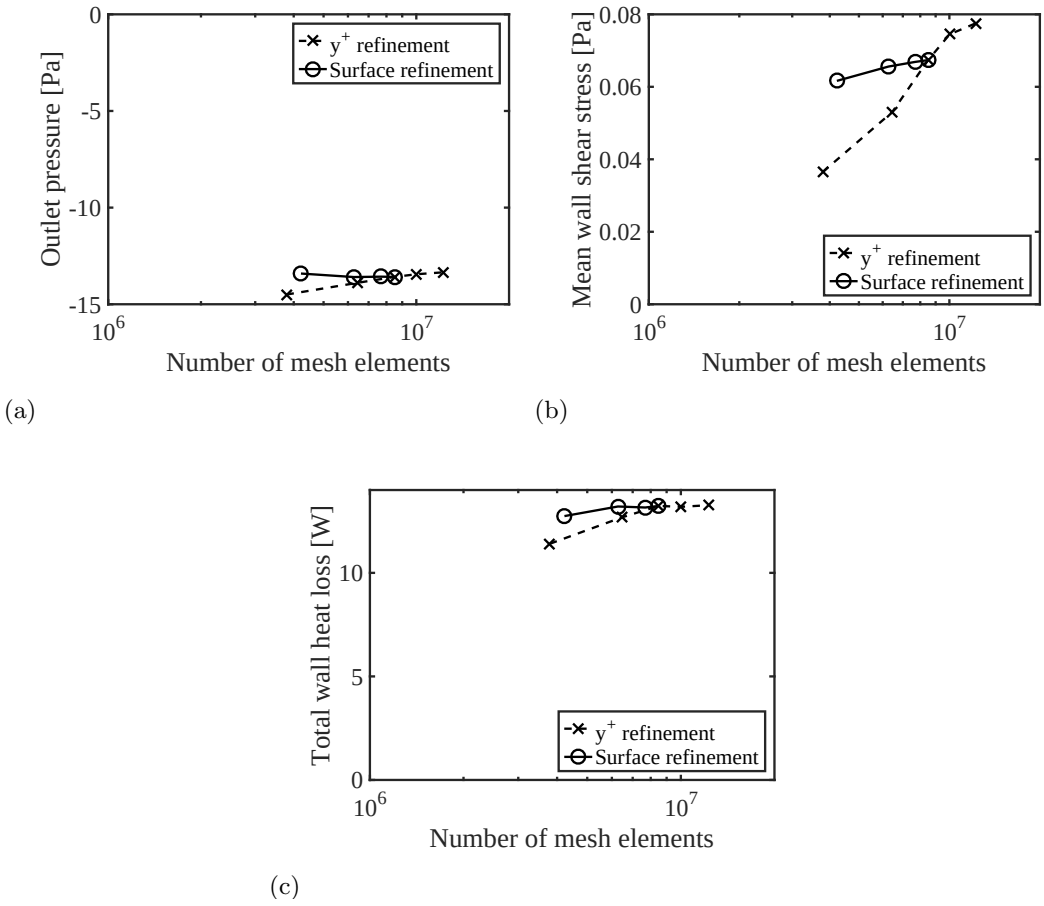

Figure 3.2: Mesh-independence study for: (a) pressure, (b) wall shear stress, and (c) heat loss. As the gradient approaches zero, the problem approaches mesh independence.

3.2.7 Validation

Given the complex and patient specific geometry of the nasal airways, validation of a nasal CFD simulation is difficult without complementary experimental work to compare to. For this study, some relevant metrics were calculated and compared to some found in the literature from similar simulations or *in vivo* testing, these are presented in Table 3.2.

Nasal resistances compare well with literature values. The *in vivo* study of Pallanch *et al.* (Pallanch *et al.* (1985)) reveals large variation in normal nasal resistance values. Even with this large range of normal values, the nasal resistance computed for the normal nose sits within the normal range while that of the ENS noses sit below the normal 95% confidence interval. This is what one would expect and highlights the lack of resistance observed in ENS patients (Houser (2007)).

The mean sensible heat fluxes computed in the present simulations are slightly below that seen in the literature, though not unreasonably so. The majority of the literature cases used an inlet temperature below the present simulation, 20°C compared to 25°C used here, and a mucosa temperature higher than the present simulation, 32.6°C compared to 31.7°C used here. Therefore the slightly higher heat fluxes seen in the literature is justified.

Heat flux due to the evaporation of water accounts for about 90% of the total heat flux through the nasal mucosa. So the calculated mean heat flux and mean water flux show similar relationships with the literature and both slightly below the literature values. Garcia *et al.* (Garcia *et al.* (2007)), which was used for this comparison, used a lower inlet temperature, a higher mucus temperature and a higher inlet relative humidity. Despite this, the difference between the absolute humidity at the inlet and that at the wall is very similar to the present simulation so they should be a good comparison. The present simulation is below the Garcia's data by a maximum of approximately 20%. Despite this difference the present simulation data seems reasonable, variations from Garcia are likely due to geometrical differences.

Case	Property	Simulation	Literature
Normal	Nasal resistance [Pa s/ml]	0.088	0.039 - 0.082 [**1**] 0.049 - 0.28 (95% CI)[**4**] 0.046 [**5**]
	Mean total heat flux [W/m^2]	734	855 - 1205 [**1**]
	Mean water flux [kg/m^2 s]	2.7×10^{-4}	3.04 - 4.3×10^{-4} [**1**]
	Mean wall shear stress [Pa]	0.11	0.0695 [**5**]
ENS	Nasal resistance [Pa s/ml]	0.036 - 0.037	0.084±0.031 (±SD)(ITR)[**2**] 0.028 (ENS)[**1**]
	Mean sensible heat flux [W/m^2]	71 - 92	150 - 250 (ITR)[**3**] 217±24 (±SD)(ITR)[**2**]
	Mean total heat flux [W/m^2]	750 - 953	975 (ENS)[**1**]
	Mean water flux [kg/m^2 s]	2.8 - 3.5 $\times10^{-4}$	3.46×10^{-4} (ENS)[**1**]
	Mean wall shear stress [Pa]	0.058 - 0.061	0.127±0.036 (±SD)(ITR)[**2**]

Table 3.2: Comparison with literature. (ENS) - Empty nose syndrome geometry, (ITR) Inferior turbinate resection geometry. Present simulation: flow rate: 250 ml/s; inlet temperature: 25°C; inlet relative humidity: 30%; mucosal temperature: 31.7°C. **References**: [**1**] Garcia *et al.* (2007) (normal: n=4; ENS: n=1) *in silico*; flow rate: 250 ml/s; inlet temperature: 20°C; inlet relative humidity: 50%; mucosal temperature: 32.6°C. [**2**] Kimbell *et al.* (2013) (n=10) *in silico*; flow rate: 300±50 ml/s (±SD); inlet temperature: 20°C; mucosal temperature: 32.6°C. [**3**] Sullivan *et al.* (2014) *in silico*; (n=10) flow rate: *unknown (two times patient minute volume)*; inlet temperature: *unknown*; mucosa temperature: 32.6°C, [**4**] Pallanch *et al.* (1985) (n=80) *in vivo*; flow rate: 200 ml/s, [**5**] Wen *et al.* (2008) (n=1) *in silico*; flow rate: 250 ml/s.

The mean wall shear stress does not appear to agree very well with the literature with errors near 50%. This, however, is likely due to the large variation in nasal geometry seen in the human population. For the normal case, the simulated mean wall shear stress is higher than that of Wen *et al.* (Wen *et al.* (2008)), though so is nasal resistance by a similar proportion. Compared to the *in vivo* data, the nasal resistance of Wen *et al.* is very low. Similarly in the ENS case, the simulated mean wall shear stress is lower than that of Kimbell *et al.* (Kimbell *et al.* (2013))) by a similar proportion that the nasal resistances differ. While the metrics for the ITR geometries simulated by Kimbell *et al.* suggest they are closer to a normal nose than an ENS nose all the nasal resistance values seem to make sense, and their relationship to the mean wall shear stress provides confidence that the present simulation can produce reasonable results.

Finally, simulated temperatures at various locations in the normal nasal cavity were compared to the *in vivo* study by Keck *et al.* (Keck *et al.* (2000)) and presented in Figure 3.3. The experimental temperature data are compared to the CFD temperature averaged over the coronal plane at each location. The data matches quite well, the simulated data remains within approximately one standard deviation of the *in vivo* data at the majority of the data points for both temperature and relative humidity. A couple of minor discrepancies can, however, be observed. First, the simulated temperature data increases at a slower rate than the mean of the *in vivo* data. This is because of the mucosal wall temperature being set to 31.7°C throughout the nasal cavity in the simulation when, in reality, the mucosal temperature would be slightly cooler anteriorly and slightly hotter posteriorly. The simulated relative humidity increases slightly faster than the mean of the *in vivo* data with the final data point at 6 cm more than one standard deviation above the mean. This may be due to the lower temperature on the mucosal surface in the simulation at this location lowering the water vapour concentration required for saturation, or it could indicate an over-active evaporation modelling approach. Regardless, the data shows very good agreement, resulting in a temperature profile that would appear physically plausible.

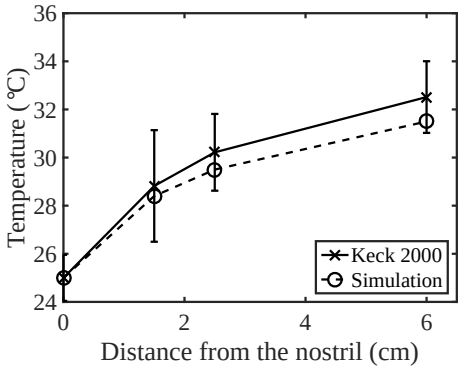

(a)

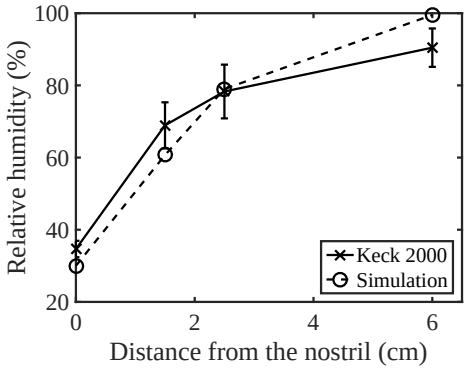

(a)

Figure 3.3: Comparison of the present simulation of a normal nose with temperature and humidity data from Keck *et al.* (2000) (mean±SD).

3.3 Results

3.3.1 Patient information

In total, six nasal geometries of three subjects have been simulated.

Normal subject

Male, 24 years old. Subject had no history of nasal disease and presents a normal nasal cavity except for an asymptomatic septal deviation.

Patient 1

Female, 32 years old. Patient 1 had a history of chronic sinusitis and primary ciliary dyskinesia. The patient had previously undergone sinus surgery which had removed much of their turbinate tissue leaving a cavernous nasal cavity. They experienced bilateral frontal headaches, chronic post-nasal drip, chronic bilateral nasal obstruction, bilateral aural fullness and hearing loss. A CT scan of this condition was available and will be referred to as the pre-surgery case for this patient.

The patient underwent an SIS graft turbinate reconstruction. A CT scan

following this surgery was collected and will subsequently be referred to as the post-surgery case for this patient. Following surgery, they reported a normal quality of breathing and were less depressed, though frontal sinus pressure and pain were still present.

The patient then underwent further endoscopic sinus surgeries which improved her sense of smell while the frontal headache remained. Unfortunately a CT scan was not available for this case and it could not be simulated. This surgery is mentioned here to highlight that further improvement beyond the first surgery was possible and it is presently unlikely that a single surgery can result in full treatment of symptoms for ENS patients.

Summary:

- **Pre-surgery** - history of sinus surgery and other sinus disease. ENS symptoms.
- **Post-surgery** - following SIS graft turbinate reconstruction.

Patient 2

Male, 48 years old. Patient 2 presented with a sensation of nasal obstruction bilaterally, although there was no problem with airflow. They had a history of septoplasty and turbinate reduction. A CT scan of this case was available and will be referred to as the pre-surgery case for this patient.

Patient 2 underwent an SIS graft turbinate reconstruction along with an inferior turbinate in-fracture. A CT scan of this case was taken and used as the post-surgery-1 case for this patient. The patient reported significant improvement in ENS symptoms and quality of life following this procedure, though they noted that there was "still room for improvement" as the patient's sleeping patterns were still affected.

The patient underwent a further procedure in which Alloderm implants were placed on the lateral inferior walls of the nasal cavity. This procedure resulted in a larger modification of the nasal geometry and the patient reported further improvement in symptoms. This case will be referred to as the post-surgery-2 case for this patient.

This patient noted that after each procedure a peak benefit was observed 4-6 weeks post-operation, after which some, but not all, of the benefits receded.

Summary:

- **Pre-surgery** - history of septoplasty and turbinate reduction. ENS symptoms.
- **Post-surgery-1** - following SIS graft turbinate reconstruction and inferior turbinate in-fracture.
- **Post-surgery-2** - following Alloderm implants.

3.3.2 Quantification of symptoms

Validated questionnaires are useful for quantifying patient symptoms and identifying patients with various conditions. Symptoms are quantified by asking patients to rate the severity of each symptom on a five point scale, five being extremely severe and zero being not a problem at all. Quantifying patient symptoms allows the tracking of symptoms and quality of life over time following clinical intervention. One of the most commonly used validated questionnaires in the field of rhinology is the sino-nasal outcome test 22 (SNOT-22) (Rudmik *et al.* (2015); Hopkins *et al.* (2009)).

More recently, an ENS specific questionnaire was validated, the empty nose syndrome 6-item questionnaire (ENS6Q)(Velasquez *et al.* (2016)). This questionnaire is targeted to ENS specific symptoms making it a useful tool for identifying ENS and quantifying quality of life in these patients.

Both questionnaires were completed throughout the treatment timeline by both patients and accumulated results are shown in Figure 3.4. Both patients completed the SNOT-22 and ENS6Q at their pre-surgery state (0 months). Patient 1 then completed the questionnaires again three months after the operation (post-surgery state) and also 12 months after the initial procedure but after further surgical intervention. Patient 2 completed them

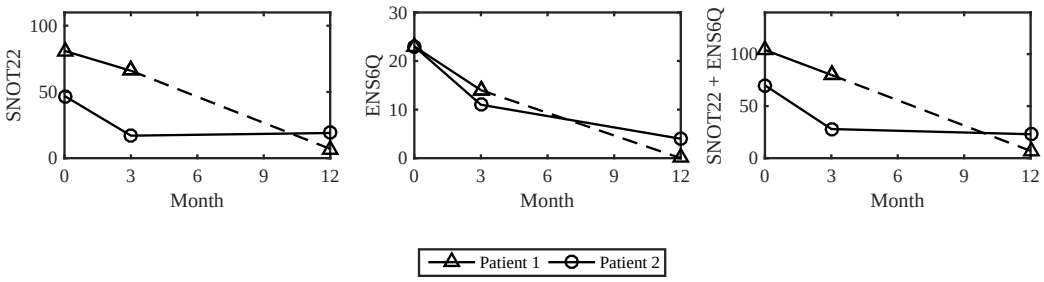

Figure 3.4: Accumulated scores for the SNOT-22 and ENS6Q questionnaires following surgery, a higher score indicates more severe symptoms. Zero months corresponds to the pre-surgery state. The dashed line for patient 1 indicates that further surgery was performed during this time, the geometry following this surgery was not simulated here. Results following Patient 2, surgery 2 are not shown.

at three and again at 12 months following his first procedure (post-surgery-1). Their second surgery occurred after this time, of which no questionnaire data was available (post-surgery-2).

At the pre-surgery state, Patient 1 had a higher SNOT-22 score while both patients had similar ENS6Q scores. This shows that both patients had similar ENS specific symptoms to begin with, while patient 1 presented with more non-ENS specific symptoms, reflecting the patient's history of chronic sinusitis and primary ciliary dyskinesia.

Both patients improved following surgery. Patient 1 reported a large improvement in ENS specific symptoms but only a small improvement in SNOT-22 score. The small SNOT-22 improvement was still larger than the minimal clinically important difference for the SNOT-22, indicating that non-negligible improvement in these symptoms was observed. At 12 months, and after additional surgery, not simulated here, this patient showed a large further improvement on both questionnaires.

For both questionnaires, patient 2 showed significant improvement three months following the first surgery (post-surgery-1 case). At 12 months minimal further improvement was observed, though much of the benefits seen at three months remained.

Question specific responses for each questionnaire are presented in Figures 3.5 and 3.6. At the post-surgery case, three months after surgery, Patient 1 reported little to no change in questions 1-12 of the SNOT-22. These questions target physiological symptoms. However, in questions 13-22, which relate more to quality of life and secondary symptoms, patient 1 showed almost uniform improvement. Patient 1 also responded with improvement to all but one ENS6Q question, dryness. Their responses to all three questions related to the paradoxical sensation of nasal obstruction: 'absence of airflow sensation', 'suffocation', and 'nose is too open', improved significantly despite the patient's response to 'nasal obstruction' in the SNOT-22 not changing over this period. This discrepancy highlights the difficulty associated with understanding the subjective symptom profile of ENS.

Patient 2 also responded with more changes in the last 10 questions of SNOT-22 than the first 12. They had previously reported that they felt the most improvement four to six weeks following surgery. This may be reflected in the three month improvement seen in the sleep related questions (questions 13-16) followed by a slight relapse by the 12 month questionnaire. It is interesting to note that these responses appear to correlate inversely with the patient's response to: 'need to blow nose', and 'thick nasal discharge'. Patient 2 also noted significant improvement in ear related symptoms 'ear fullness', 'dizziness', and 'ear pain'. Additionally, an increase in 'nasal obstruction' was reported at 12 months despite all ENS6Q metrics decreasing.

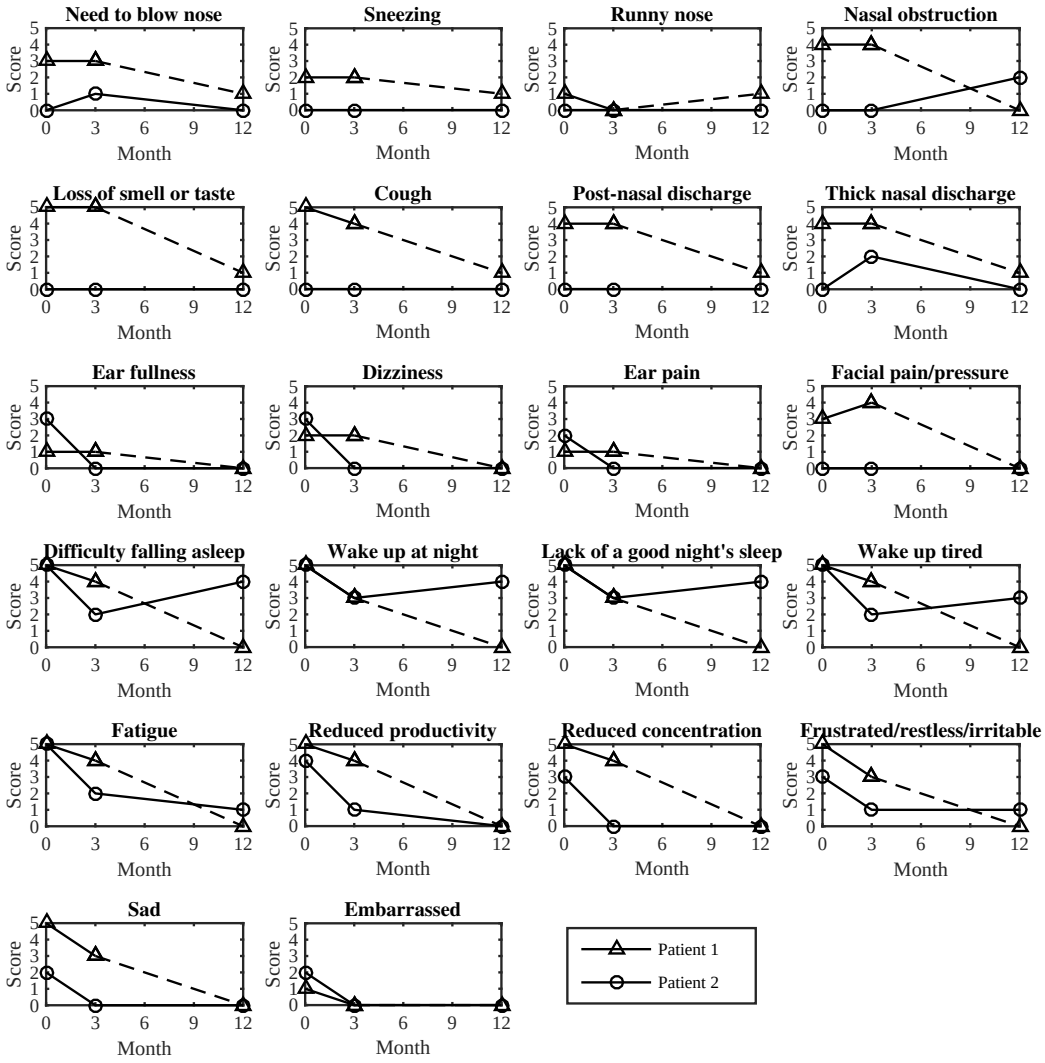

Figure 3.5: Individual symptom scores of the SNOT-22 questionnaire following surgery. A score of five corresponds to extremely severe and a score of zero indicates no problem. Zero months corresponds to the pre-surgery state. The dashed line for patient 1 indicates that further surgery was performed during this time, the geometry following this surgery was not simulated here. Results following Patient 2, surgery 2 are not shown.

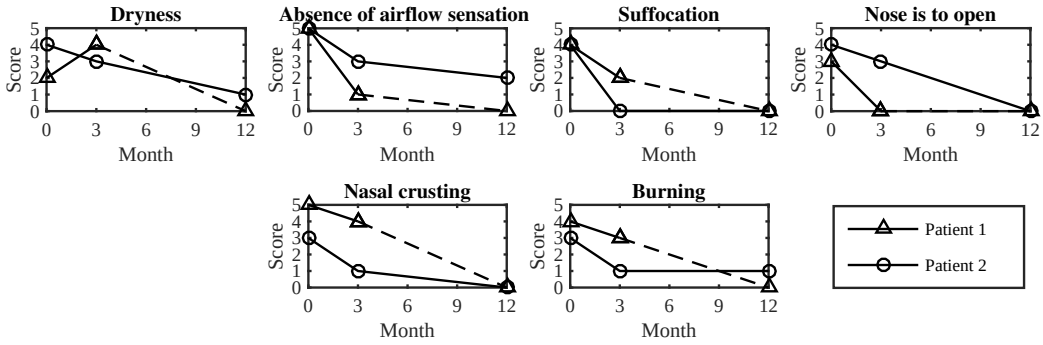

Figure 3.6: Individual symptom scores of the ENS6Q questionnaire following surgery. A score of five corresponds to extremely severe and a score of zero indicates no problem. Zero months corresponds to the pre-surgery state. The dashed line for patient 1 indicates that further surgery was performed during this time, the geometry following this surgery was not simulated here. Results following Patient 2, surgery 2 are not shown.

3.3.3 Nasal cavity visualization

Figures 3.7 through 3.11 show left and right projections of each side of the nasal cavity for each nasal geometry. The left two columns show the lateral and medial side of the right nasal cavity, the right two columns show the medial and lateral sides of the left nasal cavity. They are arranged in rows corresponding to each simulated nasal geometry. All results are time averaged over a time interval equivalent to the average residence time in the geometry following three residence times to allow the flow to develop. This was sufficient to capture wall averaged quantities to within at least 0.5%.

Stream tracers through each geometry are presented in Figure 3.7. The normal nose (Figure 3.7(a)) exhibited orderly and smooth stream traces through the majority of the nasal cavity. The exception to this was in the nasopharynx, towards the rear of the nasal cavity, where a wake was generated behind the inferior turbinate and the air turned downwards towards the artificial trachea.

In both cases, patient 1 (Figure 3.7(b) and(c)) showed a jet of air which traversed the nasal cavity from the nostrils to impinge on the posterior wall. After impingement, large scale recirculation was generated superiorly in the

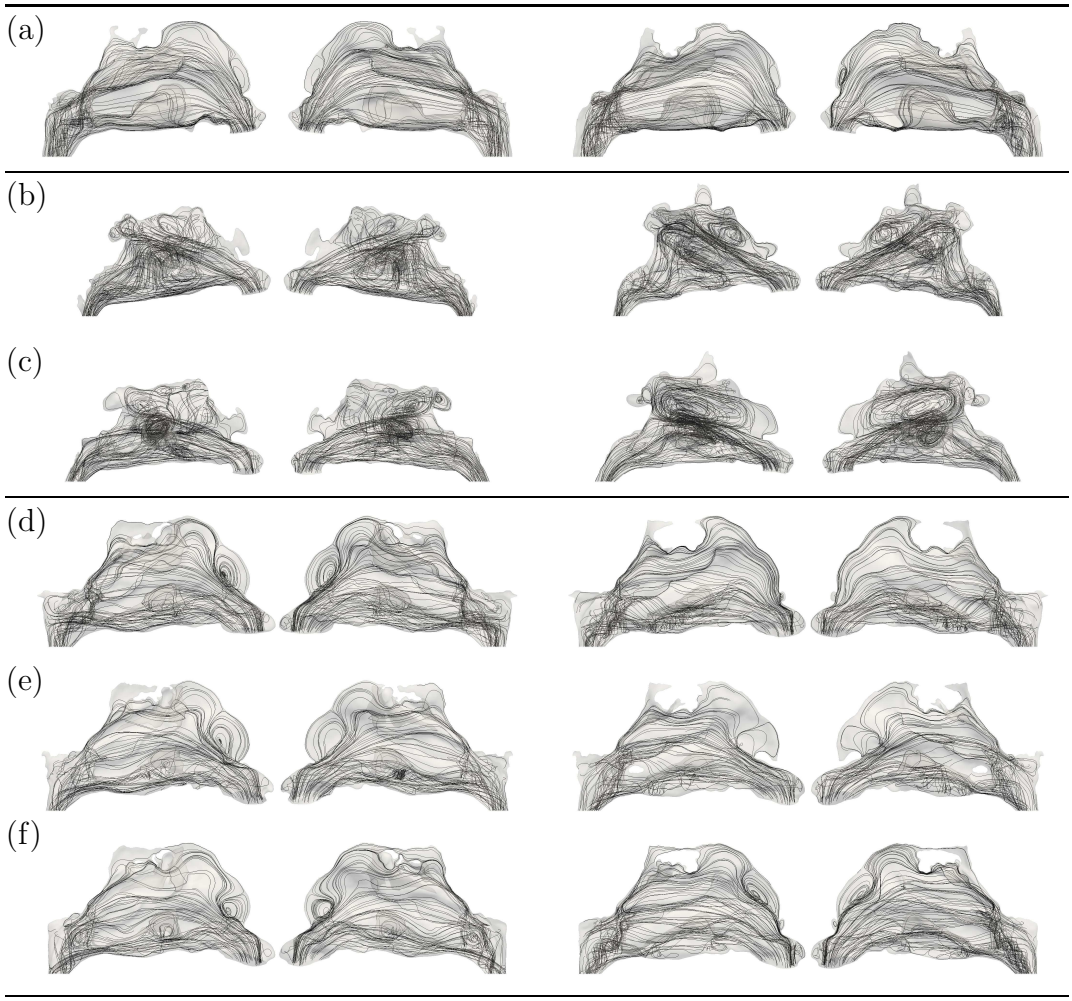

Figure 3.7: Stream tracers of each case, viewed from both the lateral and medial sides of each nasal cavity. The stream tracers were calculated from time averaged flow fields. (a) normal, (b) patient 1 pre-surgery (with ENS), (c) patient 1 post-surgery (improved symptoms), (d) patient 2 pre-surgery (with ENS), (e) patient 2 post-surgery 1 (improved symptoms), (f) patient 2 post-surgery 2 (improved symptoms).

left nasal cavity while disorganised flow was generated superiorly in the right cavity. This patient had a very cavernous nasal cavity with almost no identifiable turbinate tissue left to obstruct the flow of air as it travels through the nasal cavity, resulting in this jet phenomenon. Following surgery (Figure 3.7(c)) the jet was shifted downwards, impinging lower on the posterior wall, creating larger superior recirculation, and perhaps guiding more unobstructed air through the lower part of the nasal cavity down into the nasopharynx. As a result of previous sinus surgery, patient 1 had a large ostium connecting the maxillary sinuses to the nasal cavity, and hence the maxillary sinuses were included in the simulation. Circulating airflow inside the maxillary sinuses is responsible for the patch of disorganised airflow in the centre of each panel of Figure 3.7(b) and (c).

Patient 2 (Figure 3.7(d), (e), and (f)) showed much smoother and more organised stream tracers than patient 1, resembling that of the normal nose throughout much of the nasal cavity. Disorganised helical flow patterns were present in the lower part of the nasal cavity where the remains of the inferior turbinates sit. In the left nasal cavity, these flow patterns reduced following each surgery. In the right cavity of the pre-surgery case, a low air stream impinged on the rear of the nasopharynx producing a stagnation point and some upwards flow in this region. Following surgery the impingement was no-longer seen.

Figure 3.8 shows the pressure on the nasal surface throughout the nasal cavity for each case. The pressure on the nasal surface in the normal nose (Figure 3.8(a)) transitioned smoothly from near-atmospheric pressure at the nostrils to a lower pressure at the nasopharynx, much lower than any other case. The lower pressure seen here is indicative of the much larger pressure loss across this geometry compared with the abnormal noses, and forms the basis of the statement that ENS patients' sensation of nasal obstruction is paradoxical. Most of the pressure losses occurred in the first half of the nasal cavity in the normal case. Some small areas of higher pressure were created on the front of each inferior turbinate as the air collided with this structure on its way past. The lighting effects in these images reveal a much smoother

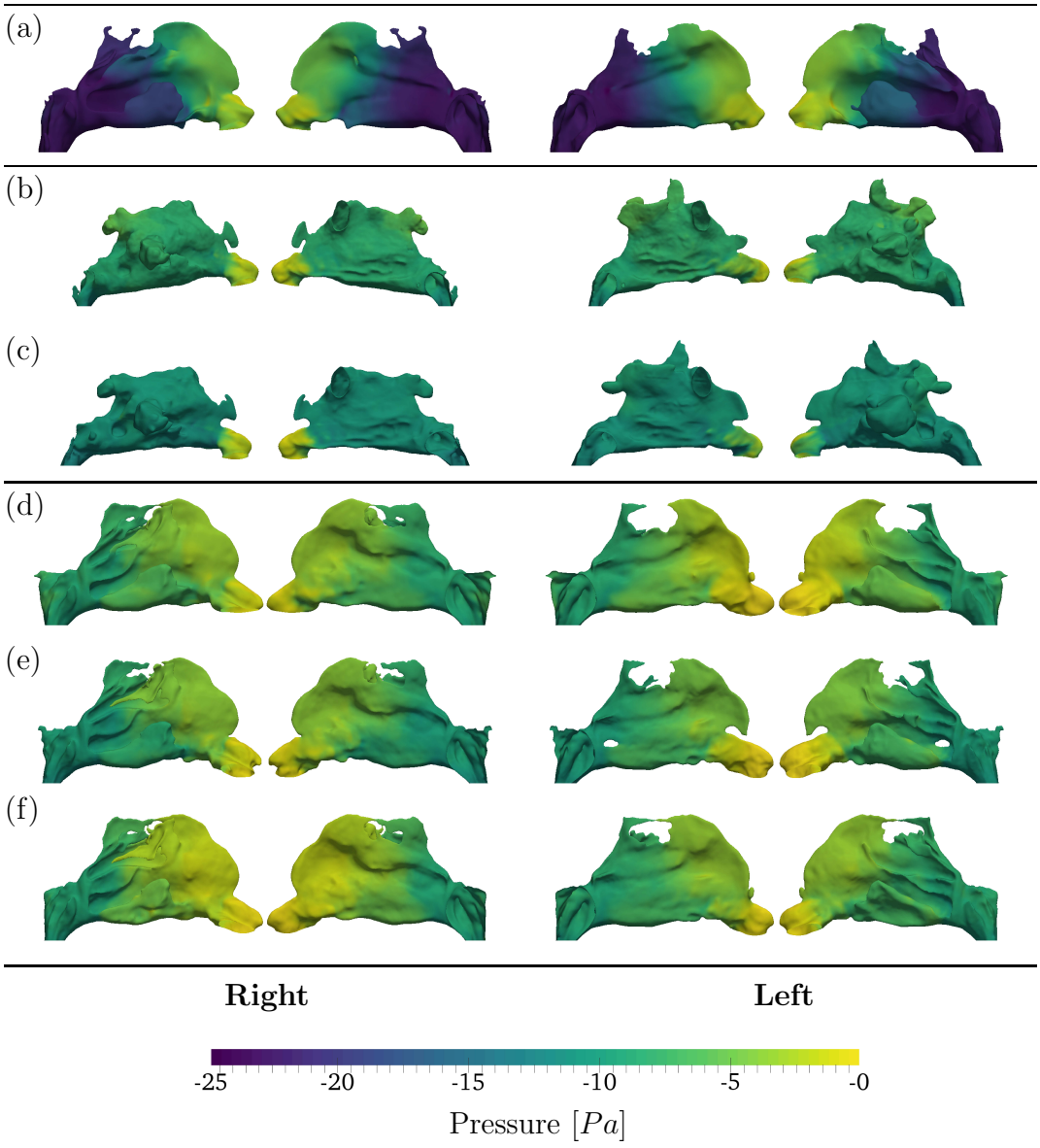

Figure 3.8: Pressure on the nasal surface for each case, viewed from both the lateral and medial sides of each nasal cavity. The results are time averaged. (a) normal, (b) patient 1 pre-surgery (with ENS), (c) patient 1 post-surgery (improved symptoms), (d) patient 2 pre-surgery (with ENS), (e) patient 2 post-surgery 1 (improved symptoms), (f) patient 2 post-surgery 2 (improved symptoms).

septal wall in the normal case when compared to the other geometries in which the septum has been modified by previous surgery.

In contrast to the normal nose, patient 1 had an almost uniform pressure across much of the nasal surface apart from the vestibule and valve area near the front of the nose (Figure 3.8(b)). Most of the pressure losses occurred in the nasal valve, after which the air travels unimpeded into the cavernous nasal cavity. The wall pressure in the post-surgery case was lower than that of the pre-surgery case, implying more pressure losses in the nasal valve following surgery (Figure 3.8(c)). The impinging jet of air manifested as a region of higher pressure on the anterior wall in the pre-surgery case, which became less prevalent in the post-surgery case.

In all cases, patient 2 had a much smoother surface pressure profile, similar to that seen in the normal nose but with a higher pressure at the outlet (Figures 3.8(d)-(f)). In the pre-surgery case an area of higher pressure was produced on the rear wall of the nasopharynx where the airflow impinges on the wall, as was seen in Figure 3.7. This is close to where the auditory tube reaches the nasopharynx, connecting the nasal cavity to the middle ear. Abnormal pressures here may have played a role in this patient's ear related symptoms. The stagnation was not present following surgery and the ear related symptoms disappeared (Figure 3.5). Surface pressure near the inferior turbinate reduced following surgery 1, recovering on the right side following surgery 2. In the pre-surgery case surface pressures in the left cavity were higher than the right, swapping by post-surgery-2. This shift may indicate a shift in the distribution of airflow between the two cavities.

Both sensible and latent heat flux through the nasal surface could be calculated and combined to give the total heat flux, $\dot{q}$, as in Equation 3.9.

$$\dot{q} = -k\nabla T + \dot{q}_{water}\Delta\mathcal{H}, \tag{3.9}$$

where k is the thermal conductivity of air, T is the temperature, and $\Delta\mathcal{H}$ is the latent heat of evaporation of water. The water vapour flux, $\dot{q}_{water}$, is defined as

$$\dot{q}_{water} = -\alpha_w \nabla C, \tag{3.10}$$

where C is the water vapour concentration.

The total heat flux through the nasal wall for each case was calculated and are compared in Figure 3.9. In the normal nose, the majority of the heat flux occurred in the anterior half of the nasal cavity and was evenly distributed on both the septal and lateral walls (Figure 3.9(a)). Regions of higher heat fluxes occurred on the front of the inferior turbinate and in the nasal valve region.

The majority of heat flux in patient 1's nose occurred in a comparatively smaller region beginning in the nasal valve and extending posteriorly with the jet of air seen earlier (Figure 3.9(b)). A region of higher heat flux on the posterior nasal walls resulted from the jet impingement in the pre-surgery case. Following surgery the corresponding impingement heat fluxes moved anteriorly slightly and lower in the nasal cavity, shadowing the air jet's position seen earlier (Figure 3.9(c)).

It was evident in both patients that the uneven surface geometry resulted in patchy and uneven heat flux distributions as compared to the normal case. In this projection all three geometries from patient 2 showed a similar heat flux distribution, with the exception that the majority of the heat flux swapped from the right to the left cavity between pre-surgery and post-surgery-2 (Figure 3.9(d)-(f)). Like the surface pressures implied this could mean that the distribution of airflow between the two cavities swapped. It is difficult to determine if this was a direct result of the surgical procedures or just natural variation in the nasal geometry. An increase in heat flux on the inferior wall of both middle turbinates cannot be seen in this figure but was present in the post-surgery-1 case, while it was limited to just the left side by post-surgery-2. A slight elevation in heat flux was seen at the rear of the nasopharynx in the pre-surgery case, and on the implants on the inferior lateral walls in the post-surgery-2 case. In comparison to the normal case, the nasal walls of patient 2 were exposed to higher heat fluxes posteriorly, with moderate heat fluxes seen along the length of the inferior turbinate in

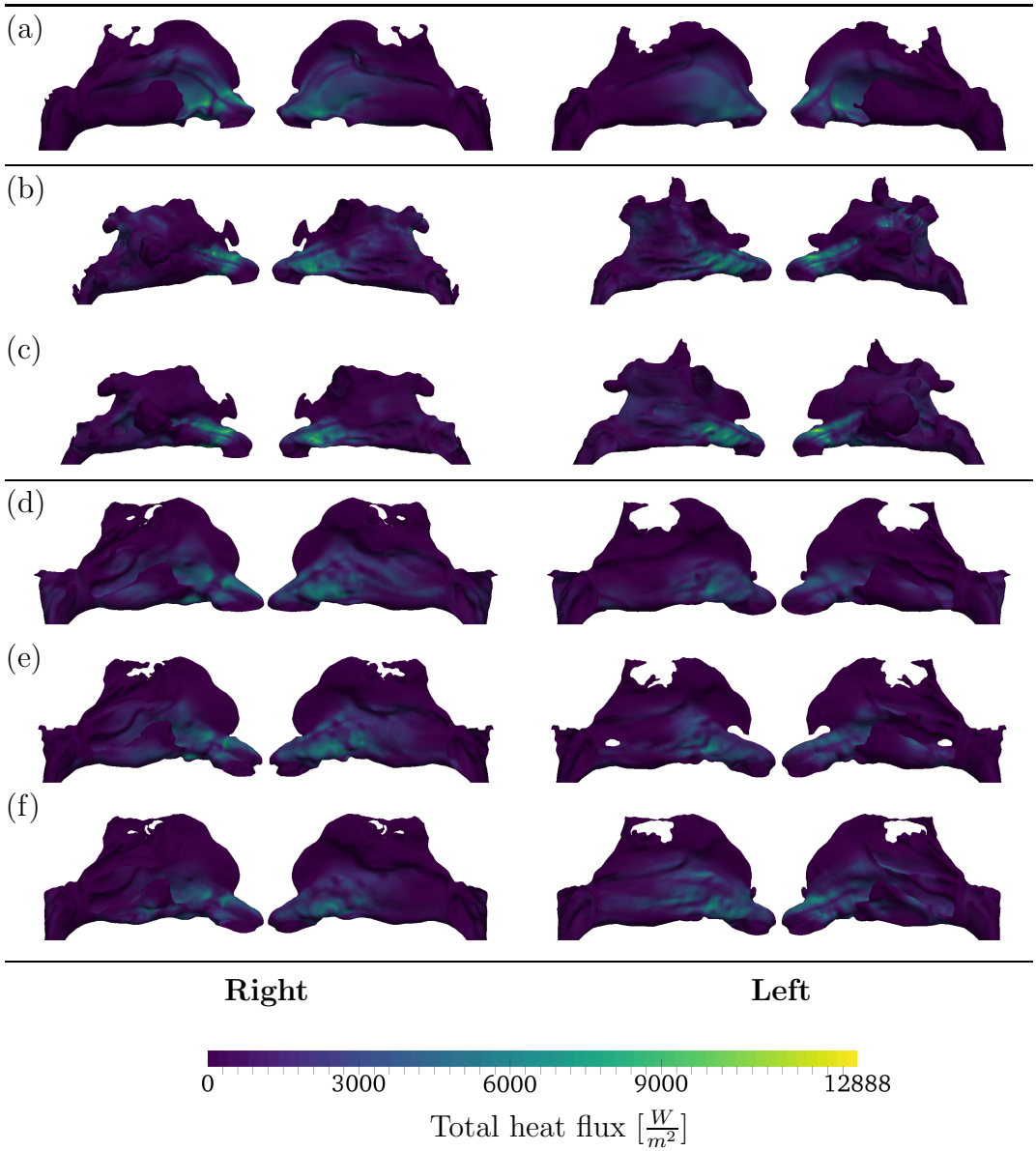

Figure 3.9: Total heat flux through the mucosal surface for each case, viewed from both the lateral and medial sides of each nasal cavity. The results are time averaged. (a) normal, (b) patient 1 pre-surgery (with ENS), (c) patient 1 post-surgery (improved symptoms), (d) patient 2 pre-surgery (with ENS), (e) patient 2 post-surgery 1 (improved symptoms), (f) patient 2 post-surgery 2 (improved symptoms).

most cases.

Nasal dryness is a common symptom in ENS patients (Houser (2007)). Atop of the nasal lining lies a thin layer of mucus which traps particulates, humidifies the incoming air, and facilitates clearance of contaminants by ciliary action (Proctor & Andersen (1982)). Maintenance of this mucus layer is important for proper nasal function and is affected, among other things, by the exchange of water with the incoming air. Water fluxes from the surface of the nose are shown in Figure 3.10, though they are almost identical to the total heat flux distribution which was discussed earlier. This similarity in distributions can be explained by the fact that the latent heat flux accounted for approximately 90% of the total heat flux.

Figure 3.11 shows the wall shear stress throughout the nasal cavity for each geometry. Elevated wall shear stress covered the majority of the normal nasal cavity, spanning the length of the inferior turbinate both superiorly and inferiorly. In contrast, both patients showed much lower wall shear stresses in much of the nasal cavity.

Patient 1 showed concentrated, very high wall shear stress in the nasal valve area, stretching backwards in a narrow band following the internal jet of air. The impingement of this jet gave rise to elevated wall shear stress on the posterior wall which decreased in magnitude and shifted inferiorly following surgery.

Patient 2 had lower shear stresses high in the nasal cavity than the normal case. This was partially recovered by the post-surgery-2 case however, especially on the left side. On the right side, the wall shear stress near the anterior end of the inferior turbinate on both the septal and lateral walls increased following surgery 1, only to decrease again after surgery 2.

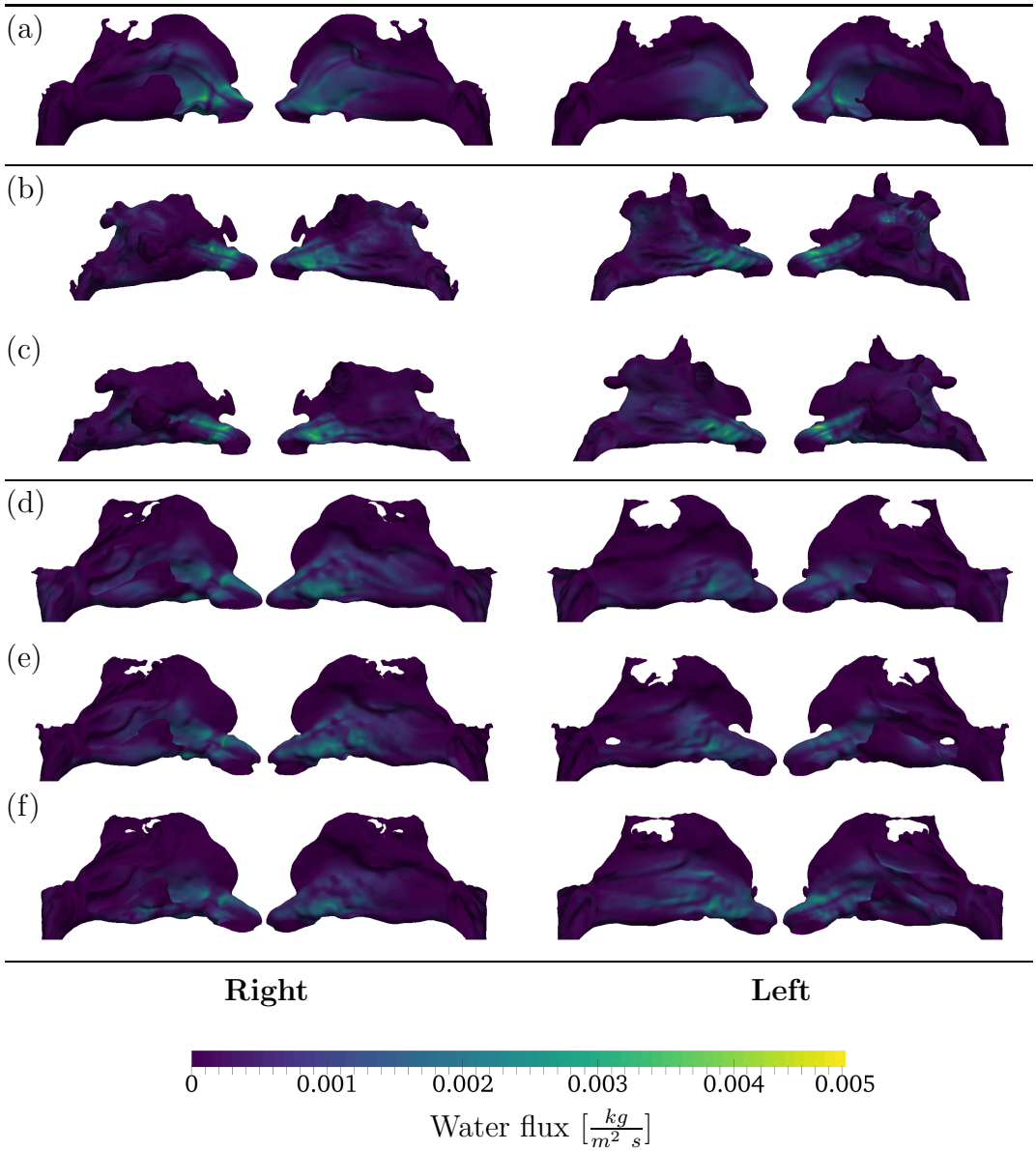

Figure 3.10: Water flux through the mucosal surface for each case, viewed from both the lateral and medial sides of each nasal cavity. The results are time averaged. (a) normal, (b) patient 1 pre-surgery (with ENS), (c) patient 1 post-surgery (improved symptoms), (d) patient 2 pre-surgery (with ENS), (e) patient 2 post-surgery 1 (improved symptoms), (f) patient 2 post-surgery 2 (improved symptoms).

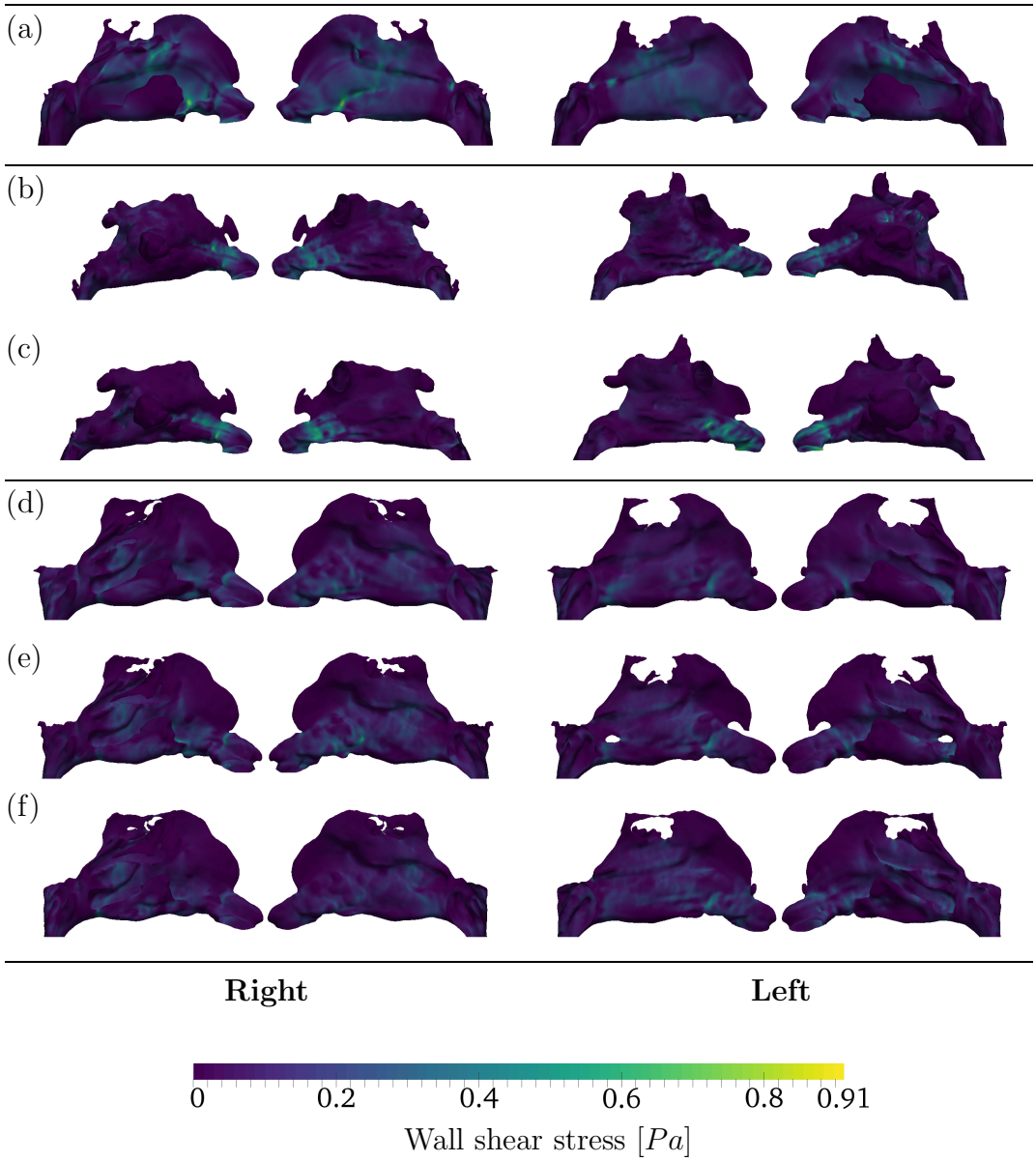

Figure 3.11: Wall shear stress on the mucosal surface for each case, viewed from both the lateral and medial sides of each nasal cavity. The results are time averaged. (a) normal, (b) patient 1 pre-surgery (with ENS), (c) patient 1 post-surgery (improved symptoms), (d) patient 2 pre-surgery (with ENS), (e) patient 2 post-surgery 1 (improved symptoms), (f) patient 2 post-surgery 2 (improved symptoms).

3.3.4 Flow field visualisation

To visualise the flow field inside each nasal cavity, Figures 3.12 to 3.15 present the flow field as a number of coronal slices equally spaced between the nostrils and the nasopharynx. Not only does this allow the visualisation of the flow field, the cross-sections make it easy to see how each geometry changed following surgery. Once again, all results are time averaged over a time interval equivalent to the average residence time in the geometry following three residence times to allow the flow to develop.

The normal nose has thin nasal passages throughout the majority of the nasal cavity, and full inferior and middle turbinates are visible.

In contrast, Patient 1 lacks almost all evidence of the turbinates apart from a couple of stubs hinting at their previous location. This nasal cavity is extremely open and cavernous in sharp contrast to the normal case. The effect of surgery can be seen most easily in the fifth and sixth slices were a couple of bulges can be seen on the floor of the nasal cavity following surgery, these are the SIS graft reconstructions.

The nasal cavity in Patient 2, however, bears much more resemblance to the normal nose throughout much of the nasal cavity. It can clearly be seen that this patient lacks much of their inferior turbinate along the length of the cavity, resulting in a large open space where they used to be. It seems also that posteriorly in the nasal cavity the superior cavities are restricted and show fewer clear passages than the normal case. The first surgery involved turbinate in-fracture and SIS graft turbinate reconstruction. Both can clearly be seen in the fourth and fifth slice where the turbinates have become enlarged and point more medially than the pre-surgery case. Surgery 2 introduced Alloderm implants which are seen in slices five to seven as bulges on the lateral inferior wall in the post-surgery-2 case.

The velocity normal to the coronal plane, in the posterio-anterior direction, are shown in Figure 3.12. Positive velocity is out of the page, towards the nostrils, the bulk flow is moving in the negative direction.

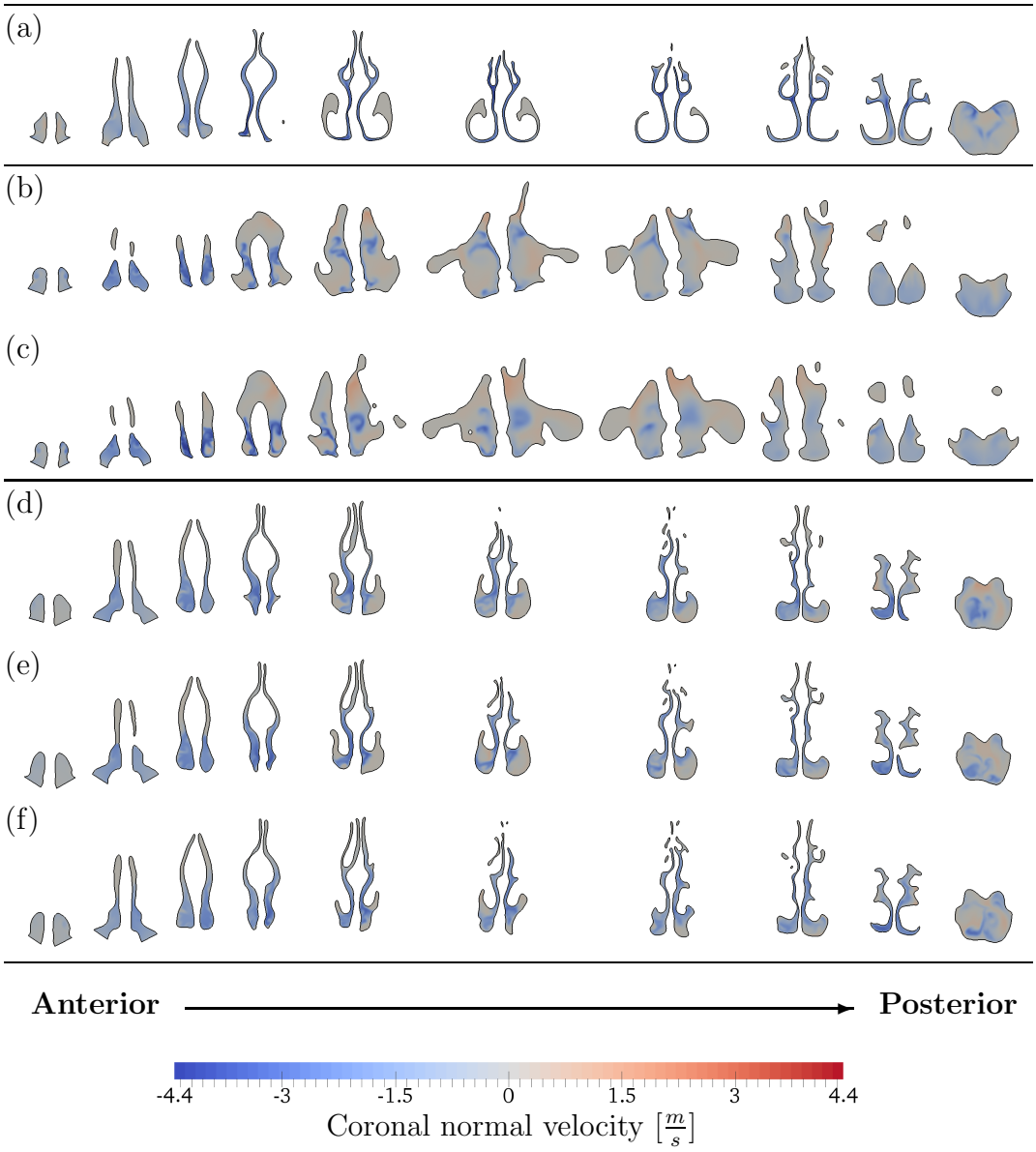

Figure 3.12: Velocity component normal to the coronal plane for each case, positive is out of the page (towards the nostril). Velocities are viewed on equally spaced coronal slices through the nasal geometry. The results are time averaged. (a) normal, (b) patient 1 pre-surgery (with ENS), (c) patient 1 post-surgery (improved symptoms), (d) patient 2 pre-surgery (with ENS), (e) patient 2 post-surgery 1 (improved symptoms), (f) patient 2 post-surgery 2 (improved symptoms).

The velocity distribution in the normal nose (Figure 3.12(a)) showed the quick development of an almost uniform velocity distribution throughout the nasal passages except the small openings above the inferior turbinates (the inferior meatus) which received little airflow. Some recirculation, and back flow was produced in the posterior nasal cavity at the nasopharynx as the air separated from the inferior turbinates.

The jet through the nasal cavity in patient 1 formed as high velocity air travelled through the nasal valve and was met with wide open space as it entered the rest of the nasal cavity. Travelling unobstructed, this jet travelled the length of the nasal cavity before impinging high on the posterior wall in the pre-surgery case (Figure 3.12(b)). The jet was still present in the post-surgery case though it was directed lower, into the centre of the cavity far from the walls (Figure 3.12(c)). The jet spread out becoming relatively diffuse by the time it reached the posterior wall, likely responsible for the reduction in stagnation pressure on the posterior wall seen in Figure 3.8. Additionally, large regions of reversed flow were present in both cases, contrasting with the near unidirectional flow of the normal nose. Following surgery, the back flow became more intense, shifting superiorly as the jet shifted inferiorly.

The redistribution of flow from the right to the left side in patient 2 was confirmed by a shift in velocity from the right to left nostril in slice two of Figures 3.12(d)-(f). Compared to the normal case, airflow penetration into the superior channels of the nasal cavity was much less effective in patient 2. Neither surgery appeared to have any affect on this. The high velocity area on the medial side of the inferior turbinates became more concentrated as the passageway there narrowed following surgery 1 (slice five). This narrowing resulted in more normal-looking passages here. Like the normal case, there were regions of low airflow near the remains of the inferior turbinate on each side. However, these regions were positioned inferiorly to their normal counterparts and included regions where, compared to the normal nose, there should have been significant airflow. Surgery 2 placed implants which filled these low velocity areas. While this may have brought more surface area in contact with the faster flowing air, it did little to affect the airflow dynamics in the nose.

Velocity fluctuations in the nasal cavity are visualised as root mean square (RMS) velocity in Figure 3.13. There was very low RMS velocity throughout the normal nose, with just a small amount at the nasopharynx as the air separated from the ends of the turbinates (Figure 3.13(a)). This behaviour supports reports in the literature of much of nasal airflow being smooth and near laminar (Doorly *et al.* (2008); Chung *et al.* (2006)).

Patient 1 showed a large deviation from the expected laminar flow behaviour (Figures 3.13(b) and (c)). Regions of high RMS velocity were seen throughout the nasal cavity in both the pre- and post-surgery geometries. This was likely due, in part, to the cavernous nature of this nasal cavity providing wide open spaces, free from the influence of nearby walls, where fluctuations could grow as they travelled downstream. The source of these disturbances were likely shear layers around the jet of air travelling through the nose. Following surgery, there was a dramatic increase in the level of RMS velocity, clearly seen around the perimeter of the air jet (Figure 3.13(c)). These fluctuations were initially promoted by back-flow into the nasal valve area seen in Figure 3.12, and were amplified by further back-flow surrounding the jet as it travelled through the centre of the cavernous nasal cavity. This increase in RMS velocity was responsible for the more diffuse jet following surgery as seen in Figure 3.12(c). Sustaining these shear layers requires energy and it is likely that this increased shear layer was responsible for the lower pressures seen throughout the nasal cavity following surgery in Figure 3.8(c).

RMS velocities were very low throughout the nasal cavity in Patient 2, similar to that seen in the normal nose (Figures 3.13(d)-(f)). There were a couple of regions of elevated RMS velocity, caused by back flow, in the inferior meatus where the inferior turbinate used to be, though these are very weak and disappeared following surgery 1. Most notably, however, was a large region of elevated RMS velocity in the nasopharynx of the pre-surgery case which was mitigated following surgery. This is near where the auditory tube connects to the nasal cavity and the mitigation of this region of RMS velocity seems to correlate with the reduction of ear related symptoms seen in patient 2. The cause of this region of high RMS velocity is not evident

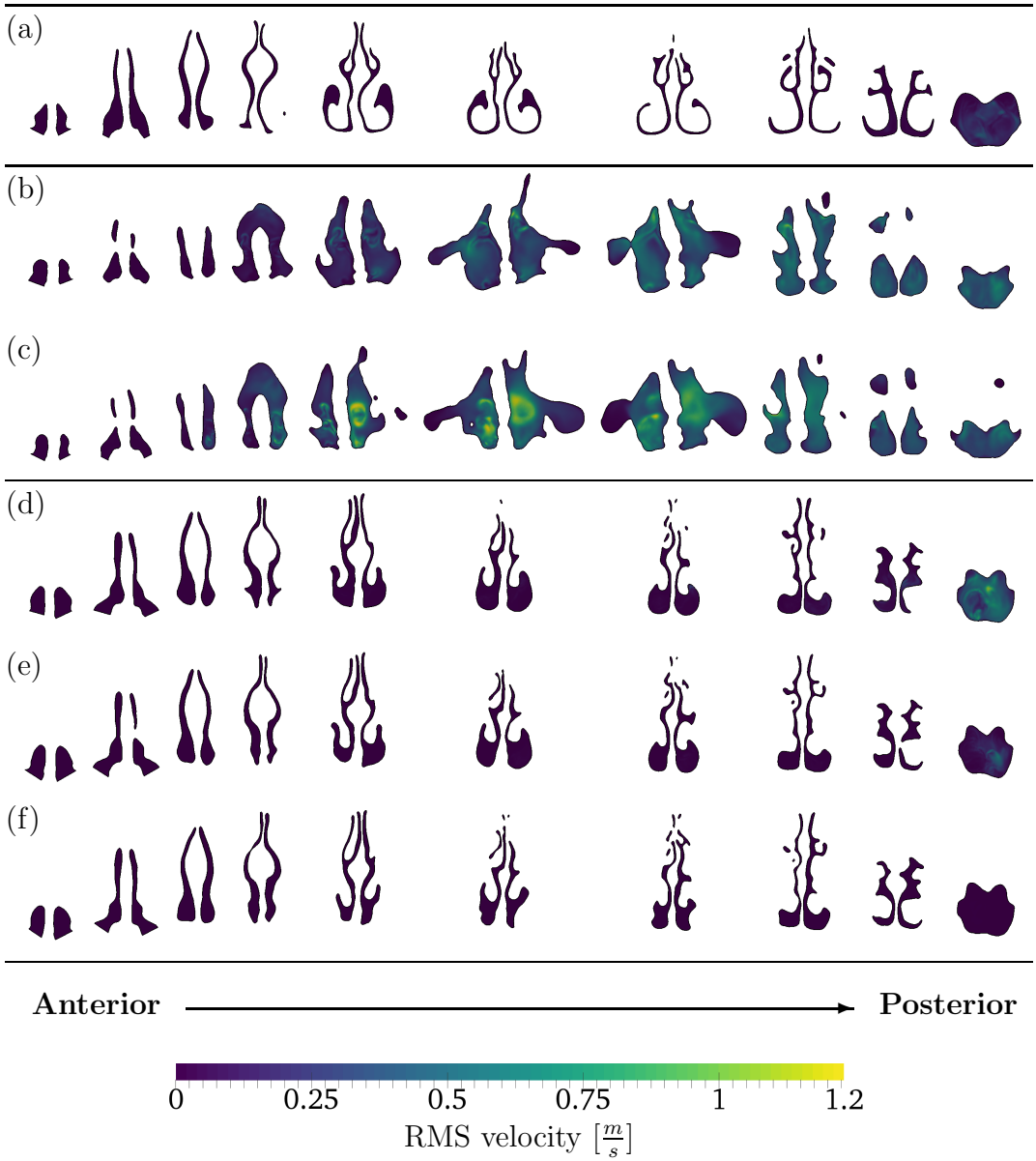

Figure 3.13: RMS velocities in each geometry. Velocities are viewed on equally spaced coronal slices through the nasal geometry. The results are time averaged. (a) normal, (b) patient 1 pre-surgery (with ENS), (c) patient 1 post-surgery (improved symptoms), (d) patient 2 pre-surgery (with ENS), (e) patient 2 post-surgery 1 (improved symptoms), (f) patient 2 post-surgery 2 (improved symptoms).

here but appears to result from the interaction between recirculating airflow impinging on the rear of the nasopharynx (Figure 3.7) and the air leaving the left side of the nasal cavity.

Temperature and water transport are analogous transport phenomena, both have similar diffusivity governing their transport in air (Table 3.1), and the boundary conditions used were relatively similar (Section 3.2.5). As a result, the temperature and water concentration distribution throughout the nasal cavities were very similar, and are shown in Figures 3.14 and 3.15 respectively.

In the normal nose, cold, dry air entered the normal nose forming concentrated cold and dry areas in the anterior nasal cavity (Figures 3.14(a) and 3.15(a)). These evened out and decreased in intensity by slice six as the air was conditioned. By slice eight, in the posterior nasal cavity, the air was almost uniformly conditioned to wall conditions apart from the small area inferior to the middle turbinate where three passages combine. At the nasopharynx the air is very near nasal wall conditions.

The cold, dry jet in patient 1's pre-surgery case transported unconditioned air deep into the nasal cavity to impinge on the posterior wall (Figures 3.14(b) and 3.15(b)). While cold, dry air was also transported deep into the nasal cavity in the post-surgery case, by the time it reached the posterior wall it had spread, near uniformly, throughout the cavity (Figures 3.14(c) and 3.15(c)). This reduced the humidification load on small regions of the nasal wall as would have been likely in the pre-surgery case. It is evident from the temperature and humidity in the nasopharynx, that in both cases patient 1 could not condition the incoming air as well as the normal nose.

In patient 2, like the normal case, as air entered the nasal cavity it formed concentrated cold, dry areas in the anterior nasal cavity, however, they took much longer to dissipate (Figures 3.14 and 3.15). Following both surgeries this seemed to improve, with the localised peaks of cold, dry air being smoothed out much quicker. It seems that the narrowing of the passages medial of the inferior turbinate (surgery 1) had a significant effect on this; the implants (surgery 2) appeared not to be of much benefit here. The

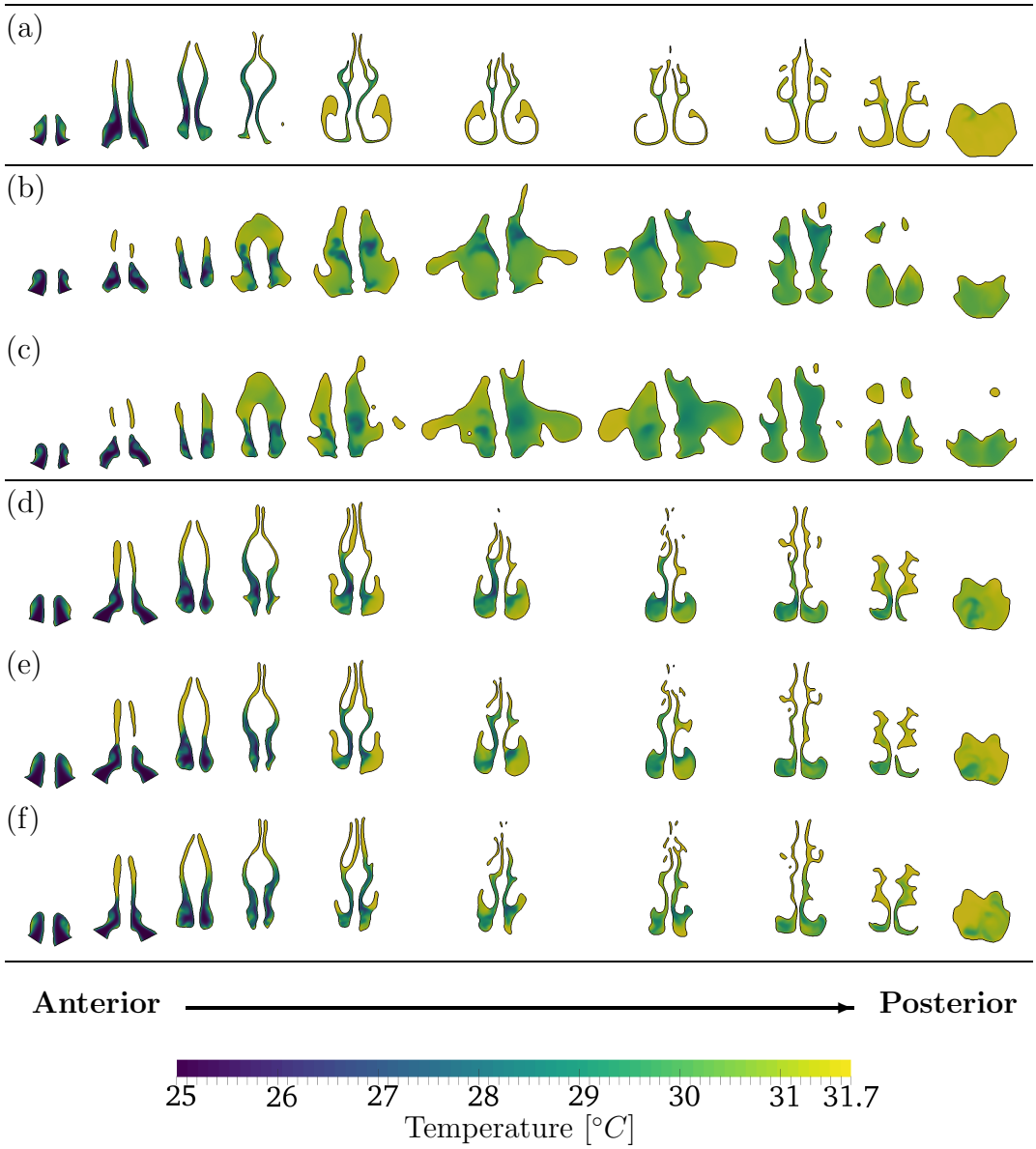

Figure 3.14: Temperature in each geometry. Velocities are viewed on equally spaced coronal slices through the nasal geometry. The results are time averaged. (a) normal, (b) patient 1 pre-surgery (with ENS), (c) patient 1 post-surgery (improved symptoms), (d) patient 2 pre-surgery (with ENS), (e) patient 2 post-surgery 1 (improved symptoms), (f) patient 2 post-surgery 2 (improved symptoms).

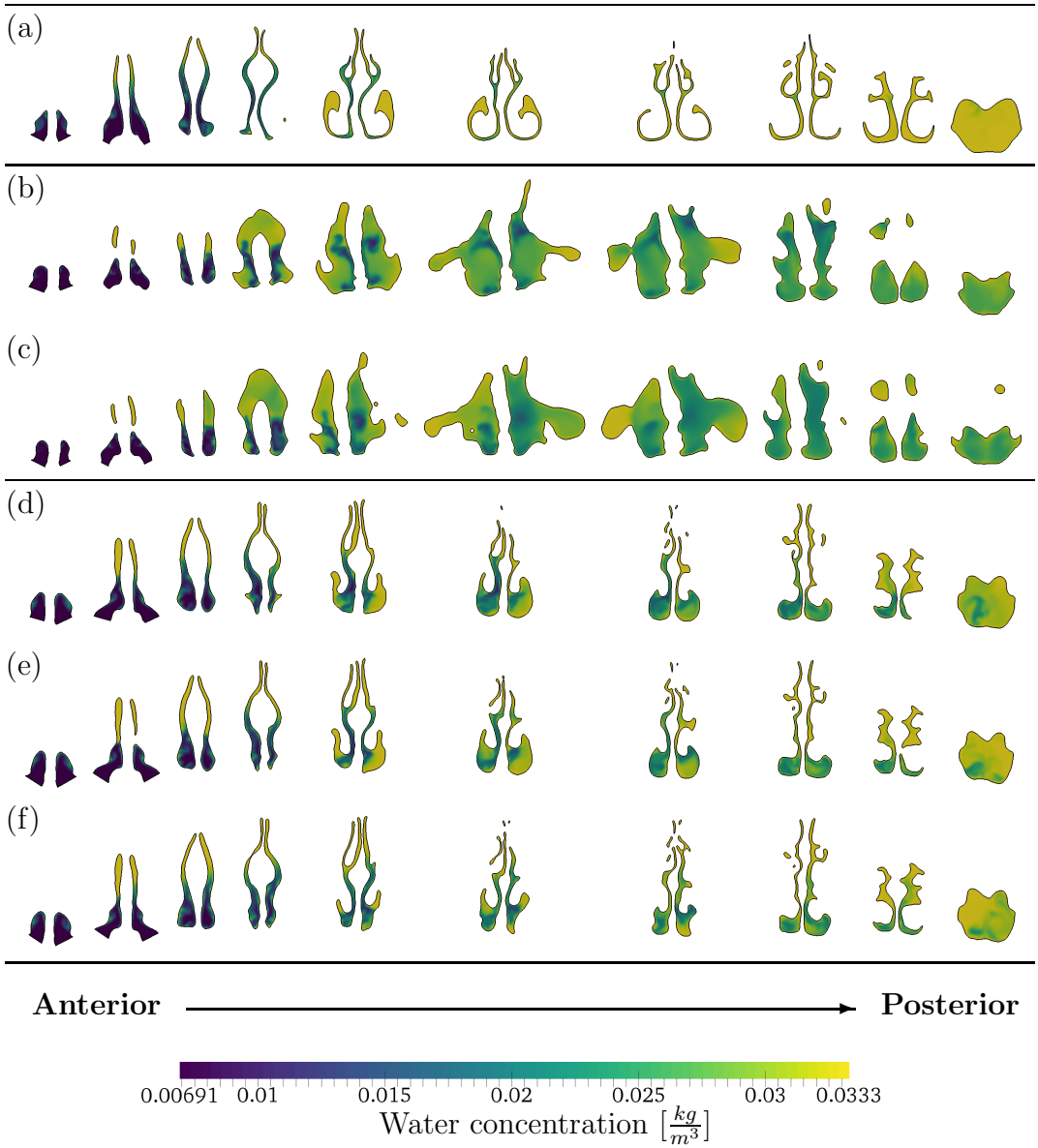

Figure 3.15: Water concentration in each geometry. Velocities are viewed on equally spaced coronal slices through the nasal geometry. The results are time averaged. (a) normal, (b) patient 1 pre-surgery (with ENS), (c) patient 1 post-surgery (improved symptoms), (d) patient 2 pre-surgery (with ENS), (e) patient 2 post-surgery 1 (improved symptoms), (f) patient 2 post-surgery 2 (improved symptoms).

temperature and water concentration at the nasopharynx lacked uniformity and were colder and dryer than the normal case in all cases. The fact that the airflow distribution swapped from left to right was clearly evident in the temperature and water concentrations here as the coldest driest part shifted from left to right. The lack of utilisation of the upper nasal cavity, and the open area below the inferior turbinate are both detrimental to this nose's air conditioning capacity.

3.3.5 Global comparison

Here we offer a quantitative comparison of each of the cases to quantify the changes occurring following each surgery and to identify metrics important to symptomatic improvement.

The nasal surface acts as a vector for force transmission, and thermal and water transport between the incoming air and the biological system beneath. The air-conditioning capacity and any sensations that might be associated with nasal breathing are in part determined by the surface area of the nasal passages. Figure 3.16 shows the total nasal cavity surface area for each of the cases simulated. The previous removal of the turbinates in both patients resulted in them having much lower nasal surface area than the normal case, with the most surgically altered nasal cavity of patient 1 being the lowest of them all.

Both surgeries which added material to the inferior nasal walls, patient 1 surgery and patient 2 surgery 2, resulted in a slight increase in surface area. Conversely, surgery 1 of patient 2 which added material to the existing turbinate structures and the surrounding tissue resulted in a slight reduction of surface area. None of the surgeries resulted in large changes in surface area, and the surface area of all post-surgery cases remain far lower than that of the normal nose.

Some commonly presented metrics are compared in Figure 3.17. Transnasal pressure loss indicates the amount of effort to drive flow through the nasal cavity at the simulated flow conditions. As seen in Figure 3.17(a),

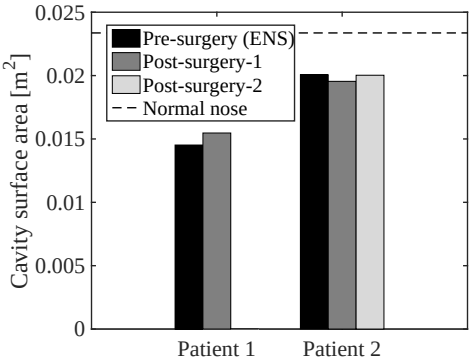

Figure 3.16: Nasal cavity surface area of each geometry.

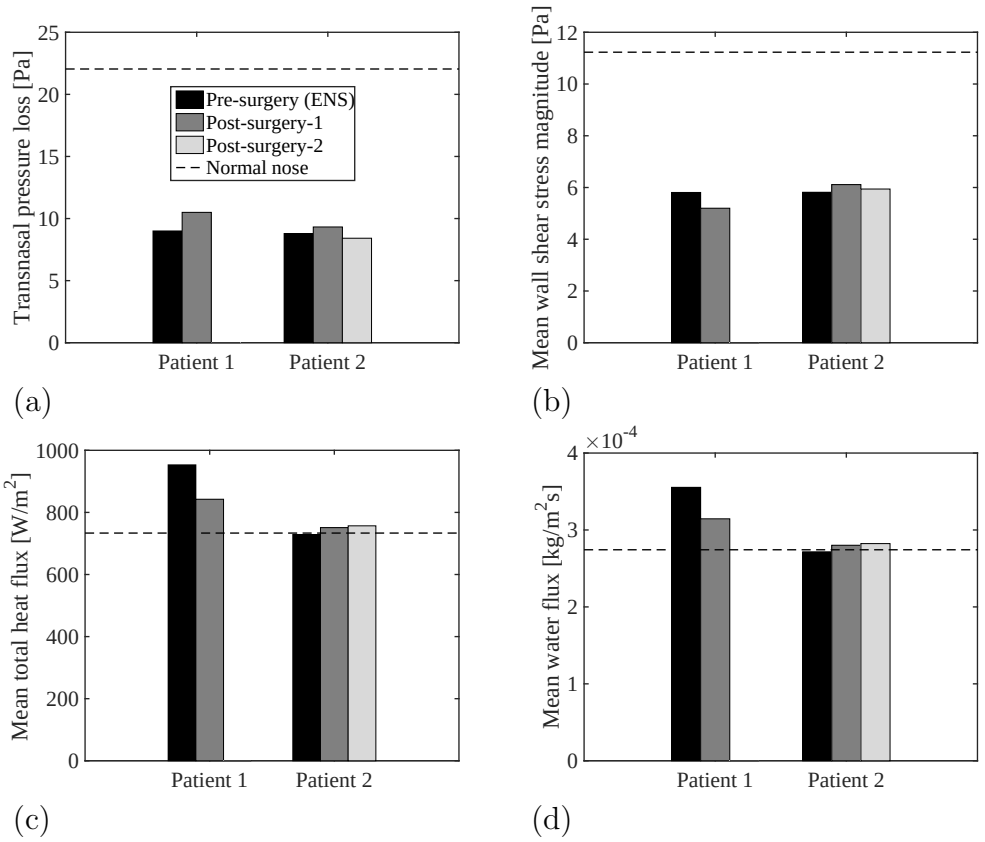

Figure 3.17: Comparison of some common metrics calculated over the entire nasal cavity. (a) transnasal pressure loss, (b) mean wall shear stress magnitude on the nasal surface, (c) mean total heat flux from the nasal surface, and (d) mean water flux from the nasal surface.

the pressure loss in all patient geometries, before and after surgical intervention, were far lower than the normal case. This highlights two things: the sensation that they cannot get enough air through their nose is completely paradoxical as they should be able to drive ample flow with little effort compared to the normal case; and pressure loss does not correlate to sensation of nasal patency. Both patients reported a significant improvement in response to the 'nose is too open' question in the ENS6Q despite minimal increases in transnasal pressure loss to levels still far below normal. These results reinforce that seen in the literature already (Chapter 2). It should be noted though that both patients did see an increase in pressure loss following their first surgeries. Interestingly, patient 2 showed a decrease in pressure loss following their second surgery. Close inspection of the coronal slices in Figure 3.12 shows that following surgery 2, the inferior turbinates, which were enlarged during surgery 1, have shrunk slightly. This resulted in an enlargement of the narrow passages medially of the turbinates and is potentially responsible for the decrease in pressure loss that was observed.

The mean wall shear stress for all cases were also well below that seen in the normal case (Figure 3.17(b)). The laminar airflow in the nasal cavity of patient 2 (Figure 3.13) meant that the mean wall shear stress followed a similar trend to the pressure loss. A slightly lower than expected mean wall shear stress was seen in the pre-surgery case however, because of pressure loss due to turbulence generated in the nasopharynx. The lower air jet seen in patient 1 following surgery interacted less with the walls producing lower mean wall shear stress than the pre-surgery case, while it is clear that the shear layer around the jet was responsible for the increase in total pressure loss.

The mean total heat flux and the mean water flux though the nasal surface may represent the average air-conditioning load required of the nasal mucosa in each geometry and are shown in Figures 3.17(c) and (d). Once again, the mean total heat flux and the mean water flux are very similar to each other. The mean total heat and water fluxes decreased following surgery for patient 1 moving closer to the value observed in the normal nose. This can be

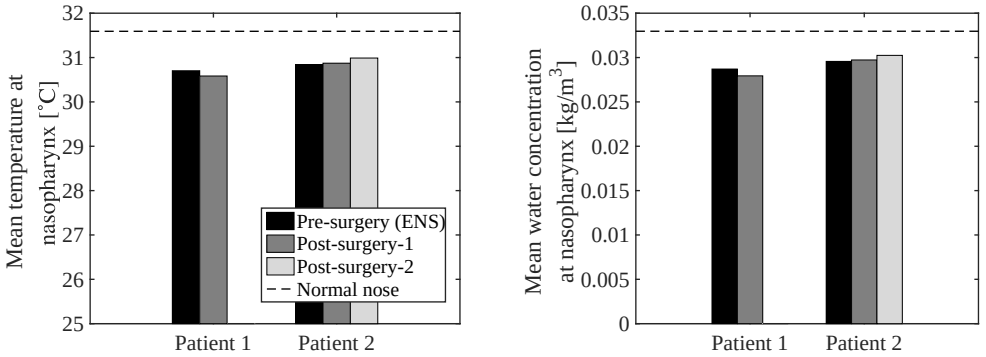

Figure 3.18: Temperature and water concentration at the exit of the nasal cavity, the nasopharynx, for each case. (a) mean temperature at the nasopharynx, (b) mean water concentration at the nasopharynx.

physically explained by the lower air jet directing more air directly towards the nasopharynx where it exits the nasal cavity with minimal interaction with the wall. In patient 2, the mean total heat and water fluxes were similar to that of the normal nose in all cases which would indicate a mean air conditioning load similar to the normal case. Small successive increases were seen following each surgery.

The air-conditioning capacity of each geometry can be compared through the air temperature and water concentration at the exit of the nasal cavity, shown in Figure 3.18. The normal nose conditioned the air much more effectively than all the patient geometries, with outlet conditions very close to the prescribed nasal wall conditions of 31.7 °C and 0.0333 $\frac{kg}{m^3}$. The air-conditioning capacity of the nasal cavity of patient 1 reduced following surgery, while that of patient 2 increased following each successive surgery. It is interesting to note that the air-conditioning capacity does not match what would be expected from looking at the mean heat at water fluxes, this can be attributed to differences in surface area between the noses.

3.3.6 Surface heat loss distribution

The antero-posterior distribution of total heat loss is presented in Figure 3.19. Here we refer to the heat lost from the mucosa to be gained by the air, this seems like a more physiologically relevant perspective than considering it as heat gained by the air.

Most of the heat loss in the normal nose (Figure 3.19(a)) occurred in the anterior half of the nasal cavity peaking just posterior to the front of the inferior turbinate. Patient 1 also showed a peak in heat loss anteriorly, though concentrated closer to the nasal valve area, slightly further forward than the normal case. However, a large amount of heat transfer occurred posteriorly in patient 1's nasal cavity, owing to the air jet impingement. This region of high heat loss was significantly reduced following surgery.

The distribution of heat loss in patient 2's pre-surgery nasal cavity was far more similar to the normal case. There was an anterior peak in heat loss which decreased posteriorly. There was still a significant amount of heat loss occurring in the posterior half of the cavity however, and a large spike at the rear of the nasopharynx resulting from air impingement. The largest modification to the heat loss distribution occurred following surgery 1, in which the anterior peak was slightly reduced, while higher levels of heat loss were observed further back; the peak in the nasopharynx was also reduced. Surgery 2 further smoothed the heat loss distribution, reducing the highest peaks and spreading them out. The peak in the nasopharynx partially returned but not to the extent of the pre-surgery case.

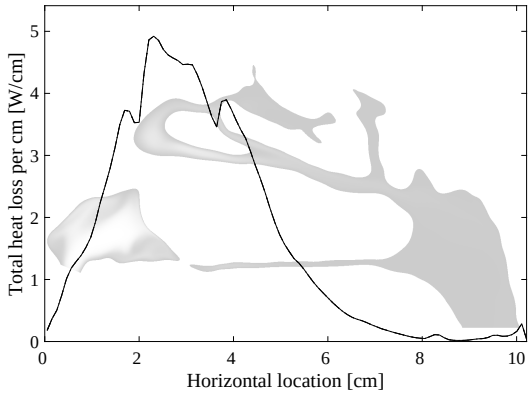

(a)

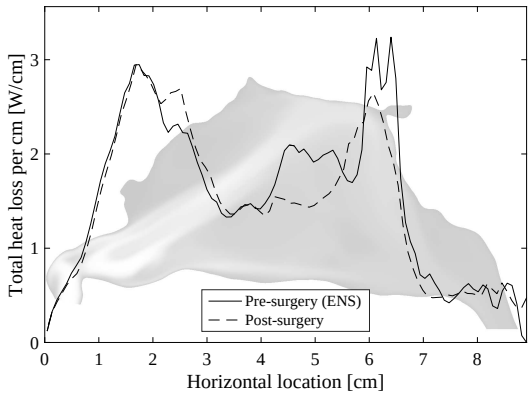

(b)

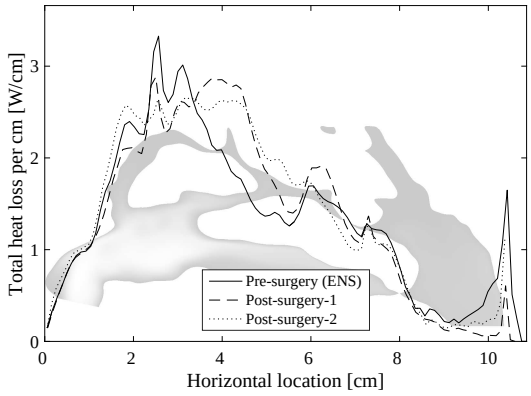

(c)

Figure 3.19: Surface heat loss as a function of the distance from the tip of the nose. A sagittal slice through the nasal cavity is shown for reference. (a) normal nose, (b) patient 1, (c) patient 2.

3.4 Discussion

3.4.1 The paradox

It is clear that ENS has a huge effect on patient quality of life. Both ENS patients here responded with high levels of dissatisfaction on most of the quality of life related SNOT-22 questions (Figure 3.5). Surgery, for both patients, resulted in improvements for all of these metrics, quantitatively justifying surgery as an effective treatment path for ENS patients.

A number of ENS specific symptoms, as identified by the ENS6Q questionnaire, were important to both patients studied here, and many of these symptoms improved following surgery (Figure 3.6). One of the difficulties in studding ENS, as evident by this result, is that ENS cannot be distilled down to one objective symptom for study, it presents as a combination of complex subjective symptoms. Identifying physical reasons for this ensemble of symptoms is difficult.

Further, symptoms can appear paradoxical, making them difficult to interpret. The essence of the key term in ENS, 'paradoxical nasal obstruction', as presented by these patients is having a cavernous nasal cavity while not being unable to 'sense' airflow, and feeling a sensation of suffocation. Perhaps more astounding is the fact that, consistent with their extremely low transnasal pressure losses (Figure 3.17), both patients initially identify a sensation of the nose being too open, however, following surgery, with minimal modification to the pressure loss, this sensation all but vanished.

Both patients reported a significant improvement in most of the major symptoms of ENS as identified in the ENS6Q, and in this regard the patients were similar. One would like to elucidate the reason for these improvements, and subsequently, the cause of the symptoms in the first place.

3.4.2 Patient specific outcomes

Apart from the commonly shared ENS symptoms seen in each patient, there were a couple of symptom combinations specific to these patients which we will address here.

Patient 1 described high levels of nasal obstruction, yet indicated a sensation of the nose being too open, impaired airflow sensation, and extremely low transnasal pressure loss (Figures 3.5, 3.6, and 3.17). On the surface, it would seem here that the nose feeling too open was justified by the low pressure loss, though the sensation of nasal obstruction does not agree. One possible explanation for this may be that the sensation of nasal obstruction in patient 1 was driven by the sinuses rather that the nasal cavity. This patient presented with a persistent frontal sinus pressure and pain, and following sinus surgeries after their SIS graft reconstruction (not simulated here), their sensation of nasal obstruction vanished. Neither this high response to the 'nasal obstruction' question in SNOT-22 or frontal headaches were observed in patient 2.

Both patients reported some form of ear discomfort in the pre-surgery case, being ear fullness, dizziness, or ear pain (Figure 3.5). Patient 2 indicated that these symptoms were largely resolved following surgery, however they persisted in patient 1. The middle ear connects to the nasopharynx through the Eustachian tube (auditory tube) in order to regulate pressure. The auditory tube opens, to let air through, during swallowing or yawning, but also if the pressure in the nasopharynx is sufficiently higher or lower than that of the middle ear (Proctor & Andersen (1982)). One possible explanation for these ear related symptoms may be the high levels of turbulence in the nasopharynx and the associated pressure fluctuations, as evidenced by the RMS velocities shown in Figure 3.13. In the pre-surgery case both patients had elevated levels of turbulence in the nasopharynx compared to the normal case. Following surgery, these levels persisted in patient 1, while they decreased to normal levels in patient 2. These observations were consistent with the reported progression of these symptoms.

Some level of dryness was reported by both patients. The efficacy of the nasal air conditioning decreased following surgery for patient 1, and increased following surgery for patient 2 (Figure 3.18), being consistent with the patient responses to 'dryness' in the ENS6Q (Figure 3.6). A dry throat elicits a recognisable sensation and cooler, dryer air entering the pharynx would dry

it out over time. Could this result in the sensation of dryness reported here?

3.4.3 The air conditioning capacity of the ENS nose

In agreement with previous studies (Garcia *et al.* (2007)) the air conditioning capacity of the pre- and post-surgery ENS noses were significantly poorer than the normal case (Figure 3.18).

Comparing the cases, it appears that the presence of narrow passages and the effective use of both the upper and lower passages are features unique to the normal nose (Figures 3.14 and 3.15). Patient 1 lacks a significant amount of turbinate tissue making direct comparison with the normal case difficult. Patient 2 is closer to normal and less conditioning appears to occur in the upper passages of patient 2 than it does in the normal case. The result of this is that instead of utilising the narrow superior passageways, air-conditioning is confined to the middle and inferior parts of the cavity where tissue has been removed, and the passageways are wide and open. The implants, being positioned in an area where little airflow occurs anyway, do little to modify the airflow dynamics in this respect. In addition, the upper passageways around the middle turbinate in patient 2, appear to be more physically obstructed compared to the normal airway.

Narrowing the nasal passages and spreading airflow throughout the height of the nasal cavity are likely important to improving air conditioning capacity in these patients. However, while proper air conditioning capacity helps protect the delicate structures in the lung, it is likely not the root cause of the pertinent ENS symptoms. The majority of ENS symptoms improved following surgery, while the change in air conditioning capacity between patients was not consistent and still remained far lower than the normal case.

3.4.4 Response to common hypotheses

As covered earlier in this thesis (Section 2) there have been many hypotheses about the pathophysiology and treatment of ENS. We addressed many of these using evidence from relevant literature. Here we present evidence from the present work to support those claims and others.

Surface area

Part of the motivation behind surgical implants to treat ENS has typically been to increase the nasal surface area to allow more interaction with the incoming airflow (Sozansky & Houser (2015); Garcia *et al.* (2007)). While this may be a sound objective, surgery does not always result in an increase in nasal surface area, and when it does, the resulting surface area may still be significantly lower than normal, as seen in Figure (3.16). Despite this, surgery can still result in positive outcomes for the patient as evidenced by this study.

Nasal resistance

Nasal resistance is directly proportional to transnasal pressure loss,

$$\mathrm{R}_n = \frac{\Delta P}{Q}, \tag{3.11}$$

Where ΔP is the transnasal pressure loss and Q is flow rate. Typically nasal resistance is measured using a much larger pressure drop than was obtained here. Because of this, CFD derived nasal resistance is not directly comparable to clinical values (Garcia *et al.* (2007)). So, here we use our transnasal pressure loss as a proxy for nasal resistances in these patients.

Speculation about the role that nasal resistance has in causing the symptoms associated with ENS is widespread in the literature (Section 2.4). Both patients studied here showed a slight increase in transnasal pressure loss following their first surgery, and they both showed widespread improvement in ENS related symptoms. However, following their second surgery, patient 2's transnasal pressure loss decreased to a value even lower than the pre-surgery case. Testimony following this surgery indicated that this patient saw further improvement in their symptoms despite the low transnasal pressure loss. In addition, the variations in transnasal pressure losses seen in these patients were relatively small, and they were both still far lower than the normal case following surgery. It seems therefore unlikely that transnasal pressure loss is responsible for the symptoms seen in ENS patients.

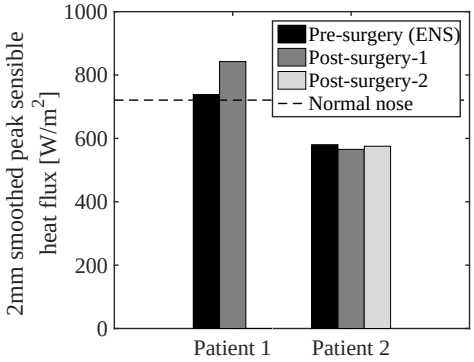

Figure 3.20: Peak sensible heat flux posterior of the vestibule in each geometry after 2 mm spatial smoothing.

Heat flux

Many suggest that the lack of airflow sensation in ENS is related to decreased activation of TRPM8 cool thermoreceptors caused by a lack of mucosal cooling (Section 2.4). And while this is a natural conclusion given the evidence linking thermoreceptor activation and a sensation of nasal patency (Zhao *et al.* (2011); Baraniuk (2011)), the literature does not support this conclusion as the nasal cavum is thought to play a minimal role in this sensation (Clarke *et al.* (1992)). The present results support this interpretation of the literature. The mean total heat flux in the nasal cavity (Figure 3.17) decreased following surgery for patient 1, and increased following both surgeries for patient 2, yet both reported an improvement in the 'absence of airflow sensation' metric of the ENS6Q. Further, Patient 1 had a significantly higher mean total heat flux than the normal case both pre- and post-surgery, while patient 2 was almost identical to the normal case pre-surgery.

Further, recent results suggest that nasal patency may be sensed through localized peak nasal mucosal cooling (Zhao *et al.* (2014)). The peak sensible heat flux posterior of the vestibule after 2 mm spatial smoothing, the relevant metric found by Zhao *et al.*, for each case is presented in Figure 3.20. Like the mean total heat flux, these results show no consistency between patients and their relation to the normal case is unusual given their symptoms.

Interestingly, however, both patients showed a local increase in total heat loss anteriorly in the nasal cavity (Figure 3.19). The change in patient 1 was smaller than that seen in patient 2, and occurred more anteriorly. The implications of this are not yet known.

It is unlikely that the lack of airflow sensation felt by these patients was due to a lack of thermoreceptor activation by reduced mucosal heat flux as has often been speculated. Perhaps, however, the mechanism by which nasal patency is felt through the thermoreceptors is more complex than we expect, in which case this conclusion can be re-evaluated.

3.4.5 New hypotheses

Wall shear stress

Some have used terms such as 'less sensate airflow' and 'reduced air-mucosal contact' to describe the loss in sensation described by ENS patients (Section 2.4). If heat flux is not responsible, it may be pertinent to question the role of wall shear stress.

There is evidence that mechanoreceptors, sensors that respond to mechanical stimulation, are present throughout the nasal mucosa (Clarke & Jones (1992, 1994); Wrobel *et al.* (2006)). However, the present results show contradictory trends in mean wall shear stress between patients following surgery (Figure 3.17).

Li *et al.* (Li *et al.* (2017)) simulated the nasal cavities of patients who developed ENS following inferior turbinate reduction. They noted a reduction in airflow and a reduction in mean wall shear stress in the inferior portion of the nasal cavity in the ENS cases. Further, as noted in section 2.5, past simulations of ENS patients have described more airflow in the superior portion of the nasal cavity, while inferior turbinate reduction patients without ENS show more airflow in the inferior portion of the nasal cavity. Figure 3.21 shows the mean wall shear stress with vertical position in each of the simulated geometries. In support of previous observations, the present data clearly shows a local increase in mean wall shear stress in the inferior portion

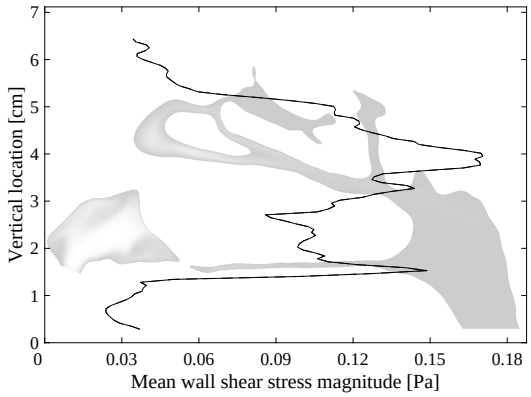

(a)

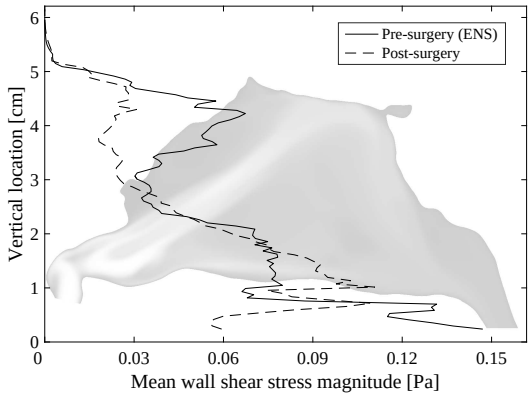

(b)

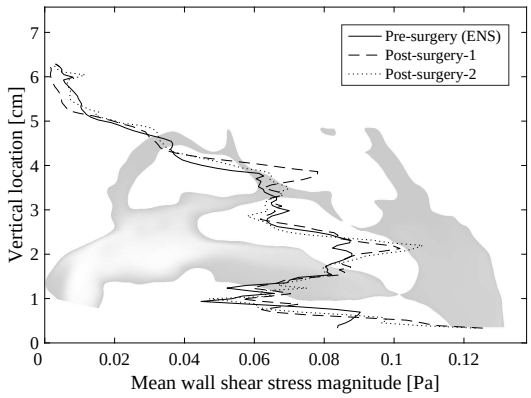

(c)

Figure 3.21: Mean wall shear stress with height in each nasal geometry. (a) normal nose, (b) patient 1, (c) patient 2.

of the nasal cavity following surgery. In patient 1, the location of increased mean wall shear stress corresponds to the nasal floor and the inferior nasal valve. In patient 2, the increase occurred on the inferior wall of the inferior turbinate and the inferior septal wall. These changes were likely due to the inferior turbinate in fracture in patient 2; and the lower mean airflow in conjunction with a higher nasal floor in patient 1. The mean wall shear stress in the superior half of the nasal cavity in the normal case is significantly higher than that seen in all patient cases. This region may not be as important to ENS as the inferior half of the nasal cavity.

The mean total heat flux with vertical position was also plotted (Figure 3.22). It is interesting to note that mean heat flux does not show the same trends as the wall shear stress as convincingly. And the mean heat flux in both patients inferiorly was much higher than that seen in the normal case.

Mucosal health

Patients with ENS often report a variety of symptoms atop of the well known sensations of paradoxical nasal obstructions (Section 2.1). Both patients studied here reported symptoms of nasal crusting and burning which both improved following surgery (Figure 3.6). The presence of crusting might suggest poor mucociliary clearance or drying out of the mucosa, especially since many patients report nasal dryness too. One may ask if dryness could also play a role in the sensations of nasal obstruction. This would provide a unified cause for all the symptoms associated with ENS.

The mucus layer covering the nasal mucosa acts the vector through which not only heat and water are transported between the air and the cells beneath, but is also the medium through which forces must be transmitted. It is possible that changes to the state of the mucosa and overlying mucus layer would change how airflow would be 'felt' in the nasal cavity.

The 'honeymoon' period of minimal symptoms following surgery, as described by patient 2 and likely related to the peak improvement in sleep related SNOT-22 seen at 3 months (Figure 3.5), occurred at the same time as a peak in the patient's reported 'need to blow nose' and 'thick nasal dis-

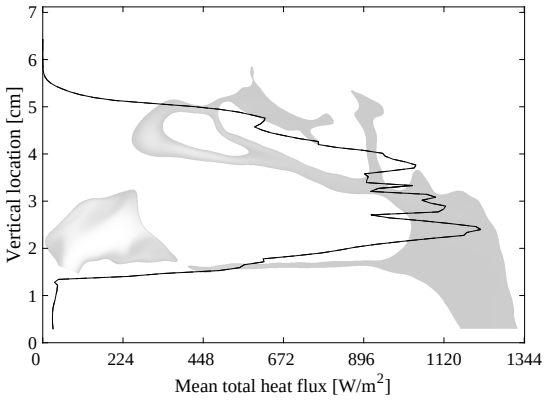

(a)

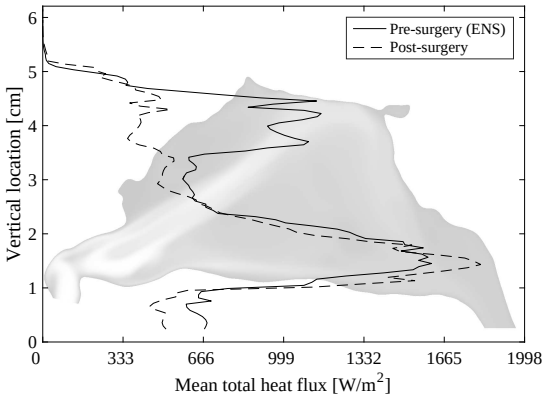

(b)

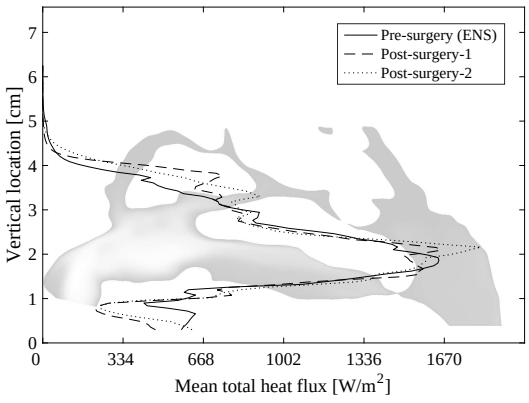

(c)

Figure 3.22: Mean total heat flux with height in each nasal geometry. (a) normal nose, (b) patient 1, (c) patient 2.

charge' symptoms. It has also been reported in the literature that patients suffering from ENS have seen an improvement in symptoms during infection (Modrzyński (2011)); and medical treatment typically involving nasal moisturising brings patients temporary relief from symptoms. The state of the nasal mucosa, being highly affected by water fluxes, appears to be related to ENS symptoms.

Surprisingly, the results presented here show inconsistent trends between patients regarding total heat flux, and hence water flux, in the nasal cavity. Posterior heat loss decreased in patient 1 following surgery, while anteriorly it increased slightly. Patient 2 did not show a significant change in the posterior nasal cavity, and increased heat loss occurred in the anterior-middle of the cavity (Figure 3.19). Vertically, the mean heat flux decreased in some locations while it increased in others, inconsistently between cases (Figure 3.22). The mean heat and water fluxes decreased following surgery in patient 1, while they increased in patient 2 (Figure 3.17).

The normal case illustrated normal variation in water flux across the nasal surface (Figure 3.10). Different areas of the nasal mucosa are used to different amounts of water flux, and therefore it is likely that the air conditioning capacity of the mucosa varies similarly with location. The amount of water flux required to cause distress to the nasal mucosa is likely to vary throughout the nasal cavity, and without knowing details of this distribution drawing conclusions about the state of the mucosa from these simulations would be erroneous.

3.4.6 Final thoughts

To remain consistent with the conclusion that the nasal mucosa plays no significant role in the normal sensation of airflow (Clarke *et al.* (1992)) the responsible mechanism behind ENS must feasibly be able to produce a unique, not normally felt, sensation which would manifest as feelings associated with ENS. It is possible to postulate mechanisms by which both wall shear stress, and mucosal health may comply with this requirement. Abnormal water flux and drying of the mucosa could potentially produce an unusual sensation

simply by disrupting the mucus layer's nominal state, resulting in damage to the underlying mucosa, and modifying force and heat flux transmission to the tissue below. One possible mechanism by which wall shear stress may produce an unusual sensation could be spatial discrepancies from the normal distribution of wall shear stress. For example, given that there was sufficient wall shear stress in the nasal valve area, if there was insufficient wall shear stress in the inferior nasal cavity this may produce abnormal feelings.

The cotton test proves that near-instant relief of symptoms can be produced by changing the geometry of the nasal cavity alone. Within 10 minutes, improvement has been recorded in all ENS6Q questions, including 'dryness' and 'nasal crusting' (Thamboo *et al.* (2017)). It is not unreasonable that both wall shear stress and mucosal health could satisfy this requirement too. In the case of wall shear stress, instant relief in sensation may be obtained simply by favourably redistributing airflow to a more nominal state, while disruptions to the mucus layer likely occur also to cause nasal crusting. For water flux, relief from all symptoms may be realised either by covering the damaged mucus layer with the cotton, or by re-directing airflow so that it no-longer interacts with the area of the depleted mucus layer.

It has been shown in the literature that ENS patients have significantly lower trigeminal sensitivity (tested via inhalation of menthol) than normal patients (Li *et al.* (2017); Konstantinidis *et al.* (2017)). Abnormal wall shear stress patterns would imply a re-organisation of air-mucosal interactions which may reduce interactions in locations with high menthol sensitivity. Perhaps the presence of a dry mucosa may modify the interaction between menthol and the mucosa resulting in poor detection thresholds for menthol.

Finally, we cannot ignore the fact that ENS symptoms may take months to years to appear (Chhabra & Houser (2009)). Is it possible that slow modification of the nasal cavity over time due to healing or adaptation of the nasal lining could produce delayed, abnormal wall shear stress distributions? Or, is it more likely that abnormal water fluxes slowly damage the mucosa and mucus layer? Are they also compatible with the fact that symptoms can

also manifest soon after turbinate surgery (Houser (2007))?

Despite the evidence for the distribution of wall shear stress being implicated in the subjective symptom profile seen in ENS, we should not rule out the possibility of the interaction between water flux and the mucus layer. In contrast to wall shear stress, water flux could alone be responsible for the abnormal breathing sensations associated with ENS as well as the other symptoms such as burning, crusting, and dryness that commonly accompany ENS. There are many questions as to how these proposed mechanisms fit within the constraints identified by the current literature, and research into this topic will likely yield a fuller understanding of ENS.

3.4.7 Limitations

Data

As seen here, it is likely that with current knowledge, a patient will require multiple surgeries before they are sufficiently relieved from their ENS symptoms, recovery from this condition appears to lie on a spectrum. Following surgery, these patients still observed residual symptoms of ENS, though to a much lower extent than they did previously. This means that the flow features that are responsible for ENS were likely still present to some extent in both pre- and post-surgery simulations, making a black and white comparison unlikely.

To maximise the output of a study like this, there must be careful documentation of both the geometric and symptomatic state of each patient throughout the treatment timeline. The use of standardized questionnaires like the SNOT-22 and ENS6Q make symptoms easier to track, and CT scans are sufficient to record geometry. However, keeping these kinds of records requires foresight from clinicians who deal with ENS patients, so that the results can be studied later. Here, we were not able to get hold of CT scans from patient 1 following their further surgeries, and we were unable to retrieve SNOT-22 and ENS6Q results from patient 2 following their second surgery, both of which may have helped shed more light on the development

of ENS.

Every patient is unique in their geometry, flow features, and symptoms. Comparison between two patients to isolate the causes of specific symptoms is difficult, and not a perfect procedure.

Geometry

Generating a three dimensional model of a real nasal cavity is an uncertain procedure for many reasons. The resolution of the CT scan, the segmentation procedure, geometrical smoothing, and variations of the patients nasal state over time all contribute.

Computerized tomography scans provide a radiation dose to the patients receiving them so their frequency and resolution are often limited to what is sufficient for diagnosis and treatment. As a result, CT scans are rarely of the quality desired for an accurate three dimensional model to be produced. Smoothing of the CT generated model is therefore required to remove artefacts resulting from the segmentation process. In addition, there will always be some uncertainty about the location of the interface between air and tissue when trying to resolve a discontinuous interface with finite resolution. So the segmentation procedure may not necessarily result in the exact nasal geometry of the patient that you are modelling. One result of this is that it is difficult to know if the small scale roughness of the geometry is faithfully represented in each model. The calculation of accurate wall shear stresses could be highly affected by this kind of error in the geometry. In this study, a repeatable segmentation and smoothing procedure was used for each geometry to make the models comparable.

Natural variations in nasal cavity geometry over time adds additional uncertainty to comparisons such as the one presented here. In both patients variations in the superior and the anterior nasal cavity were observed, even though both locations were untouched by surgery. The possibility of nasal cycling, where the side of the nasal cavity with the most airflow resistance periodically cycles between the left and right cavities, also provides modification to flow features that may not be due to surgery alone. In patient 2,

higher velocities were observed in the right cavity of the pre-surgery case, by the post-surgery-2 case higher velocities were observed in the left nasal cavity instead. It is difficult to determine whether this was due to surgery or natural cycling.

Some parts of the nose are flexible, such as the nostrils and the soft palate, which likely change geometry as we breathe. It is difficult to know how this would affect the flow features inside the nose. Similarly, the effect of the vibrissae (nasal hairs) on the flow features in the nasal cavity are unknown.

Flow assumptions

The assumption of steady flow removes the inertial effects of breathing and only allows the analysis of one instant during the respiratory cycle.

Inflow turbulence was neglected here, its importance to the development of flow features in the nasal cavity is unknown.

Sample size

Many factors including data availability and computational expense meant that only a very small sample of ENS and normal nasal cavities was possible for this investigation. This should be kept in mind when interpreting the conclusions resulting from this work.

3.5 Conclusions

The study of ENS requires foresight and rigorous documentation of the geometrical and symptomatic state of patients throughout the treatment timeline to build up data for rigorous study.

This study presented simulations of the airflow through multiple nasal geometries, one normal, two with ENS, and three post-surgical geometries with improved ENS symptoms. The results did not support the hypotheses that the air conditioning capacity, nasal surface area, nasal pressure loss, and lack of thermoreceptor activation by heat flux play a significant role in the pathophysiology of ENS.

There was a correlation between the ear related discomfort in these patients with elevated turbulence levels in the nasopharynx, near the auditory tubes.

Dryness, as identified in the ENS6Q, may be related to a sensation of dryness in the pharynx, as it correlated with poor air-conditioning of air by the ENS nose. Narrowing of the nasal passages and spreading airflow throughout the height of the nasal cavity could improve air conditioning capacity in these patients.

In agreement with the literature, a deficit of mean wall shear stress in the inferior nasal cavity appears to correlate with the presence of ENS related symptoms. Mean heat flux distribution and superior wall shear stress likely have little affect on ENS symptoms.

Mucosal dryness and the state of the mucus layer could offer a universal explanation for many ENS symptoms. More detailed models of the air-mucus interaction, and information about local air conditioning capacity throughout the nasal mucosa is required for the study of this hypothesis through CFD.

Both wall shear stress effects, and mucosal dryness could feasibly fit within the framework of the current literature. While there is presently evidence connecting wall shear stress distribution to ENS symptoms, mucosal dryness should be investigated before discarding it as a possible cause. Further research into how each of these mechanisms may satisfy the constraints set out by the current literature will be necessary to understand their role in ENS.

Chapter 4

Exploration of new boundary conditions

4.1 Background

The health of the nasal mucosa and the state of the overlying mucus layer are likely important to nasal symptoms involving malfunction of the nose's mucociliary clearance function and may influence nasal heat and force sensation. In empty nose syndrome specifically, patients sometimes report nasal crusting in addition to sensation related symptoms (Houser (2007)). The nasal mucus layer is 95% water and the thickness of the layer is important to mucociliary clearance (Mygind & Dahl (1998)). Abnormally high water fluxes can reduce the thickness of the mucus layer and cause mucociliary transport to cease. The mucus layer acts as the medium through which forces are transmitted from the air to neurosensory receptors in the nasal mucosa. If changes to the state of the mucus layer can be linked to the sensation related symptoms seen in ENS it could provide a unified cause for all ENS symptoms. Research about how nasal airflow interacts with the nasal mucus layer could aid our understanding of mucosal function and sensation.

In the literature, Modrzynki (Modrzyński (2011)) reported that some ENS patients feel relief during infection. ENS patients also feel temporary relief following nasal moisturising (Jang *et al.* (2011); Leong (2015); Houser

(2007)). One could draw a tentitive link between variations to the state of the nasal mucosa and ENS symptoms. Thamboo *et al.* (Thamboo *et al.* (2017)) reported improvements in all ENS symptoms, including crusting, following insertion of a wad of cotton into patients' nasal cavities. Thamboo's result links geometrical changes in the nasal cavity with changes to the mucus layer in ENS symptoms.

Computational fluid dynamics is likely the only tool able to investigate the interaction between airflow and the nasal mucosa in realistic nasal geometries. Use of CFD to study such a phenomenon would first require physiologically accurate boundary conditions which are not yet available. Elad *et al.* (Elad *et al.* (2008)) also noted that accurate handling of the air-tissue-interface was lacking in current CFD models. The most obvious deficiency in the current CFD analyses of ENS, and the nasal cavity in general, is the assumption of a constant wall surface temperature, as assumed by many previous investigations (Garcia *et al.* (2007); Zhao *et al.* (2014); Naftali *et al.* (1998); Na *et al.* (2012); Hariri *et al.* (2015)). It is clear from the results of Lindemann *et al.* that the nasal mucosal temperature changes with both location and airflow conditions. Kim *et al.* (Kim *et al.* (2017)) treated the mucosal surface as a heat conducting layer of water to yield a variable surface temperature. Unlimited mucus secretion was assumed and the water concentration on the surface was set to 100% relative humidity with the vapour pressure defined by the local surface temperature. They compared results using the variable surface temperature with that using the constant surface temperature and found that the constant surface temperature case underestimated heat and water fluxes by 10-40%. Similarly, Kumahata *et al.* (Kumahata *et al.* (2010)) simulated a nasal cavity with a conduction layer wall model for both temperature and water transport. By transporting the water through the wall layer they allowed for variable relative humidity on the surface also. They noted significant changes in temperature and water concentration in narrow parts and near the front of the nasal cavity when compared to the constant temperature and water concentration case.

The effect that latent heat has on both the air and the mucosa also needs

to be properly accounted for. The simulations presented in Chapter 3, along with many others, implicitly assume that the latent heat required by water evaporating from the surface was supplied solely by the wall and did not affect the wall temperature. The justification for this assumption comes from the fact that the thermal conductivity of the nasal wall (assumed to be similar to that of water) is about 20 times that of the air at nasal wall temperature and the nasal mucosal is highly vascularised allowing efficient heat transfer. Hanida *et al.* (Hanida *et al.* (2013)) extended Kumahata *et al.*'s conduction wall model (Kumahata *et al.* (2010)) and included the effect of latent heat on the wall surface temperature. They found that the inclusion of that latent heat effect had a significant impact on the temperature and humidity in the nasal cavity.

Tsu *et al.* (Tsu *et al.* (1988)) proposed a model to vary the thickness of the mucus layer as liquid evaporated and condensed on it, though this was only applied to a one-dimensional model of airway air-conditioning. Boundary conditions for nasal airflow CFD still cannot predict drying out of the mucosal surface.

4.2 Objectives

The aim of this part of the thesis is to explore new boundary conditions for nasal CFD on a simplified geometry and evaluate their utility to future study of empty nose syndrome.

We implemented a variable wall temperature boundary condition and a simple model to account for mucosal drying. The effect of each of these boundary conditions on air conditioning capacity, wall fluxes, and wall temperatures will be assessed. The ability of the drying model to capture mucosal drying will be discussed along with the relevance of these boundary conditions to the study of ENS.

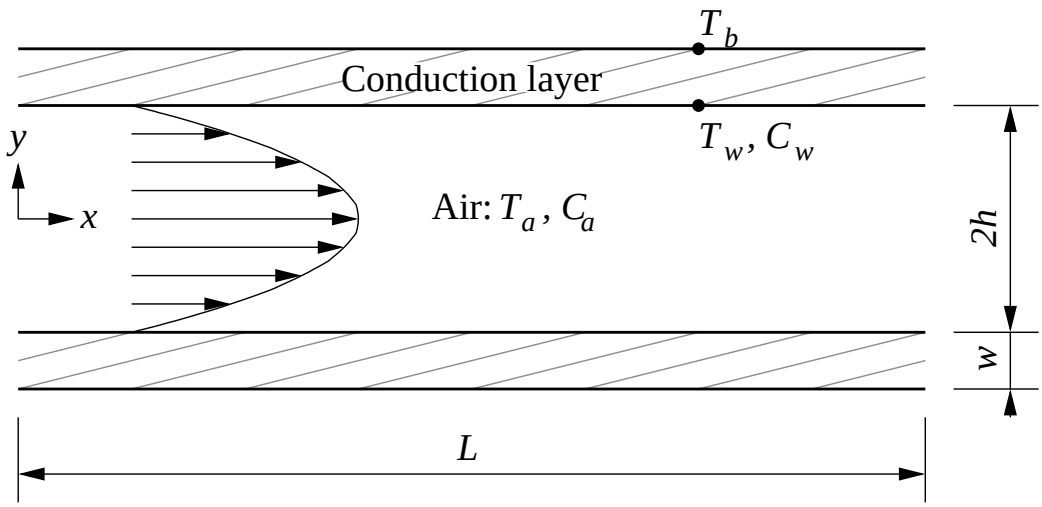

Figure 4.1: Schematic of the channel geometry. L is the channel length; h is the channel half height; w is the conduction layer thickness; T_a, T_w, and T_b are the air, wall, and body temperatures respectively; C_a and C_w are the air and wall water concentrations respectively.

4.3 Methodology

4.3.1 Geometry and mesh

Poiseuille flow was chosen as the test bed for the new boundary conditions. It is a well know flow and its simple geometry make it easy to implement. The channel is also a reasonable approximation to the narrow passages in the nasal cavity. A schematic of the geometry is shown in Figure 4.1.

A solid conduction layer is included on the boundaries of the channel to facilitate the variable temperature boundary condition. A constant body temperature, T_b, can be specified on the outer edge of the thermally conductive conduction layer allowing the wall temperature, T_w, to vary depending on the airflow in the channel. This is similar to approaches taken by other researchers to implement a variable temperature boundary condition (Kim *et al.* (2017); Kumahata *et al.* (2010)).

The dimensions used in the present simulations are given in Table 4.1. The length of the channel, L, was chosen to match the mean path length in

Dimension	Value
L	0.125 m
h	6.45×10^{-4} m
w	0.00364 m

Table 4.1: Channel dimensions.

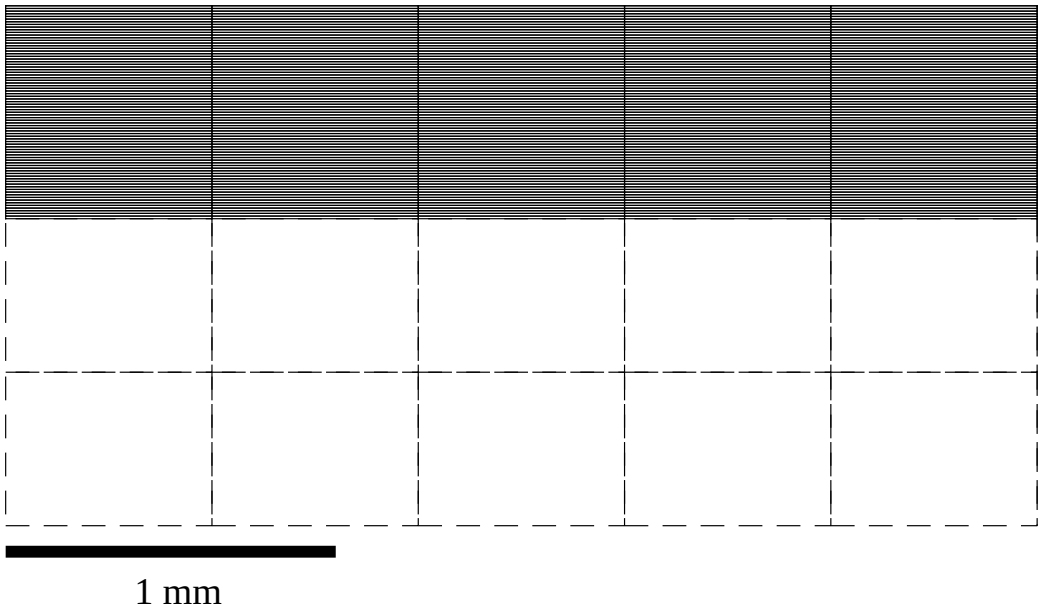

Figure 4.2: A short length of the lower half of the channel mesh. The conduction layer mesh is drawn in dashed lines, the fluid mesh is solid.

the normal nose simulation presented in Chapter 3. The channel half height, h, was chosen such that the pressure drop across the channel was equivalent to the pressure loss across the normal nose (Chapter 3). The conduction layer thickness, w, was calculated from physiological properties (Section 4.3.3).

A structured rectangular mesh was used for the numerical solution and a section of it is shown in Figure 4.2. There were 200 cells in the streamwise direction, 160 cells across the height of the fluid domain, and 2 cells across the conduction layer; for a total of 32800 cells.

4.3.2 Numerical methods

Fluid

The Navier-Stokes equations were not solved numerically. Instead the problem was simplified by making a number of assumptions about the flow:

- The flow is steady
- The velocity profile is fully developed throughout the entire channel
- Laminar flow, justified by the low Reynolds number of 278
- Air can be treated as an incompressible fluid, justified by the low Mach number of $<5\times10^{-3}$
- Buoyancy effects can be ignored, justified by the low Richardson number of 1.2×10^{-4}

The Reynolds, Mach, and Richardson numbers are defined respectively as

$$\mathrm{Re} = \frac{D_h \rho U_{max}}{\mu}, \tag{4.1}$$

$$\mathrm{Ri} = \frac{gl\left(\rho_2 - \rho_1\right)}{\rho_1 U^2}, \tag{4.2}$$

$$\mathrm{M} = \frac{U_{max}}{c}, \tag{4.3}$$

where U_{max} is the maximum velocity in the channel and c is the speed of sound in air. The hydraulic diameter is defined here as

$$D_h = 4 \times \left(flowarea/perimeter\right). \tag{4.4}$$

Making these assumptions allowed the prescription of an analytic Poiseuille velocity profile everywhere in the fluid domain

$$u_x(y) = \frac{U_{max}}{h^2}\left(h^2 - y^2\right), \tag{4.5}$$

where u_x is the x-component of the velocity vector and y is the vertical ordinate, defined in Figure 4.1. All other velocity components are zero.

An advection-diffusion equation was used to model the temperature and water transport in the fluid. The assumptions made here include:

- The system is in a steady state
- There are no temperature or water source terms
- The fluid velocity is low enough that viscous heating can be ignored
- Mass concentration gradients are negligible
- Diffusion in the x direction is negligible compared to the y direction
- The fluid has constant properties
- Air is treated as a ideal gas
- The flow field is two dimensional

The advection-diffusion equation used for temperature and water transport under the aforementioned assumptions becomes

$$u_x \frac{\partial \theta}{\partial x} - \alpha \frac{\partial^2 \theta}{\partial y^2} = 0, \tag{4.6}$$

where θ is the transported quantity and α is the molecular diffusivity of water in air, α_w, or the thermal diffusivity of air, α_T.

The advection-diffusion equation was discretised using the finite volume method. The maximum element Péclet number for this case was 47 for temperature, and 41 for water transport. The Péclet number being defined as

$$\mathrm{Pe} = \frac{\Delta x u_x}{\alpha}, \tag{4.7}$$

where Δx denotes the mesh element size in the x direction. Because of these large Péclet numbers the transport equation was discretised with a

first order upwind scheme in the streamwise direction, while a second order central scheme was used for the transverse direction.

Solid

The solid conduction layer on the boundaries of the channel allowed for a varying surface temperature in contact with the fluid. Biological heat transfer problems are well studied and the Pennes equation (Pennes (1948)) describes heat transfer in biological tissue. The Pennes equation includes conduction heat transfer and source terms for metabolic heat generation and blood perfusion. Similar to the mucosa, the Pennes equation has proven useful to model heat transfer in the skin (Xu *et al.* (2008)). The Pennes equation for one-dimensional conduction through a layer of tissue is given as

$$\rho c_t \frac{\partial T}{\partial t} = k \frac{\partial^2 T}{\partial y^2} + \omega_b \rho_b c_b \left(T_{blood} - T\right) + S_{met} + S_{ext}, \tag{4.8}$$

where ρ, k, and c_t are the tissue density, thermal conductivity, and specific heat capacity respectively; T and T_{blood} (constant) are the tissue and blood temperatures respectively; t is time; y is the vertical direction, normal to the tissue layer; ω_b is the blood perfusion rate; ρ_b and c_b are the blood density and specific heat capacity respectively; and S_{met} and S_{ext} are the tissue metabolic heat generation and external heat sources.

As seen in Chapter 3 the latent heat flux due to the evaporation of water from the surface of the mucosa accounts for approximately 90% of the total heat flux from the surface. The rate of evaporation is driven by the water transport in the air and will drive a necessary heat flux through the proposed conduction layer. Consequently the mucosa surface temperature will be indirectly determined by this imposed heat flux, the properties of the conduction layer, and the body-side boundary condition. Therefore, a sufficient wall conduction model must replicate the relationship between heat flux and surface temperature that would occur in the real biological system. If we assume the Pennes equation is an accurate representation of the way the true biological system responds we can compare its response to our proposed wall conduction model. In a single layer, at steady state, the Pennes equation can

be solved analytically (Appendix A.1) to give a linear relationship between the surface heat flux and the surface temperature. Similarly, the pure heat conduction transport equation, can be solved analytically (Appendix A.2) and also gives a linear relationship between surface heat flux and surface temperature. Therefore, by modifying the body temperature and the layer thickness or thermal conductivity, it should be possible to tune the proposed wall conduction model to match the response of the full biological system. Using the conduction equation as opposed to the full Pennes equation reduces the number of free parameters required from 8 to 3. Reduction in model parameters consolidates error and simplifies model tuning.

Others have solved the one-dimensional heat conduction equation in a conduction layer to yield a spatially varying surface temperature (Kim *et al.* (2017); Kumahata *et al.* (2010)). Here, instead, the two-dimensional heat conduction equation is solved in the conduction layer, governed by

$$\frac{\partial^2 T}{\partial x^2} + \frac{\partial^2 T}{\partial y^2} = 0. \tag{4.9}$$

Solving in two-dimensions will enable testing of the one-dimensional conduction assumption.

Equation 4.9 was discretised using the finite volume method with a second order central difference gradient approximation.

Coupling

All three transport equations, wall temperature, air temperature, and air water concentration, must be solved simultaneously and must be compatible across the air-solid interface. An energy balance across the interface as in Figure 4.3, gives the energy balance

$$\dot{q}_w = \dot{q}_a + \dot{q}_{latent}, \tag{4.10}$$

where $\dot{q}_w$ is heat flux through the wall, $\dot{q}_a$ is the heat flux into the air, and $\dot{q}_{latent}$ is the heat flux lost as latent heat due to water evaporation. The latent heat flux is given by

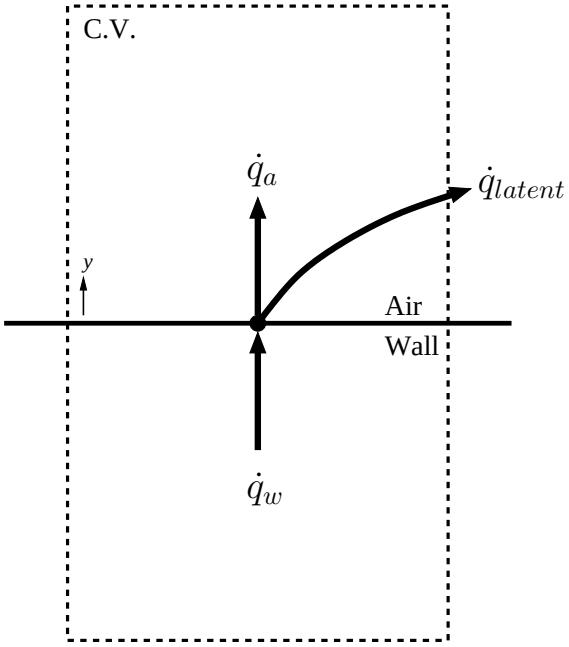

Figure 4.3: Schematic of an energy balance across the wall-air interface.

$$\dot{q}_{latent} = \dot{q}_{water}\Delta\mathcal{H}, \tag{4.11}$$

where $\dot{q}_{water}$ is the water flux from the surface and $\Delta\mathcal{H}$ is the latent heat of evaporation of water.

Equation 4.10 is used to match the three transport equations at the interface. A flow chart of the numerical procedure is presented in Figure 4.4.

First, the heat flux through the conduction layer, $\dot{q}_w$, is initialized and the wall conduction equations are solved with a constant body temperature and with $\dot{q}_w$ imposed on the fluid side. This yields a surface wall temperature, T_w, which is used as the wall boundary condition to solve for the temperature in the fluid. The wall temperature is also used to calculate the wall water concentration, C_w, using the method described later in Section 4.3.2. This wall water concentration is used as the wall boundary condition to solve the water transport in the fluid. Now that the temperature and water concentration distributions in the fluid are known, they are used to calculate the air and latent hear fluxes, $\dot{q}_a$ and $\dot{q}_{latent}$. These are summed to calculate the

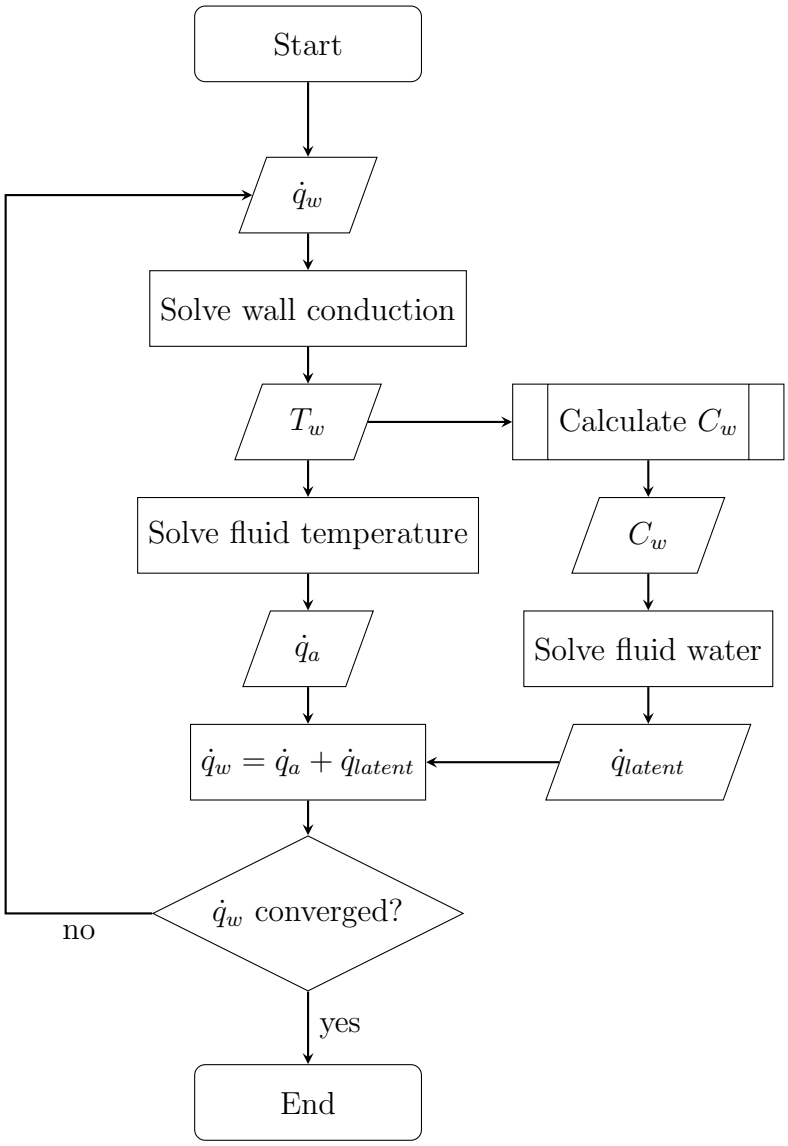

Figure 4.4: Transport equation coupling solution method.

wall heat flux, $\dot{q}_w$, which is then compared to the wall heat flux used at the start of the iteration. If not yet converged, the wall heat flux is updated and the entire process is repeated, otherwise the simulation is complete.

Drying

A novel mechanism to model the drying of the mucosa is proposed. It is hypothesised that the nasal mucosa has a maximum mucus producing capacity. When water evaporation from the mucosal surface exceeds this maximum capacity on average then the surface begins to dry out. The dry surface will act as though it has reduced relative humidity. With the steady state approximation, this method should be effective.

The water concentration on the wall is first chosen to be 100% relative humidity to model a wet mucus layer. The absolute humidity at this condition is then determined from the wall temperature. To do this, the saturation vapour pressure is first calculated using a Magnus form approximation from Abbot and Tabony (Abbott & Tabony (1985))

$$E_w = 6.107 \exp\left(\frac{17.38T}{239+T}\right), \tag{4.12}$$

where E_w is the saturation vapour pressure of water in hPa, and T is in °C. The Abbot-Tabony formulation was shown to be more accurate than a number of other formulations over a biologically relevant temperature range, 25-37 °C (Alduchov & Eskridge (1996)). The saturation vapour pressure is converted to a molar concentration using the ideal gas law (assuming the air-water mixture acts as an ideal gas)

$$C_M = \frac{n}{V} = \frac{E_w}{RT}, \tag{4.13}$$

where C_M is the molar concentration, n is the number of moles of water, V is the volume it occupies, and R is the universal gas constant ($R = 8.314$ J/mol K). The absolute humidity can then be calculated as

$$C_w = C_M * M, \tag{4.14}$$

where M is the molar mass of water, 18 g/mol.

To simulate the drying process, a maximum water flux sustainable by the mucus layer is chosen. The water transport in the fluid is then solved once using this water flux as the wall boundary condition. The result is an absolute humidity on the wall that corresponds to the maximum sustainable water flux. When solving the system of equations as in Figure 4.4, before water transport is solved, the water concentration boundary condition is modified so that it is the minimum of the saturated concentration and the pre-calculated maximum concentration. This mechanism is shown in Figure 4.5 and defines the process 'Calculate C_w' in Figure 4.4. The limitation of this method is that it requires that the water flux on the surface decreases monotonically in the x-direction. The advantage of this method is that it avoids having to iterate the entire solution procedure again to meet it, the only iteration required is to couple the transport equations. This approach works well for the channel case, its utility on more complex geometries is yet to be determined.

4.3.3 Boundary conditions and material properties

Material properties

The material properties used are presented in Table 4.2. The thermal conductivity of the wall layer is somewhat arbitrary for the function of the wall model, though here we chose it be equal to the thermal conductivity of the dermis (Cohen (1977)).

Inlet

The fluid velocity was specified everywhere in the domain (Section 4.3.2). A U_{max} of 1.68 m/s was chosen to define the velocity profile as in Equation 4.5. This velocity was chosen to make the mean velocity match the bulk velocity seen in the normal nasal cavity that was simulated in Chapter 3. The incoming air was chosen to be 25 °C at 30% relative humidity (6.91×10^{-3} kg/m^3 (Jones (1994))), equivalent to the room conditions used in Lindemann *et*

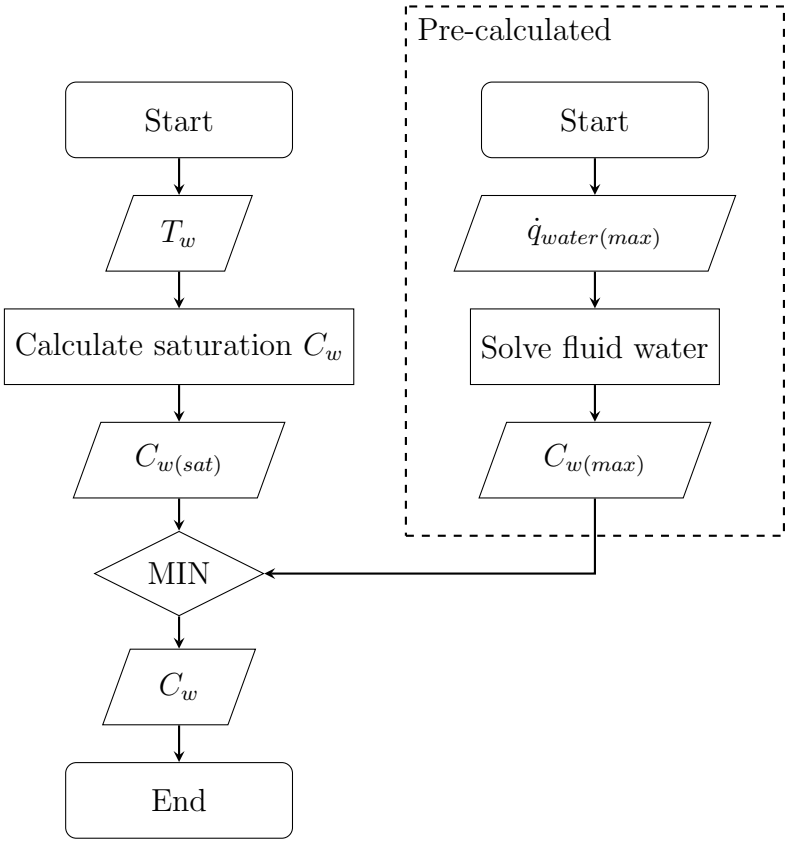

Figure 4.5: Implementation of the drying model for calculation of C_w. This defines the process, 'Calculate C_w' in Figure 4.4.

Fluid	
Property	Value
Density, ρ	1.18 kg/m^3
Dynamic viscosity, μ	1.84×10^{-5} kg/m s
Thermal diffusivity, α_T	2.22×10^{-5} m^2/s
Molecular diffusivity of water in air, α_w	2.56×10^{-5} m^2/s
Latent heat of evaporation of water, $\Delta\mathcal{H}$	2.43×10^6 J/kg
Conduction layer	
Property	Value
Thermal conductivity, k_{wall}	0.322 W/m K

Table 4.2: Material properties nominally at 25°C (Çengel *et al.* (2012); Hall & Pruppacher (1976); Cohen (1977)).

al.'s *in vivo* measurement of nasal mucosal temperatures during breathing (Lindemann *et al.* (2002)).

Outlet

Using a first order upwind scheme meant that no boundary treatment was required on the outlet.

Conduction layer

The conduction layer requires two input parameters, body temperature and layer thickness. These parameters must be determined from the steady solution to the Pennes equation to ensure that the conduction layer model responds similarly to the real system.

The boundary condition must maintain the relationship between the surface temperature and the surface heat flux, written as

$$T(w) = A\dot{q}_w + B, \tag{4.15}$$

where A and B are constants (See Appendix A). The conduction layer model must be tuned to match these constants as determined by the Pennes equation. For the Pennes solution, A and B are defined as follows

$$A = \frac{\mathrm{e}^{w\beta} - \mathrm{e}^{-w\beta}}{k\beta\left(-\mathrm{e}^{w\beta} - \mathrm{e}^{-w\beta}\right)}, \tag{4.16}$$

$$B = \left(T_b - \frac{S_{met}}{\omega_b \rho_b c_b} - T_{blood}\right)\left(\mathrm{e}^{w\beta} + \frac{\mathrm{e}^{2w\beta} - 1}{-\mathrm{e}^{w\beta} - \mathrm{e}^{-w\beta}}\right) + T_{blood} + \frac{S_{met}}{\omega_b \rho_b c_b}. \tag{4.17}$$

where $\beta = \sqrt{\frac{\omega_b \rho_b c_b}{k}}$. We can estimate these parameters using estimates of the physiological parameters, as presented in Table 4.3. The thermal conductivity of tissue and the metabolic heat generation were estimated from reported values of the skin's dermis, the density of the blood was assumed to be similar to that of water, and the blood perfusion rate was taken from measurements in the inferior turbinate. The blood temperature was assumed

Property	Value	Reference
Thermal conductivity of tissue, k	0.322 W/m K	(Cohen (1977))
Density of blood, ρ_b	1000 kg/m^3	*estimate*
Specific heat capacity of blood, c_b	3770 J/kg K	(Torvi & Dale (1994))
Blood perfusion rate, ω_b	0.0065 m^3_{blood}/m^3_{tissue} s	(Olsson & Bende (1985))
Metabolic heat generation, S_{met}	368.1 W/m^3	(Xu *et al.* (2008))
Temperature of blood, T_{blood}	37°C	*estimate*
Temperature of body, T_b	37°C	*estimate*

Table 4.3: Physiological properties used for the solution to the Pennes equation.

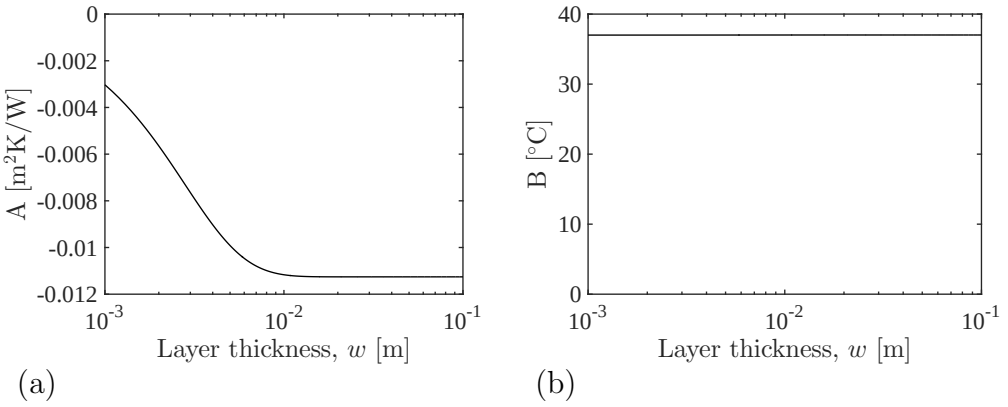

Figure 4.6: Constants A and B with layer thickness, w.

to be 37°C. The Pennes equation was solved on a layer of tissue, of thickness w, that is sufficiently thick so that the body facing boundary was at body temperature, T_b, of 37°C. Substituting the parameters from Table 4.3 we get numerical estimates for A and B that vary with the layer thickness, w, as shown in Figure 4.6. At large w, above about 0.01 m, both A and B reach constant values of

$$A = -0.0113\ m^2K/W, \tag{4.18}$$

$$B = 37°\text{C}. \tag{4.19}$$

These can be matched with the corresponding constants in the conduction

layer model (Appendix A)

$$A = \frac{-w}{k}, \tag{4.20}$$

$$B = T_b, \tag{4.21}$$

to give values for the conduction layer thickness, w, and the conduction layer body temp, T_b, of

$$w = 0.00364\ m, \tag{4.22}$$

$$T_b = 37°\text{C}. \tag{4.23}$$

Zero flux conditions were applied to the side boundaries of the conduction layer.

Drying model

The drying model requires an estimate of the maximum water flux that the mucosa is able to sustain. This estimate was based on the sum of two components, the total evaporative water lost through the nose due to respiration, and the average rate of clearance of the mucus layer.

Humans loose about 300-400 ml water through the upper airways every 24 hours (Proctor & Andersen (1982)). If we assume that most of the air conditioning occurs in the nasal cavity, we can use the surface area of the normal nasal cavity simulated in Chapter 3 to convert this to a mean water flux from the nasal mucosa of 1.5-2.0$\times 10^{-4}$ kg/m^2 s.

The mucus layer is normally about 10 μm thick (Mygind & Dahl (1998)) with a mean clearance rate of approximately 6 mm/min (Proctor & Andersen (1982)). The average water flux from the surface required to sustain this mucus clearance rate can be calculated as,

$$\dot{q}_{water} = \frac{\rho U w}{L}, \tag{4.24}$$

where ρ is the density of the mucus (estimated as 1000 kg/m^3), U is the mucus clearance velocity, w is the mucus layer thickness, and L is the length of the mucus layer (approximated as 0.125 m). This gives a water flux of 8×10^{-6} kg/m^2 s.

Since we are modelling steady inspiration only, and if we assume that water flux from the mucus layer only occurs during inspiration, the maximum water flux that can be sustained during steady inspiration should be the mean over all time, as previously calculated, divided by the fraction of time that humans spend inspiring, 0.42 (Tobin *et al.* (1983)). Adding the components from evaporation and mucociliary transport and dividing by fractional inspiratory time yields an estimate of the maximum sustainable water flux for use in the drying model,

$$\dot{q}_{water(max)} = 4.4 \times 10^{-4} \text{ kg/m}^2\,\text{s}. \tag{4.25}$$

4.3.4 Mesh-independence analysis

To evaluate the mesh-independence of the results the mean total heat flux through the channel walls and the mean fluid temperature in the channel were compared, as shown in Figures 4.7 and 4.8. For this comparison the drying model was turned off and similar parameters to that used for the final simulations were used.

Three mesh metrics were refined independently from a base mesh: the number of cells in the y-direction in the conduction wall, 'wall refinement'; the number of cells in the y-direction in the channel 'channel refinement'; and the number of cells in the x-direction in the whole domain 'x refinement'. The effect of each of these refinements are most clearly seen in Figure 4.7. Wall refinement has no effect on the mean total heat flux. Channel refinement and x refinement both become nearly insensitive to their respective element sizes by the finest refinement of each. The final mesh used the lowest possible wall refinement, 2 cells in the y-direction, and the maximum that was tested in the channel y-direction, 160 cells, and in the x-direction, 200 cells, resulting in a mesh with a total of 32800 cells.

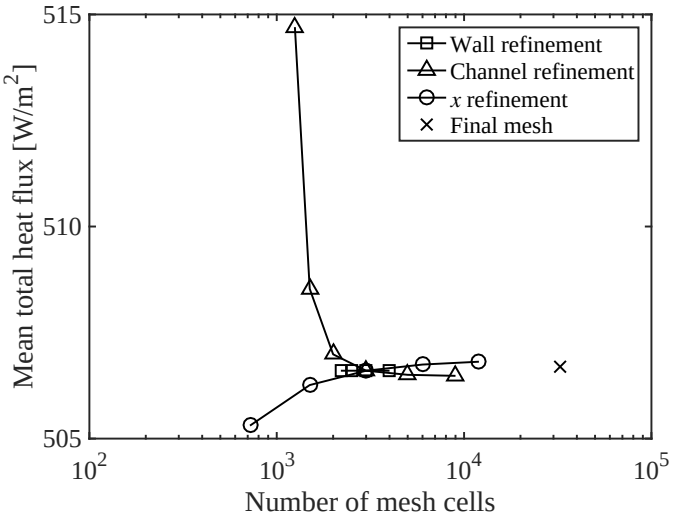

Figure 4.7: The mean total heat flux from the channel wall as the mesh is refined in the y-direction in the channel and the wall, and in the x-direction throughout the domain.

The final mesh of 32800 cells was then compared to the baseline mesh of 3000 cells in Figure 4.8. There was minimal difference in the mean fluid temperature between the two meshes.

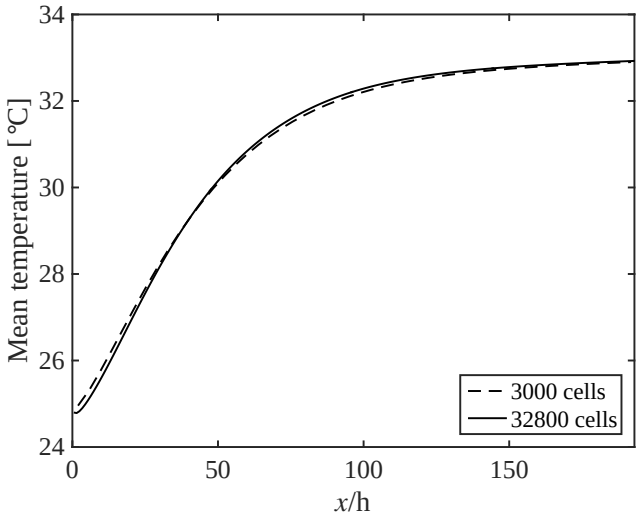

Figure 4.8: The mean fluid temperature in the channel with x-position at two mesh resolutions.

4.3.5 Verification

The numerical methods were verified by comparing them to analytical results in Figure 4.9.

The wall conduction solver was tested with a temperature of 37°C at y = 0 m and a heat flux out of the domain of 1000 W/m^2 at y = 0.004 m and compared to the analytical one-dimensional heat transfer result (Figure 4.9(a)). The simulated result matches the analytical result exactly.

The advection-diffusion solver for temperature in the fluid was tested with the same parameters as used for this study, with an inlet temperature of 25°C and a constant wall temperature of 37° (Figure 4.9(b)). The temperature profile in the simulated solution develops until $x/\mathrm{h} = 11$ after which it reaches a thermally fully developed state until $x/\mathrm{h} = 78$ when the system begins to decay to thermal equilibrium. The Nusselt number in the thermally fully developed region matches well with the analytical solution from Kays and Crawford (Kays & Crawford (1980)). The Nusselt number is defined as

$$\mathrm{Nu} = \frac{h_c D_h}{k}, \tag{4.26}$$

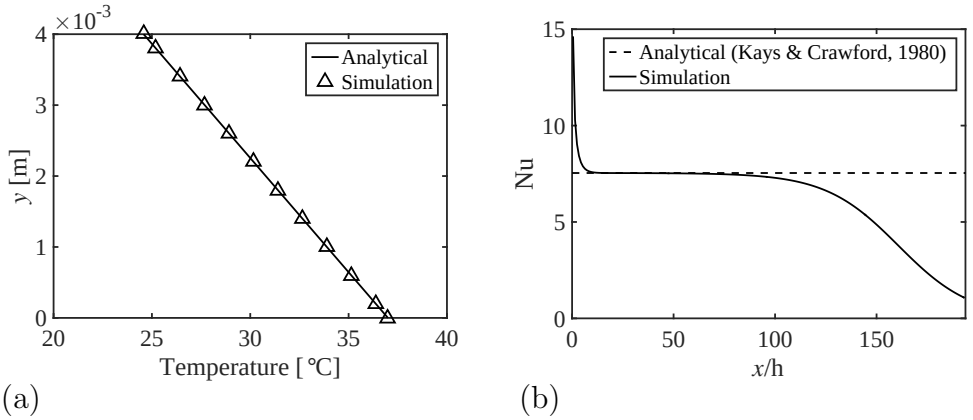

Figure 4.9: Verification of (a) the wall conduction and (b) the channel advection-diffusion solvers.

where h_c is the convective heat transfer coefficient.

4.4 Results

4.4.1 Full drying model

The results from the channel simulation with the full drying model are shown in Figure 4.10. At large x/h both results look nominal for a channel flow. Near the entrance of the channel, though, the temperature remains relatively constant for a period of time before the fluid begins to heat up significantly.

The heat flux and temperature on the wall are presented in Figure 4.11 with positive values indicating heat transfer from the wall to the fluid. Latent heat flux is the dominant component of the total wall heat flux. Up to $x/\mathrm{h} \approx 27$ the latent heat is limited by the drying model causing a plateau of total heat flux and a near zero sensible heat flux from the cold wall. Once the latent heat flux becomes no-longer saturated the sensible heat flux begins to build and a small peak in total heat flux occurs forming the global maximum. This small peak is actually caused by heat flux in the negative x-direction transferring energy from the adjacent, relatively warm, wall. When a one-dimensional model is used the peak disappears. The wall temperature

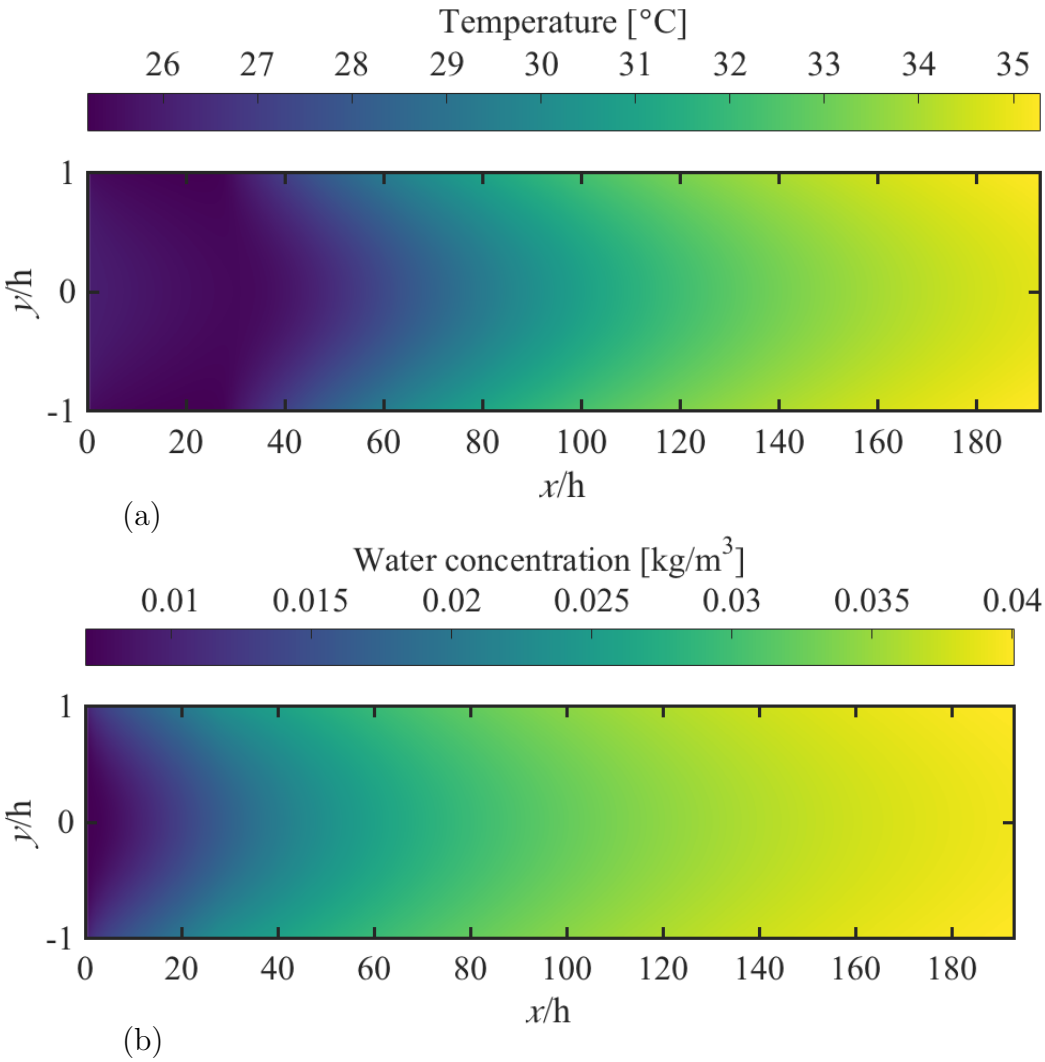

Figure 4.10: Temperature and water concentration in the channel.

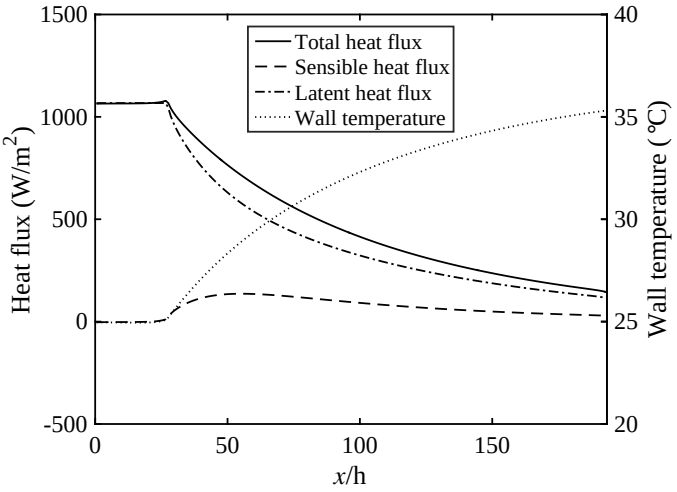

Figure 4.11: Heat flux components and wall temperature in the channel using the full drying model. Positive heat flux indicates heat transfer from the wall to the fluid.

begins steady at about 25°C as all the heat flux being supplied across the conduction wall is consumed as latent heat flux to humidify the dry incoming air. The temperature then rises towards the end of the channel. The mean wall temperature of 31.0°C is similar to the mean of 31.7°C seen *in vivo* during inspiration by Lindemann *et al.* (Lindemann *et al.* (2002)).

The total heat flux profile is sensitive to the model parameters and the inlet conditions. Results for the same case except with an inlet temperature 1°C higher, 26°C, is shown in Figure 4.12. Now the cold wall, driven by the latent heat flux, cools the air, providing a negative sensible heat flux and a lower total heat flux at the entrance to the channel. This negative sensible heat flux indicates that the air is providing some of the latent heat flux requirement. While this is small compared to the fraction provided by the wall, the temperature of the air is significantly affected by this process.

The relative humidity on the channel wall is presented in Figure 4.13. The relative humidity quantifies the dryness of the mucosal surface. Before $x/\mathrm{h} \approx 27$ mucus production would not be able to keep up with the water flux from a wet surface at 100% RH, so it compensates by effectively presenting

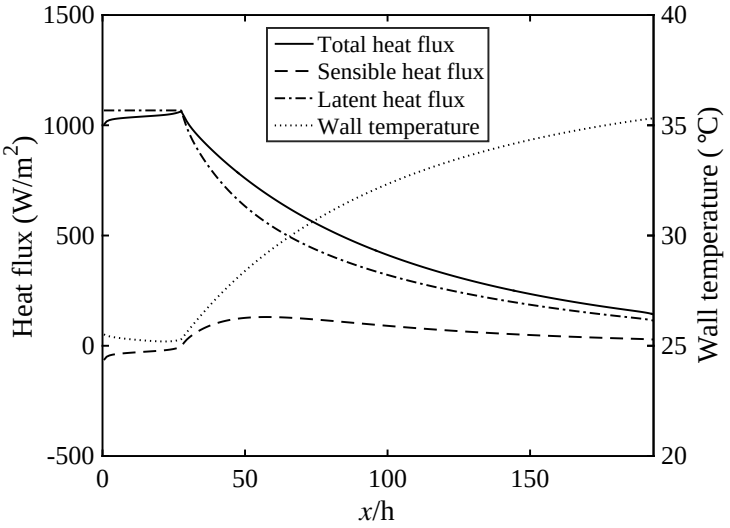

Figure 4.12: Heat flux components and wall temperature in the channel using the full drying model with an inlet temperature of 26°C. Positive heat flux indicates heat transfer from the wall to the fluid.

a relative humidity below saturated to the airflow in the channel.

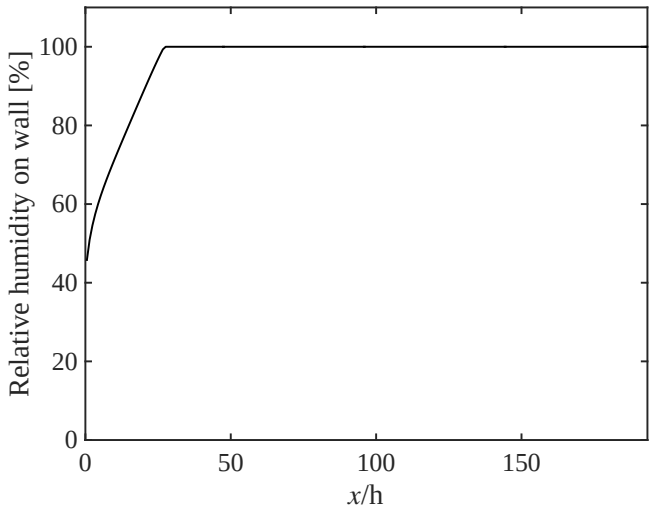

Figure 4.13: Relative humidity on the wall in the full drying model.

4.4.2 Boundary condition comparison

The full drying model was compared to the same case without the drying model, using only the variable temperature conduction layer model, and to the same case with a constant wall temperature equal to the mean temperature from the drying case. Heat and water fluxes along with the wall temperature using each boundary condition is presented in Figure 4.14.

Compared to the other cases, the total wall heat flux in the constant temperature case reaches much higher values near the entrance of the channel, and it decays rapidly to near zero by half way through (Figure 4.14(a)). The variable temperature boundary condition and the drying model are very similar for most of the channel. Early in the channel though, the heat flux is limited in the drying model but not in the variable temperature model.

The water flux shows similar behaviour to the total heat flux (Figure 4.14(b)). A naive prediction of mucosal dryness could be made using the variable temperature boundary where the water flux exceeds the specified maximum. However, this naive method would under-predict the area of dry mucosa, compared to that predicted by the drying model, by approximately

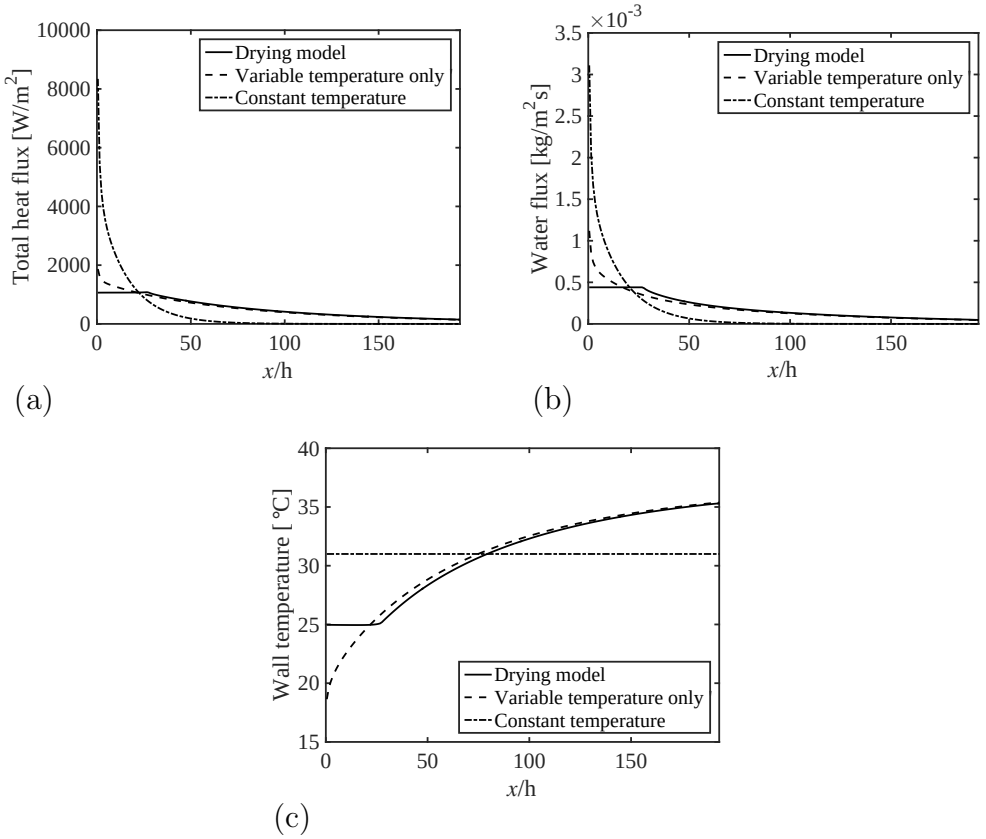

Figure 4.14: Boundary condition comparison between the full drying model, only the variable temperature model, and a constant temperature case. (a) total wall heat flux, (b) wall water flux, (c) wall temperature.

40% in this geometry.

The temperature at the wall in the variable wall temperature case begins well below ambient due to the high latent heat flux at the entrance to the channel (Figure 4.14(c)). All other cases remain at or above the ambient temperature and, following the entrance region, both the variable wall temp and the drying model cases show similar wall temperatures rising to about 35.3°C at the exit.

The conditioning of the air using each boundary condition are compared in Figure 4.15. The temperature rises much faster in the constant wall temperature case but levels off quickly to near wall temperature resulting in a

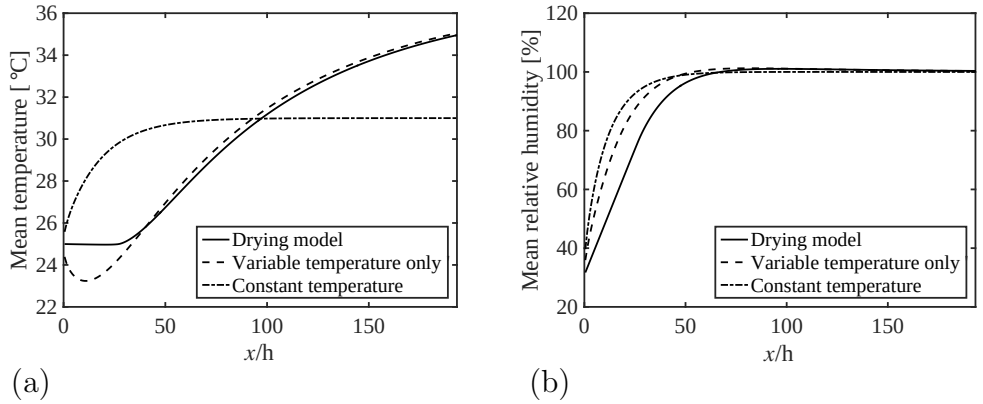

Figure 4.15: Boundary condition comparison between the full drying model, only the variable temperature model, and a constant temperature case. (a) mean air temperature, (b) mean relative humidity.

lower outlet temperature than the other cases (Figure 4.15(a)). The temperature matches well between the variable wall temperature and the drying model for much of the channel. At the entrance, the variable wall temperature case produces the lowest mean temperature, lower than ambient, as the air is cooled due to high latent heat loss in this area.

The constant temperature case humidifies the air the fastest, followed by the variable temperature model, and finally the drying model (Figure 4.15(b)). This result may reflect how each model would predict the air-conditioning capacity of a human nose, with both the variable temperature and constant temperature models over-predicting compared to the drying model.

4.4.3 Effect of streamwise wall conduction

Heat flux in the x-direction in the conduction layer is shown in Figure 4.16 with the original resolution in panel (a) and a higher resolution in panel (b). Axial heat flux in the conduction layer is driven by the temperature gradient on the surface where the wall interacts with the fluid. Despite the presence of heat fluxes on the order of -80 W/m^2 these are concentrated in

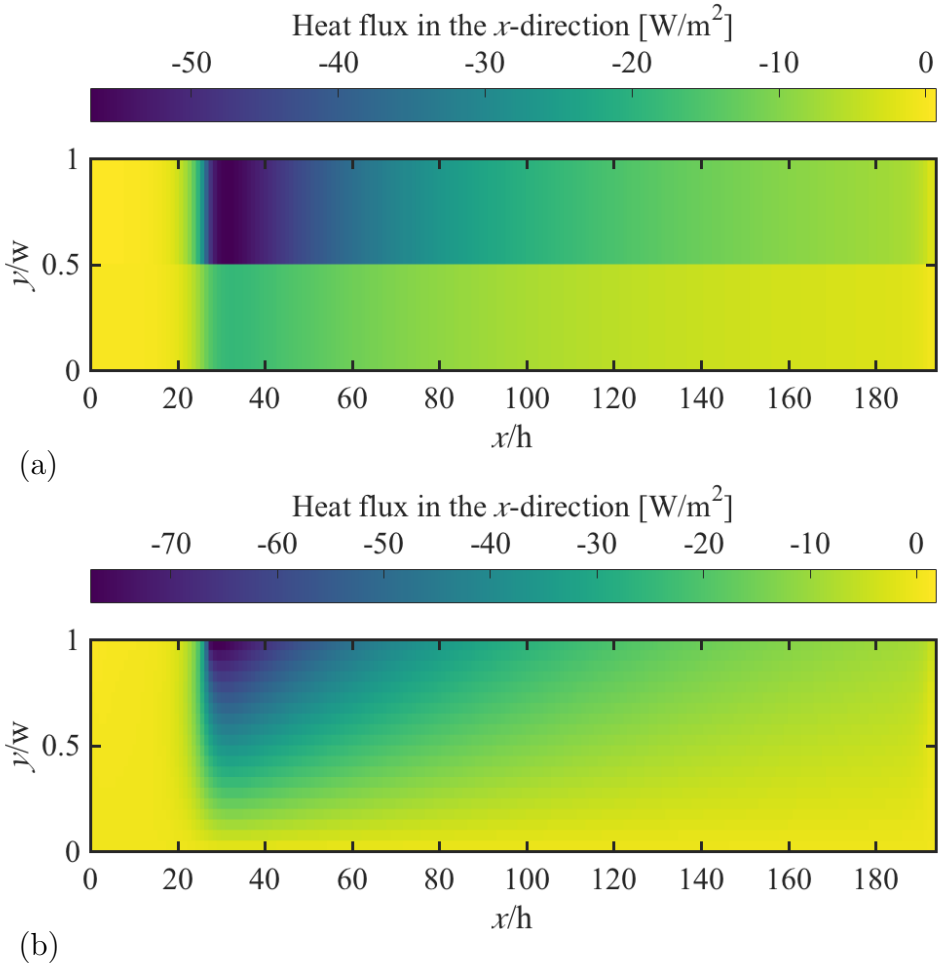

Figure 4.16: Heat flux in the x-direction within the conduction layer for (a) the nominal case, (b) a more refined wall conduction layer mesh.

a small proportion of the wall and are of insignificant magnitude compared to the total heat flux being transferred through the wall into the fluid of ≈ 1000 W/m^2. As seen earlier in Figure 4.12 heat flux in the x-direction is responsible for a small peak in the total heat flux from the wall, though this is relatively small. It is likely safe to assume that heat flux in the x-direction can be ignored in the wall. Temperature gradients in the x-direction in the fluid are of a similar magnitude to those seen at the wall surface and the thermal conductivity is about 10 times lower than that of the wall, so these can safely be assumed negligible also.

4.5 Discussion

4.5.1 Implications for nasal CFD

Using the proposed drying model the dryness of the mucosa may be quantified by the relative humidity on the wall. If this model proves to be accurate, then it could allow for the prediction of the breakdown of mucosal clearance, and potentially the health of the nasal mucosa.

The constant wall temperature boundary condition produced results that were significantly different from the variable temperature and drying model cases in terms of wall heat flux and conditioning of the inspired air. The variable wall temperature case and the drying model produced similar results in the areas of the channel that were not dry, though air-conditioning was less affective with the drying model. Because it is known that the mucosal temperature in the nasal cavity varies with location (Lindemann *et al.* (2002)) these result suggest that CFD of the nasal cavity including a constant temperature boundary condition may be significantly inaccurate, especially in terms of heat flux magnitudes and air-conditioning. Compared to the proposed drying model, it was not sufficient to predict drying by simply looking at where the water flux exceeded a maximum value when using the variable temperature model. A dedicated drying model is likely required to reliably predict dryness.

In this geometry both the constant and the variable wall temperature cases produced monotonically decreasing heat flux profiles with x-location. This may indicate that both conditions would perform similarly in identifying locations of higher heat flux in a nasal cavity simulation. The drying model, however, does not always produce a monotonically decreasing total heat flux and may produce a global maximum where the wall becomes saturated. This non-monotonic trend may have implications for the certainty of conclusions drawn from the relative magnitude and locations of heat flux in past CFD studies.

While, in this simulation, most of the latent heat was provided by the wall rather than the air, the latent heat flux indirectly impacts the heating

of the air by influencing the wall surface temperature. Latent heat should be included in future nasal CFD studies that wish to accurately capture air and wall temperatures.

4.5.2 Limitations

In it's present form, some limitations must be addressed before this drying model can be applied to full scale CFD. The most obvious limitation is the simplified geometry tested here. It was easy to implement the boundary condition on the simple channel flow, it provided for simple comparison between cases, and allowed the behaviour of this model to be clearly displayed. But, the use of a simplified geometry makes it difficult to extrapolate the results to what would be observed in a realistic nasal simulation. Further, and most importantly, more complex geometries may result in a flow field that violates the main physical limitation of this drying model which is that water flux must monotonically decrease along the surface in the streamwise direction.

For simplicity, this work considered the air and the wall with constant properties, including a constant maximum water flux across the wall. The implication of this assumption is not known.

This drying model was conceived without reference to the structure of the mucus layer itself and focuses only on numerical methods that could be used to achieve a response akin to drying.

The model presented here considers steady flow and drying out of the mucosa in the mean sense. While this may turn out to be sufficient for clinical use, in reality breathing is not a steady process and additional interactions like condensation during expiration will occur. The mucus layer is also not static, it likely responds to the environment around it and is constantly secreting and transporting mucus. This model makes a first attempt at the problem of modelling mucosal drying but it should be acknowledged that there are likely more complex affects that could be necessary for a truly accurate drying model.

In its current form, the numerical methods proposed here to implement the drying model requires an iterative process which would make high reso-

lution and time-dependent solution computationally prohibitive. The use of an analytical one-dimensional conduction layer model may enable improvements to the numerical procedures, but further numerical improvement will be required for this method to become useful in expensive nasal CFD calculations.

4.6 Conclusions

A novel model to predict dryness in the human nasal cavity for use in CFD has been proposed and tested on a simple channel flow. The model allows the prediction of dryness and the effect that dryness has on heat and water transport in the geometry. It was proven that a simple conduction layer boundary condition is sufficient to replicate the temperature/heat-flux response of the nasal wall and the more complex Pennes physiological model is not required. A conduction layer provides a simple method to accurately include surface temperature variation in a CFD simulation. The proposed model can be tuned with two parameters which have been estimated here based on realistic physiological properties. The proposed dryness model limits the water flux in the geometry to a specified maximum value. In the steady state, exceeding this maximum value would result in drying out of the mucosa over time. A crude estimation for the maximum sustainable water flux from the nasal mucosa for use in the drying model has been made.

Heat transfer in the streamwise direction can likely be safely ignored in wall conduction models, allowing an analytical boundary condition to be imposed. The effect that latent heat has on the temperature in the geometry is significant and should not be ignored.

A comparison of constant temperature, variable temperature, and drying model boundary conditions was made in a channel flow. The constant temperature boundary condition poorly predicted heat fluxes and air-conditioning compared to the other, more sophisticated, models. The use of constant temperature boundary conditions should be limited in nasal CFD where heat and water transport is important. A dedicated drying model is likely required for accurate prediction of mucosal dryness, as inference simply

from the variable temperature case was inaccurate. The introduction of the dryness model can produce a non-monotonic distribution of total heat flux through the wall. This may render conclusions based on relative heat fluxes and heat flux location uncertain. Development of drying models for use in full scale, realistic, nasal CFD simulation is likely necessary for the evaluation of nasal health and further research of enigmatic nasal conditions such as empty nose syndrome. This model remains to be validated and extended to complex geometry.

Chapter 5

Conclusions

The current state of understanding of the enigmatic condition, empty nose syndrome, has been critically assessed and an attempt has been made to improve understanding of this condition through computational fluid mechanics. The utility of current CFD practice for the study of ENS has been assessed and a springboard has been laid for future application of CFD to the study of ENS. Our understanding of the pathophysiology of ENS is advanced here through exclusion of possible mechanisms.

There has been a number of attempts to review literature addressing possible mechanisms by which ENS may manifest, though many of them similarly conclude that a number of commonly quoted factors may be involved somehow. Objective tests of proposed mechanisms are lacking, or have been overlooked in existing literature reviews. Here, critical evaluation of these proposed mechanisms allowed a number to be excluded, narrowing the scope of possible explanations for further research. It is likely that psychological fault, lack of normal airflow sensation through thermoreceptor activation (due to fluid dynamic or neurological factors), and nasal resistance are likely not responsible for the sensation of nasal obstruction reported by ENS patients. It is more likely that the abnormal sensations felt in ENS are caused by the stimulation of distinct sensations not normally felt during breathing, a novel hypothesis. It is most likely that this abnormal sensation is driven by complex interactions between airflow in the nasal cavity and its

sensitive mucosal lining.

The conclusion that ENS is likely related to nasal airflow demands the use of CFD to further our understanding of likely pathophysiological mechanisms. Computational fluid dynamics is the only tool that can allow analysis of the entire nasal flow field and the interaction between the air and the mucosa throughout the nasal cavity. There are few CFD studies of ENS nasal cavities though it is clearly necessary to further ENS understanding. Here, high resolution time-dependent CFD simulation of a number of ENS nasal cavities, before and after corrective surgeries, and that of a normal nasal cavity has been performed and presented. The results were discussed with reference to patient reported outcomes from standard, validated, clinical outcome questionnaires. The results did not support the hypotheses that air-conditioning capacity, nasal surface area, transnasal pressure loss, or lack of thermoreceptor activation by heat flux play a significant role in the pathophysiology of ENS. In agreement with other studies, these results seem to corroborate a correlation between a deficit in inferior wall shear stress and the presence of ENS symptoms.

Due to the crucial role that the nasal mucosa plays in force and heat transmission between the air and tissue, it was postulated here that mucosal health and the state of the mucus layer could offer a universal mechanism for many reported physiological symptoms of ENS. This hypothesis is yet to be investigated. The state of the mucus layer is driven by the overlying fluid dynamics, and any investigation of this hypothesis likely requires CFD with boundary conditions that can sufficiently capture the air-mucosa interaction. A few boundary treatments were tested here on Poiseuille flow. It was shown that a simple thermal conduction layer on the boundary of the domain can sufficiently capture surface temperature variation in the nasal cavity. The conduction layer has been tuned using two parameters to match the response predicted by the Pennes biological heat transfer equations for tissue surface. Additionally, a novel mechanism to predict surface drying has been implemented. The variable temperature condition and the drying condition were compared to a constant surface temperature condition. In Poiseuille flow the constant temperature condition showed poor agreement

with the other two models in determining heat and water flux from the surface. There was little agreement between any of the boundary conditions when predicting air conditioning. It was found that the introduction of a dryness model may have implications for the location of the highest heat fluxes in the geometry. More accurate boundary conditions including latent heat, variable wall temperature, and mucosal drying should be explored in CFD of ENS nasal cavities. The drying model presented here is yet to be validated and extended to complex geometry.

5.1 List of contributions

The most important original contributions made by the present work include:

- Abnormal breathing sensations in empty nose syndrome are likely not caused by psychological factors, neurosensory damage, nasal resistance, nasal surface area, lack of thermoreceptor activation or poor air-conditioning capacity. We hypothesize that the introduction of a unique mucosal sensation driven by abnormal nasal airflow patterns is important to the pathophysiology of ENS. This may be related to:
  - A deficit in inferior wall shear stress
  - Mucosal health and the condition of the mucus layer (original hypothesis)
- First high resolution, time dependent, simulation of ENS nasal geometries. First comparison of patient geometry before and after surgery that improved ENS symptoms, with quantification of the magnitude of these improvements using standard questionnaires.
- In our sample (n=2) symptoms related to ear discomfort correlated with elevated turbulence levels in the nasopharynx. Additionally, dryness, as identified by the ENS6Q, correlated with poor air-conditioning capacity which may cause dryness in the pharynx.

- A novel method to predict mucosal dryness has been proposed and implemented in Poiseuille flow. Introduction of a drying model may have implications for the location of maximum heat flux in the nasal geometry.
- We provide a proof that a heat conducting layer can accurately facilitate surface temperature variation in a similar way to that predicted by the Pennes biological heat transfer model. We have presented estimates for the parameters required by the conducting layer model to accurately replicate the Pennes response.
- A number of different boundary treatments have been compared in Poiseuille flow.

Chapter 6

Future work

Our knowledge of empty nose syndrome remains poor, and much further research will be required before we can grasp the pathophysiology underlying this condition. It is hoped that the work presented here helps narrow down the list of possible research directions and helps to provide a basis for future work. There are number of research groups actively working towards understanding ENS, and it seems promising that strides will be made in the near future.

Here we present a list of potential future research directions which, in the author's opinion, will lead to meaningful outcomes for ENS research. One thing that is apparent from this work and others is that CFD will be a key tool for ENS research, and targeted advancement of numerical methods will likely yield useful outcomes.

6.1 Testing proposed hypotheses

A number of hypotheses have been speculated here and remain to be tested. The chief hypothesis being that the sensations related to ENS are caused by a distinct, abnormal, sensation rather than the lack of a normal one. This can easily be tested by anaesthetising the nasal cavities of ENS patients and seeing if their sensation disappears. If these sensations are distinct, we should be able to suppress them in ENS nasal cavities and reproduce them in the

normal nose. Attempts to do this will likely advance our understanding of the sensations involved. For example, locally anaesthetising different parts of the nasal cavity independently in both ENS and normal nasal cavities will also likely produce useful results.

Two possible mechanisms important to ENS proposed here are spatial variation in wall shear stress and the state of the mucus layer. Studies that can test these both *in silico* and *in vivo* would be useful.

Correlations were found between air-conditioning and a sensation of dryness, and between increased levels of turbulence in the nasopharynx and ear related symptoms. These can be simply tested *in vivo* by inserting probes into the nasopharynx of affected patients.

6.2 Clinical research

Clinicians should continue to identify ENS patients and rigorously record the progression of both their geometric and symptomatic state to increase the database off which ENS research can be based.

It is likely that different areas of the nasal mucosa respond differently to sensory inputs and vary in mucus secretion capacity. Any information on this variation in the nasal mucosa would be useful in determining if the function of the ENS mucosa has been modified by surgery, or how the airflow interacts with different parts of the nasal cavity.

There have recently been a couple of studies that have reported reduced menthol sensitivity in ENS patients (Konstantinidis *et al.* (2017); Li *et al.* (2017)). It may be useful to perform CFD or an *in vivo* study to determine if this is caused by fluid dynamics or physiology.

6.3 Development of computational fluid dynamics for empty nose syndrome

Computational fluid dynamics is a powerful tool, and further simulations of ENS nasal cavities are warranted. However, it is important that future CFD includes variable temperature boundary conditions and account for the effect of latent heat on temperatures in the nasal cavity. There have not yet been any substantial conclusions about the pathophysiology of ENS made from CFD simulation, though it is the authors opinion that this is likely due to missing physics in simulation. It was shown here that variable temperature boundary conditions and the latent heat effect are likely important mechanisms that have been overlooked in the past.

The nasal mucosa acts as the vector through which force and heat are transferred between the air and the tissue making it important to how airflow may be felt in the nasal cavity. More accurate modelling of the mucosa including the mucus layer, secretion, and perhaps the underlying cilia will likely allow insight in to airflow sensation through CFD. The simplest feature of the mucosa that has not yet been modelled in ENS patients is the interaction of water flux on the mucus layer and the subsequent effect this has on the air in the nasal cavity. A simple drying model has been proposed here, and future work should aim to adapt this, or other models, for use in complex geometry and high resolution CFD. In order to be confident in these results, a method of validation should be sought.

In the more distant future it may be necessary to include more detailed models of the mucosa. This may include information about the make up of the sol and gel parts of the mucus layer, ciliary action, and secretion control. Additionally it may be necessary to simulate the entire breathing cycle, in which case mucosal models should be extended to allow for condensation on expiration.

6.4 Translation of computational results for clinical use

It is important that computational results don't get lost in the literature due perhaps to the technical nature of such reports. Once we begin to gather important conclusions about ENS from simulation, it is important that engineers and medical doctors collaborate to translate CFD findings into clinically meaningful and interpretable results or guidelines.

It is sometimes desirable to publish CFD findings relevant to ENS in rhinology journals so that it reaches an interested audience, however it must be ensured that these publications are properly peer-reviewed not only by medical professionals but by someone proficient in CFD. Computational fluid dynamics can easily produce unreliable results if not implemented with care, and proper peer-review will be necessary for CFD to be viewed as a reliable tool in the medical community.

Bibliography

Aasvang, E. K. & Kehlet, H. 2010 Persistent sensory dysfunction in pain-free herniotomy. *Acta. Anaeshesiol. Scand.* **54**, 291–298.

Abbott, P. F. & Tabony, R. C. 1985 The estimation of humidity parameters. *Meteorol. Mag.* **114**, 49–56.

Alduchov, O. A. & Eskridge, R. E. 1996 Improved magnus form approximation of saturation vapor pressure. *J. Appl. Meteorol.* **35**, 601–609.

Arbia, G., Corsini, C., Esmaily-Moghadam, M., Marsden, A. L., Migliavacca, F., Pennati, G., Hsia, T.-Y. & Vignon-Clementel, I. E. 2014 Numerical blood flow simulation in surgical corrections: what do we need for an accurate analysis? *J. Surg. Res.* **186**, 44–55.

Baraniuk, J. N. 2011 Subjective nasal fullness and objective congestion. *Proc. Am. Thorac. Soc.* **8**, 62–69.

Bazilevs, Y., Calo, V. M., Cottrell, J. A., Hughes, T. J. R., Reali, A. & Scovazzi, G. 2007 Variational multiscale residual-based turbulence modeling for large eddy simulation of incompressible flows. *Comput. Methods Appl. Mech. Eng.* **197**, 173–201.

Broms, P., Jonson, B. & Malm, L. 1982 A pre- and postoperative evaluation in functional septoplasty. *Acta Otolaryngol* **94**, 523–529.

Burrow, A., Eccles, R. & Jones, A. S. 1983 The effects of camphor, eucalyptus and menthol vapour on nasal resistance to airflow and nasal sensation. *Acta Otolaryngol* **96**, 157–161.

Çengel, Y. A., Cimbala, J. M. & Turner, R. H. 2012 *Fundamentals of thermal-fluid sciences*, 4th edn. McGraw-Hill.

Chen, X. B., Leong, S. C., Lee, H. P., Chong, V. F. H. & Wang, D. Y. 2010 Aerodynamic effects of inferior turbinate surgery on nasal airflow - A computational fluid dynamics model. *Rhinology* **48**, 394–400.

Chhabra, N. & Houser, S. M. 2009 The diagnosis and management of empty nose syndrome. *Otolaryngol. Clin. N. Am.* **42**, 311–330.

Chung, S.-K., Son, Y. R., Shin, S. J. & Kim, S.-K. 2006 Nasal airflow during respiratory cycle. *Am. J. Rhinol.* **20**, 379–384.

Clarke, R. W. & Jones, A. S. 1992 Nasal airflow receptors: the relative importance of temperature and tactile stimulation. *Clin. Otolaryngol.* **17**, 388–392.

Clarke, R. W. & Jones, A. S. 1994 The distribution of nasal airflow sensitivity in normal subjects. *J. Laryngol. Otol.* **108**, 1045–1047.

Clarke, R. W., Jones, A. S., Charters, P. & Sherman, I. 1992 The role of mucosal receptors in the nasal sensation of airflow. *Clin. Otolaryngol.* **17**, 383–387.

Cohen, M. L. 1977 Measurement of the thermal properties of human skin. A review. *J. Invest. Dermatol.* **69**, 333–338.

Coste, A., Dessi, P. & Serrano, E. 2012 Empty nose syndrome. *Eur. Ann. Otorhinolaryngol. Head Neck Dis.* **129**, 93–97.

Croce, C., Fodil, R., Durand, M., Sbirlea-Apiou, G., Caillibotte, G., Papon, J.-F., Blondeau, J.-R., Coste, A., Isabey, D. & Louis, B. 2006 In vitro experiments and numerical simulations of airflow in realistic nasal airway geometry. *Ann. Biomed. Eng.* **34**, 997–1007.

Di, M.-Y., Jiang, Z., Gao, Z.-Q., Li, Z., An, Y.-R. & Lv, W. 2013 Numerical simulation of airflow fields in two typical nasal structures of empty nose syndrome: A computational fluid dynamics study. *PLoS ONE* **8**, e84243.

Doorly, D. J., Taylor, D. J. & Schroter, R. C. 2008 Mechanics of airflow in the human nasal airways. *Respir. Physiol. Neurobiol.* **163**, 100–110.

Elad, D., Wolf, M. & Keck, T. 2008 Air-conditioning in the human nasal cavity. *Respir. Physiol. Neurobiol.* **163**, 121–127.

Esmaily-Moghadam, M. 2014 Multi-physics finite element solver (MUPFES). *https://sites.google.com/site/memt63/MUPFES* .

Esmaily-Moghadam, M., Bazilevs, Y., Hsia, T.-Y., Vignon-Clementel, I. E. & Marsden, A. L. 2011 A comparison of outlet boundary treatments for prevention of backflow divergence with relevance to blood flow simulations. *Comput. Mech.* **48**, 277–291.

Fedorov, A., Beichel, R., Kalpathy-Cramer, J., Finet, J., Fillion-Robin, J.-C., Pujol, S., Bauer, C., Jennings, D., Fennessy, F., Sonka, M., Buatti, J., Aylward, S., Miller, J. V., Pieper, S. & Kikinis, R. 2012 3D Slicer as an image computing platform for the Quantitative Imaging Network. *Magn. Reson. Imaging* **30**, 1323–1341.

Freund, W., Wunderlich, A. P., Stöcker, T., Schmitz, B. L. & Scheithauer, M. O. 2011 Empty nose syndrome: limbic system activation observed by functional magnetic resonance imaging. *Laryngoscope* **121**, 2019–2025.

Garcia, G. J. M., Bailie, N., Martins, D. A. & Kimbell, J. S. 2007 Atrophic rhinitis: a CFD study of air conditioning in the nasal cavity. *J. Appl. Physiol.* **103**, 1082–1092.

Grützenmacher, S., Lang, C. & Mlynski, G. 2003 The combination of acoustic rhinometry, rhinoresistometry and flow simulation in noses before and after turbinate surgery: a model study. *Orl* **65**, 341–347.

Hall, W. D. & Pruppacher, H. R. 1976 The survival of ice particles falling from cirrus clouds in subsaturated air. *J. Atmos. Sci.* **33**, 1995–2006.

Hanida, S., Mori, F., Kumahata, K., Watanabe, M., Ishikawa, S. & Matsuzawa, T. 2013 Influence of latent heat in the nasal cavity. *J. Biomech. Sci. Eng.* **8**, 209–224.

Hardcastle, P. F., White, A. & Prescott, R. J. 1988 Clinical and rhinometric assessment of the nasal airway - do they measure the same entity? *Clin. Otolaryngol.* **13**, 185–191.

Hariri, B. M., Rhee, J. S. & Garcia, G. J. M. 2015 Identifying patients who may benefit from inferior turbinate reduction using computer simulations. *Laryngoscope* **125**, 2635–2641.

Hopkins, C., Gillett, S., Slack, R., Lund, V. J. & Browne, J. P. 2009 Psychometric validity of the 22-item Sinonasal Outcome Test. *Clin. Otolaryngol.* **34**, 447–454.

Hörschler, I., Schröder, W. & Meinke, M. 2010 On the assumption of steadiness of nasal cavity flow. *J. Biomech.* **43**, 1081–1085.

Houser, S. M. 2007 Surgical treatment for empty nose syndrome. *Arch. Otolaryngol. Head Neck Surg.* **133**, 858–863.

Jang, Y. J., Kim, J. H. & Song, H. Y. 2011 Empty nose syndrome: radiologic findings and treatment outcomes of endonasal microplasty using cartilage implants. *Laryngoscope* **121**, 1308–1312.

Jones, A. S., Crosher, R., Wight, R. G., Lancer, J. M. & Beckingham, E. 1987 The effect of local anaesthesia of the nasal vestibule on nasal sensation of airflow and nasal resistance. *Clin. Otolaryngol.* **12**, 461–464.

Jones, A. S., Wight, R. G. & Durham, L. H. 1989*a* The distribution of thermoreceptors within the nasal cavity. *Clin. Otolaryngol.* **14**, 235–239.

Jones, A. S., Wight, R. G., Stevens, J. C. & Beckingham, E. 1988 The nasal valve: a physiological and clinical study. *J. Laryngol. Otol.* **102**, 1089–1094.

Jones, A. S., Willatt, D. J. & Durham, L. M. 1989*b* Nasal airflow: resistance and sensation. *J. Laryngol. Otol.* **103**, 909–911.

Jones, W. P. 1994 *Air conditioning engineering*, 4th edn. Edward Arnold.

Kays, W. M. & Crawford, M. E. 1980 *Convective heat and mass transfer*, 2nd edn. McGraw-Hill, Inc.

Keck, T., Leiacker, R., Heinrich, A., Kühnemann, S. & Rettinger, G. 2000 Humidity and temperature profile in the nasal cavity. *Rhinology* **38**, 167–171.

Kehlet, H., Jensen, T. S. & Woolf, C. J. 2006 Persistent postsurgical pain: risk factors and prevention. *Lancet* **367**, 1618–1625.

Keyhani, K., Scherer, P. W. & Mozell, M. M. 1995 Numerical simulation of airflow in the human nasal cavity. *J. Biomech. Eng.* **117**, 429–441.

Kim, D.-W., Chung, S.-K. & Na, Y. 2017 Numerical study on the air conditioning characteristics of the human nasal cavity. *Comput. Biol. Med.* **86**, 18–30.

Kimbell, J. S., Frank, D. O., Laud, P., Garcia, G. J. M. & Rhee, J. S. 2013 Changes in nasal airflow and heat transfer correlate with symptom improvement after surgery for nasal obstruction. *J. Biomech.* **46**, 2634–2643.

Konstantinidis, I., Tsakiropoulou, E., Chatziavramidis, A., Ikonomidis, C. & Markou, K. 2017 Intranasal trigeminal function in patients with empty nose syndrome. *Laryngoscope* **127**, 1263–1267.

Kuan, E. C., Suh, J. D. & Wang, M. B. 2015 Empty nose syndrome. *Curr. Allergy Asthma Rep.* **15**, 493.

Kumahata, K., Mori, F., Ishikawa, S. & Matsuzawa, T. 2010 Nasal flow simulation using heat and humidity models. *J. Biomech. Sci. Eng.* **5**, 565–577.

Lee, J.-H., Na, Y., Kim, S.-K. & Chung, S.-K. 2010 Unsteady flow characteristics through a human nasal airway. *Respir. Physiol. Neurobiol.* **172**, 136–146.

Lemogne, C., Consoli, S. M., Limosin, F. & Bonfils, P. 2015 Treating empty nose syndrome as a somatic symptom disorder. *Gen. Hosp. Psychiatry* **37**, 273.e9–273.e10.

Leong, S. C. 2015 The clinical efficacy of surgical interventions for empty nose syndrome: a systematic review. *Laryngoscope* **125**, 1557–1562.

Li, C., Farag, A. A., Leach, J., Deshpande, B., Jacobowitz, A., Kim, K., Otto, B. A. & Zhao, K. 2017 Computational fluid dynamics and trigeminal sensory examinations of empty nose syndrome patients. *Laryngoscope* **127**, E176–E184.

Lindemann, J., Leiacker, R., Rettinger, G. & Keck, T. 2002 Nasal mucosal temperature during respiration. *Clin. Otolaryngol.* **27**, 135–139.

Modrzyński, M. 2011 Hyaluronic acid gel in the treatment of empty nose syndrome. *Am. J. Rhinol. Allergy* **25**, 103–106.

Moore, E. J. & Kern, E. B. 2001 Atrophic rhinitis: a review of 242 cases. *Am. J. Rhinol.* **15**, 355–361.

Mygind, N. & Dahl, R. 1998 Anatomy, physiology and function of the nasal cavities in health and disease. *Adv. Drug Deliv. Rev.* **29**, 3–12.

Na, Y., Chung, K. S., Chung, S.-K. & Kim, S. K. 2012 Effects of single-sided inferior turbinectomy on nasal function and airflow characteristics. *Respir. Physiol. Neurobiol.* **180**, 289–297.

Naftali, S., Schroter, R. C., Shiner, R. J. & Elad, D. 1998 Transport phenomena in the human nasal cavity: a computational model. *Ann. Biomed. Eng.* **26**, 831–839.

Olsson, P. & Bende, M. 1985 Influence of environmental temperature on human nasal mucosa. *Ann. Otol. Rhinol. Laryngol.* **94**, 153–155.

Ophir, D. 1990 Resection of obstructing inferior turbinates following rhinoplasty. *Plast. Reconstr. Surg.* **85**, 724–727.

Pallanch, J. F., McCaffrey, T. V. & Kern, E. B. 1985 Normal nasal resistance. *Otolaryngol. Head. Neck Surg.* **93**, 778–785.

Payne, S. C. 2009 Empty nose syndrome: what are we really talking about? *Otolaryngol. Clin. N. Am.* **42**, 331–337.

Pennes, H. H. 1948 Analysis of tissue and arterial blood temperatures in the resting human forearm. *J. Appl. Physiol.* **1**, 93–122.

Pointwise Inc. 2016 Pointwise.

Proctor, D. F. & Andersen, I. 1982 *The Nose: upper airway physiology and the atmospheric environment*. Elsevier Biomedical Press.

Quadrio, M., Pipolo, C., Corti, S., Messina, F., Pesci, C., Saibene, A. M., Zampini, S. & Felisati, G. 2016 Effects of CT resolution and radiodensity threshold on the CFD evaluation of nasal airflow. *Med. Biol. Eng. Comput.* **54**, 411–419.

Rhee, J. S., Pawar, S. S., Garcia, G. J. M. & Kimbell, J. S. 2011 Toward personalized nasal surgery using computational fluid dynamics. *Arch. Facial Plast. Surg.* **13**, 305–310.

Rice, D. H. 2000 Rebuilding the inferior turbinate with hydroxyapatite cement. *Ear, Nose Throat J.* **79**, 276–277.

Rudmik, L., Hopkins, C., Peters, A., Smith, T. L., Schlosser, R. J. & Soler, Z. M. 2015 Patient-reported outcome measures for adult chronic rhinosinusitis: a systematic review and quality assessment. *J. Allergy Clin. Immunol.* **136**, 1532–1540.e2.

Saafan, M. E., Hegazy, H. M. & Albirmawy, O. A. 2016 Empty nose syndrome: etiopathogenesis and management. *Egypt. J. Otolaryngol.* **32**, 119–129.

Scheithauer, M. O. 2010 Surgery of the turbinates and "empty nose" syndrome. *GMS Curr. Top. Otorhinolaryngol. Head Neck Surg.* **9**, Doc03.

Schmidt, R. & Singh, K. 2010 Meshmixer: an interface for rapid mesh composition. In *SIGGRAPH 2010*.

Shah, K., Guarderas, J. & Krishnaswamy, G. 2016 Empty nose syndrome and atrophic rhinitis. *Ann. Allergy, Asthma Immunol.* **117**, 217–220.

Sozansky, J. & Houser, S. M. 2015 Pathophysiology of empty nose syndrome. *Laryngoscope* **125**, 70–74.

Steinman, D. A. & Others 2013 Variability of computational fluid dynamics solutions for pressure and flow in a giant aneurysm: the ASME 2012 Summer Bioengineering Conference CFD Challenge. *J. Biomech. Eng.* **135**, 021016.

Sullivan, C. D., Garcia, G. J. M., Frank-Ito, D. O., Kimbell, J. S. & Rhee, J. S. 2014 Perception of better nasal patency correlates with increases in mucosal cooling after surgery for nasal obstruction. *Otolaryngol. Head Neck Surg.* **150**, 139–147.

Swift, A. C., Campbell, I. T. & McKown, T. M. 1988 Oronasal obstruction, lung volumes, and arterial oxygenation. *Lancet* **331**, 73–75.

Thamboo, A., Velasquez, N., Habib, A.-R. R., Zarabanda, D., Paknezhad, H. & Nayak, J. V. 2017 Defining surgical criteria for empty nose syndrome: validation of the office-based cotton test and clinical interpretability of the validated Empty Nose Syndrome 6-Item Questionnaire. *Laryngoscope* **127**, 1746–1752.

Tobin, M. J., Chadha, T. S., Jenouri, G., Birch, S. J., Gazeroglu, H. B. & Sackner, M. A. 1983 Breathing patterns: 1. Normal subjects. *Chest* **84**, 202–205.

Torvi, D. A. & Dale, J. D. 1994 A finite element model of skin subjected to a flash fire. *J. Biomech. Eng.* **116**, 250–255.

Tsu, M. E., Babb, A. L., Ralph, D. D. & Hlastala, M. P. 1988 Dynamics of heat, water, and soluble gas exchange in the human airways: 1. A model study. *Ann. Biomed. Eng.* **16**, 547–571.

Velasquez, N., Thamboo, A., Habib, A.-R. R., Huang, Z. & Nayak, J. V. 2016 The Empty Nose Syndrome 6-Item Questionnaire (ENS6Q): a validated 6-item questionnaire as a diagnostic aid for empty nose syndrome patients. *Int. Forum Allergy Rhinol.* **7**, 64–71.

Wen, J., Inthavong, K., Tu, J. & Wang, S. 2008 Numerical simulations for detailed airflow dynamics in a human nasal cavity. *Respir. Physiol. Neurobiol.* **161**, 125–135.

Wexler, D., Segal, R. & Kimbell, J. 2005 Aerodynamic effects of inferior turbinate reduction: computational fluid dynamics simulation. *Arch. Otolaryngol. Head Neck Surg.* **131**, 1102–1107.

Witt, R. L. 2005 Minimally invasive surgery for parotid pleomorphic adenoma. *Ear, Nose Throat J.* **84**, 308–311.

Wrobel, B. B., Bien, A. G., Holbrook, E. H., Meyer, G. E., Bratney, N. A., Meza, J. & Leopold, D. A. 2006 Decreased nasal mucosal sensitivity in older subjects. *Am. J. Rhinol.* **20**, 364–368.

Xu, F., Lu, T. J. & Seffen, K. A. 2008 Biothermomechanics of skin tissues. *J. Mech. Phys. Solids* **56**, 1852–1884.

Zhao, K., Blacker, K., Luo, Y., Bryant, B. & Jiang, J. 2011 Perceiving nasal patency through mucosal cooling rather than air temperature or nasal resistance. *PLoS ONE* **6**, e24618.

Zhao, K., Jiang, J., Blacker, K., Lyman, B., Dalton, P., Cowart, B. J. & Pribitkin, E. A. 2014 Regional peak mucosal cooling predicts the perception of nasal patency. *Laryngoscope* **124**, 589–595.

Appendix A

Analytic solutions in the wall conduction layer

A.1 Solution to the Pennes equation

The Pennes equation for one-dimensional heat transfer across a layer of biological tissue is

$$\rho c_t \frac{\partial T}{\partial t} = k\frac{\partial^2 T}{\partial y^2} + \omega_b \rho_b c_b \left(T_{blood} - T\right) + S_{met} + S_{ext}, \tag{A.1}$$

where ρ, k, and c_t are the tissue density, thermal conductivity, and specific heat capacity respectively; T and T_{blood} (constant) are the tissue and blood temperatures respectively; t is time; y is the vertical direction, normal to the tissue layer; ω_b is the blood perfusion rate; ρ_b and c_b are the blood density and specific heat capacity respectively; and S_{met} and S_{ext} are the tissue metabolic heat generation and external heat sources.

At steady state and with no external heat sources this becomes

$$k\frac{d^2 T}{dy^2} - \omega_b \rho_b c_b T = -\omega_b \rho_b c_b T_{blood} - S_{met}, \tag{A.2}$$

a second-order linear differential equation. This can be solved with an ansatz of the form $T = \mathrm{e}^{my}$, where m is a constant. The auxiliary equation is

$$km^2 - \omega_b \rho_b c_b = 0, \tag{A.3}$$

to give

$$m = \pm\sqrt{\frac{\omega_b \rho_b c_b}{k}}, \tag{A.4}$$

and the resulting complementary function

$$T_c = C_1 \exp\left(y\sqrt{\frac{\omega_b \rho_b c_b}{k}}\right) + C_2 \exp\left(-y\sqrt{\frac{\omega_b \rho_b c_b}{k}}\right), \tag{A.5}$$

where C_1 and C_2 are constants.

The particular integral is picked to be of the form $T_p = A$, where A is a constant. The particular integral is substituted into the original differential equation (Equation A.2) to give

$$\begin{aligned} 0 - \omega_b \rho_b c_b A &= -\omega_b \rho_b c_b T_{blood} - S_{met}, \\ A &= T_{blood} + \frac{S_{met}}{\omega_b \rho_b c_b}, \end{aligned} \tag{A.6}$$

and the resulting particular integral

$$T_p = T_{blood} + \frac{S_{met}}{\omega_b \rho_b c_b}. \tag{A.7}$$

The general solution of Equation A.2 can then be found as

$$\begin{aligned} T_g &= T_c + T_p, \\ &= C_1 \exp\left(y\sqrt{\frac{\omega_b \rho_b c_b}{k}}\right) + C_2 \exp\left(-y\sqrt{\frac{\omega_b \rho_b c_b}{k}}\right) + T_{blood} + \frac{S_{met}}{\omega_b \rho_b c_b}, \end{aligned} \tag{A.8}$$

where constants C_1 and C_2 can be found by application of the boundary conditions.

The boundary conditions for the conduction layer will include a temperature at the bottom of the layer, and a heat flux at the surface as follows

$$\begin{cases} T = T_b, & y = 0, \\ \dot{q} = \dot{q}_w, & y = w, \end{cases}$$

where w is the thickness of the layer and $\dot{q}$ denotes heat flux defined as

$$\dot{q} = -k\frac{dT}{dy}. \tag{A.9}$$

Substituting the first boundary condition into the general solution (Equation A.8) and rearranging gives

$$C_1 = T_b - C_2 - \frac{S_{met}}{\omega_b \rho_b c_b} - T_{blood}. \tag{A.10}$$

Differentiating Equation A.8 and multiplying by $-k$ to yield the heat flux gives

$$\dot{q} = -k\beta \left[C_1 \mathrm{e}^{y\beta} - C_2 \mathrm{e}^{-y\beta} \right], \tag{A.11}$$

where we denote $\beta = \sqrt{\frac{\omega_b \rho_b c_b}{k}}$.

Substituting the second boundary condition here yields

$$\dot{q}_w = -k\beta \left[C_1 \mathrm{e}^{w\beta} - C_2 \mathrm{e}^{-w\beta} \right]. \tag{A.12}$$

Substituting Equation A.10 into Equation A.12 we can solve for C_2,

$$C_2 = \frac{\frac{-\dot{q}_w}{k\beta} - \mathrm{e}^{w\beta} \left[T_b - \frac{S_{met}}{\omega_b \rho_b c_b} - T_{blood} \right]}{-\mathrm{e}^{w\beta} - \mathrm{e}^{-w\beta}}. \tag{A.13}$$

We can then solve for C_1 by substituting Equation A.13 back into Equation A.10,

$$C_1 = T_b + \frac{\frac{\dot{q}_w}{k\beta} + \mathrm{e}^{w\beta} \left[T_b - \frac{S_{met}}{\omega_b \rho_b c_b} - T_{blood} \right]}{-\mathrm{e}^{w\beta} - \mathrm{e}^{-w\beta}} - \frac{S_{met}}{\omega_b \rho_b c_b} - T_{blood}. \tag{A.14}$$

Both C_1 and C_2 are linear functions of $\dot{q}_w$, and the general solution, T_g, is a linear function of C_1 and C_2, therefore the surface temperature, $T(w)$, is a linear function of the imposed surface heat flux, $\dot{q}_w$.

We can write $T(w)$ in the form

$$T(w) = A\dot{q}_w + B, \tag{A.15}$$

where A and B are constants defined as

$$A = \frac{\mathrm{e}^{w\beta} - \mathrm{e}^{-w\beta}}{k\beta \left(-\mathrm{e}^{w\beta} - \mathrm{e}^{-w\beta} \right)}, \tag{A.16}$$

$$B = \left(T_b - \frac{S_{met}}{\omega_b \rho_b c_b} - T_{blood} \right) \left(\mathrm{e}^{w\beta} + \frac{\mathrm{e}^{2w\beta} - 1}{-\mathrm{e}^{w\beta} - \mathrm{e}^{-w\beta}} \right) + T_{blood} + \frac{S_{met}}{\omega_b \rho_b c_b}. \tag{A.17}$$

A.2 Solution to the heat conduction equation

Steady state one-dimensional conduction in the conduction layer is governed by

$$\frac{d^2T}{dy^2} = 0. \tag{A.18}$$

Integrating yields

$$\frac{dT}{dy} = C_1, \tag{A.19}$$

and again

$$T = C_1 y + C_2, \tag{A.20}$$

where C_1 and C_2 are constants.

The boundary conditions are

$$\begin{cases} T = T_b, & y = 0, \\ \dot{q} = \dot{q}_w, & y = w, \end{cases}$$

where w is the thickness of the layer and $\dot{q}$ denotes heat flux defined as

$$\dot{q} = -k\frac{dT}{dy}. \tag{A.21}$$

Substituting the boundary conditions into Equations A.19 and A.20 and solving gives the general solution,

$$T = \frac{-\dot{q}_w}{k}y + T_b. \tag{A.22}$$

The temperature at the surface of the layer, $T(w)$, is therefore a linear function of the surface heat flux, $\dot{q}_w$, as was the solution of the Pennes equation.

We can write $T(w)$ in the form

$$T(w) = A\dot{q}_w + B, \tag{A.23}$$

where A and B are constants defined as

$$A = \frac{-w}{k}, \tag{A.24}$$

$$B = T_b. \tag{A.25}$$